THESIS FOR THE DEGREE OF DOCTORATE OF PHILOSOPHY

Circumstellar dust emission from nearby Solar-type stars

JOACHIM WIEGERT

CHALMERS

Department of Earth and Space Sciences
CHALMERS UNIVERSITY OF TECHNOLOGY
Göteborg, Sweden 2016

Circumstellar dust emission from nearby Solar-type stars
JOACHIM WIEGERT
ISBN 978-91-7597-443-9

Doktorsavhandlingar vid Chalmers tekniska högskola
Ny serie nr 4124
ISSN 0346-718X

Radio Astronomy & Astrophysics Group
Department of Earth and Space Sciences
Chalmers University of Technology
SE–412 96 Göteborg, Sweden
Phone: +46 (0)31–772 1000

Contact information:
Joachim Wiegert
Onsala Space Observatory
Chalmers University of Technology
SE–439 92 Onsala, Sweden

Phone: +46 (0)31–772 5542
E-mail: joachim.wiegert@chalmers.se

Cover image:
Composite images showing the Herschel Space Observatory (right) and the Atacama Pathfinder EXperiment (bottom left) together with particle simulation results of circumstellar discs around α Centauri, and Herschel/PACS observations of α Centauri and 94 Ceti at 100 μm.
Image credits: ESA/AOES Medialab, and DUNES: DUst around NEarby Stars.

Printed by Chalmers Reproservice
Chalmers University of Technology
Göteborg, Sweden 2016

Circumstellar dust emission from nearby Solar-type stars

JOACHIM WIEGERT
Department of Earth and Space Sciences
Chalmers University of Technology

Abstract

Far-infrared excess above the photosphere of a star indicates the presence of a circumstellar dust disc, which is a sign-post for extrasolar planets, and was first detected in the mid 1980s. Dust discs are intricately connected to planets and planetesimals, give insights in the dynamics and evolution of the system, and are also useful for future exoplanet-observations. This thesis is aimed at modelling dust emission of nearby Solar-type stars, and is partly involved with the *Herschel* key programme DUst around NEarby Stars (DUNES). It includes detailed studies on a few nearby stars, and results from a coherent re-reduction of the combined datasets of the original DUNES catalogue and 55 DEBRIS-observed sources (Disc Emission via a Bias-free Reconnaissance in the Infrared/Sub-millimetre).

Based on observations with *Herschel* and *Spitzer* of the nearby binary α Centauri (G2 V and K1 V), an upper limit on the fractional luminosity (dust-to-star) of circumstellar dust was determined to a few 10^{-5} (Paper I). Both stars exhibit detectable temperature minima at wavelengths around 100-300 μm due to a chromospheric temperature inversion akin to that of the sun. The resulting flux difference, when compared to stellar photospheric models, is equivalent to dust emission with a fractional luminosity of $< 2 \times 10^{-7}$.

The triple star 94 Ceti hosts known dust emission-features that are modelled in Paper II. The dust is constrained to a circumbinary disc around the companion stars, 94 Cet B and C (M dwarfs), which orbits the primary 94 Cet A (F8 V) on a 2000 year orbit, with a fractional luminosity of $4.6 \pm 0.4 \times 10^{-6}$, and a disc radius of 40 AU. Tentative evidence for a circumtertiary disc is also found.

The resolved emission at EP Eridani (K1 V) corresponds well with a face-on dust disc with the outer radius 110 AU, an inner hole of 5 to 10 AU, and fractional luminosity of $2.0 \pm 0.2 \times 10^{-5}$. The emission at Gliese 42 (K2 V) appears contaminated by background sources. Dust models with a flatter than normal grain size distribution fit the observations with a fractional luminosity of $8.7 \pm 1.0 \times 10^{-6}$. A wide range of far-infrared galaxy SEDs, with redshifts between 0.7 to 1.9, and IR luminosities of 0.4 to $8.3 \times 10^{12}\ L_{\odot}$, also fit these data.

The DUNES catalogue, combined with 55 DEBRIS-observed sources, contains 188 nearby FGK stars (including resolved binaries). These data were previously reduced with older versions of the *Herschel* software and calibration, and have now been coherently re-reduced with more recent versions. There are 16 new marginal excess sources, and one new detected at δ Pavonis. We find a systematical 1σ higher flux density for the 133 original DUNES sources, while the estimates for the additional 55 sources agree well with our results.

Keywords: Stars: binaries - Stars: circumstellar matter - Infrared: stars - Infrared: planetary systems - Submillimeter: stars

Research contributions

This thesis is based on the work contained in the following papers.

I J. Wiegert, R. Liseau, P. Thébault, G. Olofsson, A. Mora, G. Bryden, J. P. Marshall, C. Eiroa, B. Montesinos, D. Ardila, J. C. Augereau, A. Bayo Aran, W. C. Danchi, C. del Burgo, S. Ertel, M. C. W. Fridlund, M. Hajigholi, A. V. Krivov, G. L. Pilbratt, A. Roberge, G. J. White, and S. Wolf:
How dusty is α Centauri? Excess or non-excess over the infrared photospheres of main-sequence stars
Astronomy & Astrophysics, 563, A102 (2014)
DOI: 10.1051/0004-6361/201321887

II J. Wiegert, V. Faramaz, F. Cruz-Saenz de Miera:
94 Ceti: a triple star with a planet and dust disc
Monthly Notices of the Royal Astronomical Society, 462 (2), 1735-1748 (2016)
DOI: 10.1093/mnras/stw1682

III J. Wiegert:
Nearby debris discs: a second look at DUNES' observations of nearby Solar-like stars
In preparation for publication in Astronomy & Astrophysics

I have also contributed to the following publications (not appended).

i Alessandro B. Romeo and Joachim Wiegert:
The effective stability parameter for two-component galactic discs: is $Q^{-1} \propto Q_{\rm stars}^{-1} + Q_{\rm gas}^{-1}$?
Monthly Notices of the Royal Astronomical Society, 416, 1191-1196 (2011)
DOI: 10.1111/j.1365-2966.2011.19120.x

ii R. Liseau, B. Montesinos, G. Olofsson, G. Bryden, J. P. Marshall, D. Ardila, A. Bayo Aran, W. C. Danchi, C. del Burgo, C. Eiroa, S. Ertel, M. C. W. Fridlund, A. V. Krivov, G. L. Pilbratt, A. Roberge, P. Thébault, J. Wiegert, and G. J. White:
α Centauri A in the far infrared. First measurement of the temperature minimum of a star other than the Sun
Astronomy & Astrophysics, 549, L7 (2013)
DOI: 10.1051/0004-6361/201220776

iii F. Taddia, J. Sollerman, E. Gafton, G. Micheva, E. Freeland, A. Macchiavello, T. Mansson, J. Wiegert:
NOT spectroscopic classifications of optical transients
The Astronomer's Telegram, 5087 (2013)

iv R. Amanullah, J. Johansson, A. Goobar, R. Ferretti, S. Papadogiannakis, T. Petrushevska, P. J. Brown, Y. Cao, C. Contreras, H. Dahle, N. Elias-Rosa, J. P. U. Fynbo, J. Gorosabel, L. Guaita, L. Hangard, D. A. Howell, E. Y. Hsiao, E. Kankare, M. Kasliwal, G. Leloudas, P. Lundqvist, S. Mattila, P. Nugent, M. M. Phillips, A. Sandberg, V. Stanishev, M. Sullivan, F. Taddia, G. Östlin, S. Asadi, R. Herrero-Illana, J. J. Jensen, K. Karhunen, S. Lazarevic, E. Varenius, P. Santos, S. Seethapuram Sridhar, S. H. J. Wallström, and J. Wiegert:
Diversity in extinction laws of Type Ia supernovae measured between 0.2 and 2 μm
Monthly Notices of the Royal Astronomical Society, 453, 3300-3328 (2015)
DOI: 10.1093/mnras/stv1505

Acknowledgements

Astronomy is one of the most ancient natural sciences, with roots all the way back to those who, with their eyes only, were able to map the stars and the movement of the planets in Mesopotamia, some 4000 years ago. It has been a humbling experience to carry on this tradition. I have spent the last years trying to contribute with a small piece of a puzzle to help the humanity to understand its place in the Universe.

There are many people I would like to thank for being around during this time. But first I must of course thank my supervisor, René Liseau, who introduced me to this specific field in astronomy and to the fantastic people in the DUNES collaboration. My co-supervisors have also always been available, Magnus Thomasson and John Black. I have also appreciated the help from Tuomas Lunttila, Kalle Torstensson, Alessandro Romeo, and Wouter Vlemmings.

I would like to thank the whole DUNES team for amazing workshops and a healthy cooperation. I want to especially mention Carlos Eiroa, Philippe Thébault, Virginie Faramaz, Fernando Cruz-Saenz de Miera (thanks for showing me around Madrid), Jonathan "Jonty" Marshall, Alexander "Sasha" Krivov, and Grant Kennedy.

The fantastic people at the department of Earth and Space Sciences at Chalmers, and at the Onsala Space Observatory deserves to be mentioned also. In the administrative and technical staff, thanks to Camilla, Glenn, Katarina K., Katarina N., Maria, Paula, Paulina, Per B., Roger, Simon, and Sofie! Those taking care of us PhD-students, Donal Murtagh and Susanne Aalto. And I'm name-dropping here because I think all of these are worth mentioning; the fantastic postdocs, (former) PhD-students et al., Boy, Daniel, Daria, Elvire, Eskil, Eva, Fabien, Francesco, Grzegorz, JB, Joakim, Johan, Judit, Lukas, Maryam, Matthias, Mitra, Niko, Niklas, Ole Martin, Per Bj., Robert, Robin, Sabine, Sofia, Suzy, and Taïssa. And a big thanks for the staff at APEX, working there has always been a pleasure, even during the long night shifts.

Finally I want to thank friends and family. Those living in the Hilbert room, at Göteborg University, which it seems I can't stop visiting. My parents, Lars and Monica who has always been very supportive and also helped me to proofread this thesis. My sister Theresa who is an inspiration and has done a marvellous detailed job with proofreading this thesis. My brothers, Benjamin, and Daniel plus his wife Jennifer (thanks for letting me and Theresa toast your wedding), who are fun as always, and of course our dachshund Cassie. I want to thank my lovely girlfriend, Beata, who is always there and supportive. I thank her family also, who have accepted me into their company. I'm so thankful that you want to be with me, Beata, even though I sometimes travel halfway across the world to steer a telescope or to sit at lectures. You stay with me even when I can't stop talking about space and science fiction!

And to you, who have just picked up this thesis. For me, to work in astronomy has been a long-term goal and perhaps even a dream. This thesis might be a culmination for me, of more than ten years of physics and astronomy studies. But I do believe, that you're supposed to keep learning and exploring your whole life. This is the end of one journey, and at the same time the beginning of the next one. I hope you also learn something from this work.

Joachim, 2016

"... I am both terrified and reassured to know that there are still wonders in the universe, that we have not yet explained everything." - Straczynski, J. M.

Contents

Chapter 1

Introduction

Circumstellar environments are highly dynamical and evolving systems, in particular during the earlier eras when they are dominated by thick gas and dust discs. Later, when the central star enters the main sequence, the evolution continues, albeit slower. At this time the stellar flux increases which clears its surroundings from most of the gas and dust, and only planets of different sizes and rings of planetesimals remain.

These rings of planetesimals are important for the circumstellar dust that are discussed in this thesis. Gravitational influences from surrounding planets will create collisions in these rings. Such collisions result in the production of μm sized dust grains (or debris) which spread throughout the planetary disc and form a dust cloud around the star (see e.g. the review by Moro-Martín 2013).

This dust cloud is affected by the radiation field from the central star in several ways. Consequently the cloud is easily heated so that it exhibits black body-like emission. With sufficient amount of dust being heated, this leads to observable excesses at far-infrared (FIR) wavelengths of the stellar spectrum. The peak wavelengths depend on the size of the disc and the stellar luminosity.

The dust is, however, not long-lived. Continued production of dust is required to sustain a circumstellar dust disc. Thus the presence of dust emission is an indirect indication of the existence of a planetary system around the star. Detailed studies of these dust discs can teach us more on the dynamics of planetary systems and their evolution, and put the Solar system into a wider context.

1.1 The famous four

The first circumstellar dust disc outside the Solar system was observed already in 1984 at the star Vega (α Lyrae, spectral class A0 V) by Aumann et al. (1984) with the Infrared Astronomical Satellite (IRAS). However, as they saw the dust emission only in the spectral energy distribution (SED) they could not infer any dust cloud shape (see Figure 1.1). The excess is beyond 12 μm and peaks close to 60 μm, and they interpreted this as emission from solid particles at 85 AU from the star, distributed in either a shell or a ring. Since such excesses were first observed at Vega, it was also called the "Vega phenomenon".

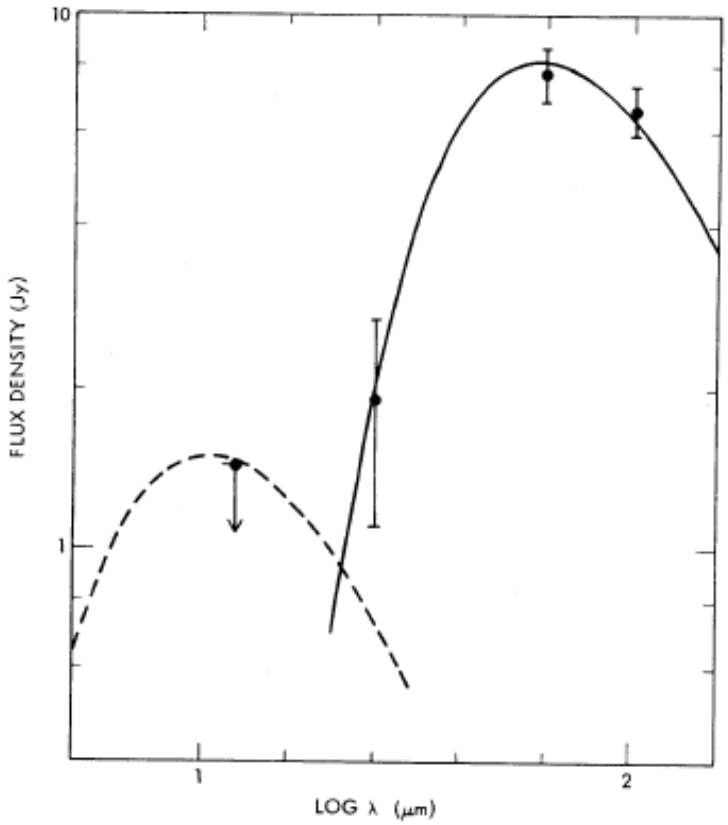

Figure 1.1: Figure 1 from Aumann et al. (1984) with the dust SED from Vega. The original caption reads as follows: "Energy distribution of the infrared excess from α Lyr. The error bars represent the 10% calibration uncertainty. The 12 μm upper limit indicates the effect of the 5% uncertainty in the absolute calibration at 12 μm. The solid line represents a 85 K black body spectrum with a solid angle of 7×10^{-13} sr fitted to the excess. The dashed line represents a 500 K black body spectrum with a solid angle of 6.3×10^{-16} sr arbitrarily fitted to the 12 μm upper limit."

Just a month later the same year, Smith & Terrile (1984) published their observations of β Pictoris, and announced that they had been able to optically observe a circumstellar disc around the star. They inferred that they had detected an edge-on disc, ~ 400 AU in radius (see Figure 1.2). They did not know the age of the star, but deduced that it is probably a young star, and they speculated that the disc might be a protoplanetary disc.

Today β Pictoris is considered to be a young star on the main sequence (spectral class A6 V) with indications that planet formation is still ongoing (Zuckerman et al. 2001; Wahhaj et al. 2003). Furthermore, Lagrange et al. (2009) were able to directly image a giant planet using the Very Large Telescope (VLT). They inferred a mass of $8\,M_{\rm Jup}$[1] with an orbit semi-major axis of ~ 8 AU. (See also the review by Artymowicz 1997 on β Pic.)

More indications of circumstellar dust were found as more data from IRAS got analysed in the 1980s. Vega-like excesses were quite soon discovered in the spectra of two additional stars, Fomalhaut (α Piscis Australis, spectral class A3 V) and ε Eridani (spectral class K2 V),

[1]The mass of Jupiter is $M_{\rm Jup} = 1.9 \times 10^{27}$ kg.

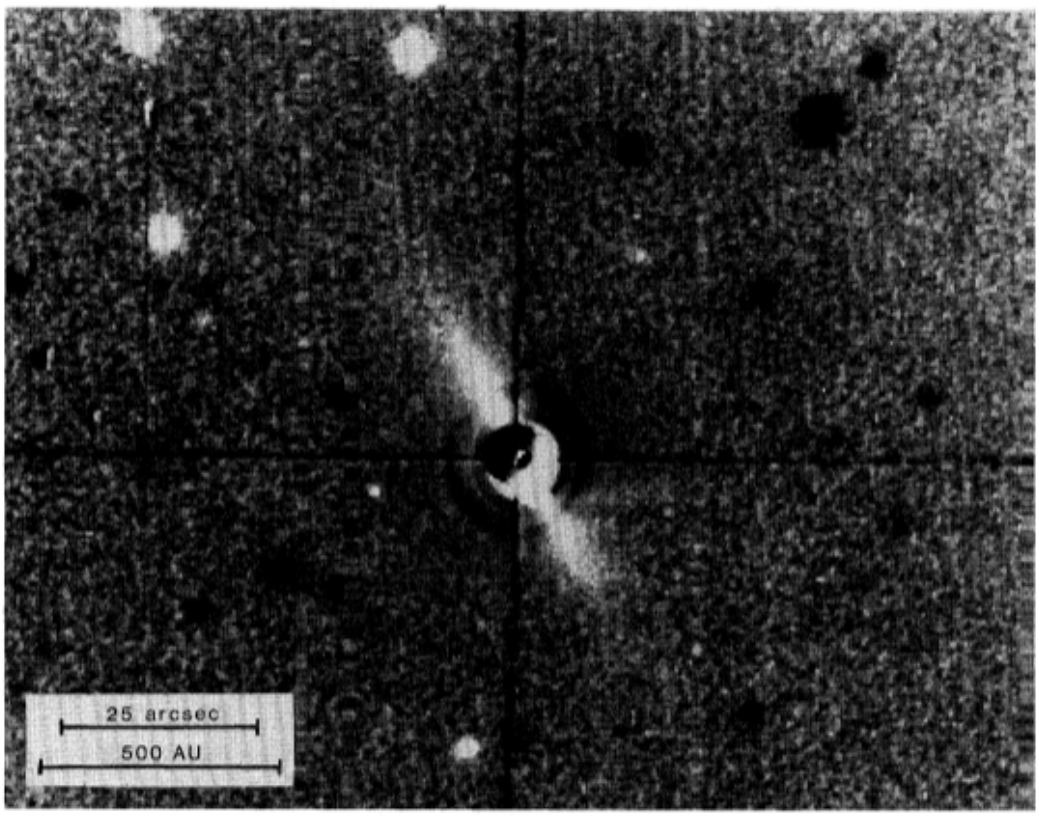

Figure 1.2: Figure 1 from Smith & Terrile (1984) with optical observations of the β Pictoris disc. The original caption reads as follows: "Ratio image (β Pictoris divided by α Pictoris) showing the edge-on circumstellar disk extending 25″ (400 AU) to the northeast and southwest of the star, which is situated behind an obscuring mask. North is at the top. The dark halo surrounding the mask is caused by imperfect balance in the ratioing process. For further explanation, see text."

see Aumann (1985); Gillett (1986), and Figure 1.3. These four were sometimes called the "the famous four", as they were the first four stars with confirmed circumstellar dust.

Fomalhaut is an ever surprising object among these four stars and has been subject of a great deal of recent research. It has been found to be a triple star system that hosts several dust discs and maybe a planet (Fomalhaut b), however, the nature of the planet is still a subject of discussion. The main dust belt has since the 1980s been directly observed with e.g. the *Hubble* Space Telescope (HST) and the planet candidate was also found through direct observations with the HST (Kalas et al. 2008). The third stellar component was found by Mamajek et al. (2013) to be an M4 dwarf star. It is lies 0.77 pc from Fomalhaut and shares its proper motion. Kennedy et al. (2014) also detected a dust excess in the FIR of the third star, which is unusual for M dwarfs. Shannon et al. (2014) suggested that the two Fomalhaut companion stars were formed together and later were captured by Fomalhaut.

As mentioned before, when the Vega-phenomenon was first found it was immediately interpreted as heat emission from $\sim$mm-sized grains, which in turn were interpreted as being either remnants from planet-forming discs, or debris (if assumed to lie in a disc). The con-

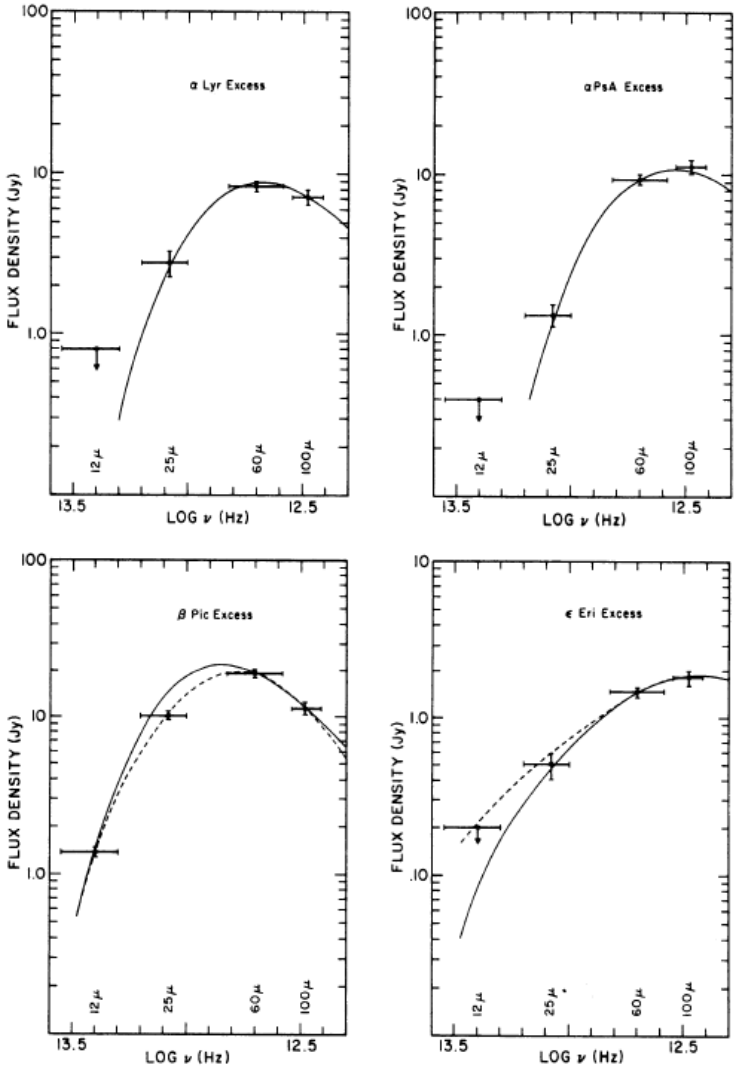

Figure 1.3: Figure 1 from Gillett (1986) with the dust SEDs associated with the Famous four, with Vega (top left), Fomalhaut (top right), β Pictoris (bottom left), and ε Eridani (bottom right). The original caption reads as follows: "Flux density distributions for the excess emission associated with the program stars. The solid curves for α Lyr, α PsA and ε Eri show fits for the black body models described in Table II. The solid curve for β Pic shows fit for black body model with $\gamma = 1$ and the dashed curve shows fit for the small particle model included in Table I. The dashed curve for ε Eri is for a model with $T_{\max} = 500$K."

nection between circumstellar discs, former planetary formation, and the existence of planets is obvious. However, no extrasolar planets (exoplanets) had yet been confirmed at this time.

The connection with planetary systems is due to the fact that all of these stars are main sequence stars. Grains of sizes $\lesssim$1 mm are not very long-lived in circumstellar environments due to Poynting-Robertson drag (PR-drag) and radiation pressure (these are described in Section 2.1). Thus where dust grains exist, there must also exist a sustained dust production which requires belts of planetesimals and planets.

1.2 The first exoplanets

The officially first, confirmed, exoplanet around a main sequence star is 51 Pegasi b. It was first announced by Mayor & Queloz (1995) who were using the radial velocity method. The planet is a gas giant with a mass of $M \sin i \approx 0.5\,M_{\rm Jup}$,[2] and an orbit semi-major axis of 0.05 AU. The star, 51 Pegasi (HR 8729, HD 217014, or Gliese 882) is a G5 V star at a distance of 13.7 pc. The proximity between the planet and star is why this planet is also considered to be the first *hot Jupiter* found.

However, it is worth noting that a planet was announced already in 1988 around the binary γ Cephei (HR 8974, HIP 116727) by Campbell et al. (1988), also by observing radial velocity. They inferred that they had found a massive planet with $M \sin i \approx 1.6\,M_{\rm Jup}$ and a period of 2.7 years. However, Walker et al. (1992) later revoked this discovery when they showed that the planetary signal was most probably due to variations in γ Cephei's rotation (they classed the star to be a K0 III star at this time and such variation is common among larger K-stars). But the planetary discovery was later reaffirmed again by Hatzes et al. (2003), who refined the measurements of the velocity variation of the star, and found that it actually does not coincide with the variations due to the planet. The star was also reclassified to a K1 IV star. The most likely explanation is a planet with the mass $M \sin i = 1.7 \pm 0.4\,M_{\rm Jup}$ and the orbit semi-major axis of 2.13 AU, and it was denoted γ Cephei Ab.

As a curiosity, it is also worth mentioning the discoveries by Wolszczan & Frail (1992). They reported finding evidence for two, or more, planet-massed objects around the millisecond pulsar PSR1257+12. They proposed the existence of two planets with masses of at least 2.8 and $3.4\,M_{\oplus}$, and with orbit semi-major axes of 0.47 and 0.36 AU respectively.

The discoveries by Mayor & Queloz (1995) are nevertheless the first confirmed observations of an exoplanet around a main sequence star. This marked the birth of a whole new field in astronomy where, now, after more than 20 years, there are almost 3000 confirmed planets reported in over 1300 systems[3]. By combining exoplanet discoveries with circumstellar dust disc findings, one can finally start to understand the inner workings of planetary systems and their evolution.

[2]The inferred mass of exoplanets when discovered by using radial velocity depend on the unknown inclination, i of the planetary orbit relative to our line of sight.

[3]As of 2016-07-25, see e.g. `http://exoplanets.org/`, `http://exoplanet.eu/`, and `http://www.openexoplanetcatalogue.com/`

1.3 Combining dust discs and planets

It is now convenient to take a look back at our Solar system. After all, one of the general goals in this field is to put the Solar system into a wider context.

An outside observer with technology not much more advanced than ours, would see an extended dust disc with an outer radius of $50 - 100$ AU, and with a central hole of a radius of 30 AU that is carved out by the four giant planets. The outer dust disc consists of debris produced by the Edgeworth-Kuiper belt (often shortened to Kuiper belt, or EKB, as it is named after Kenneth Edgeworth and Gerard Kuiper). The observer might even be able to observe the Zodiacal cloud, an inner debris disc produced by the asteroid belt and cometary debris, which stretches from ~ 4 AU radius inwards towards the Sun. However, both of these discs would have very faint emission.

The asteroid belt and Kuiper belt could in general be called planetesimal rings. It is in such rings where μm to mm dust/debris particles are produced through collisions, and then spread by non-gravitational forces to form a disc, which is also shaped by the gravitational influences of the planets. Similar dynamics can be expected in other systems; in β Pictoris, for example, the disc is known to have gaps and rings inside $\lesssim 90$ AU from the star which indicates the presence of giant planets (Wahhaj et al. 2003). Lagrange et al. (2009) were able to directly image a gas giant (β Pictoris b) with a mass of $\sim 8\, M_{\rm Jup}$ and orbit semi-major axis of ~ 8 AU.

A more mysterious case is that of the previously mentioned exoplanet Fomalhaut b. It was first found by Kalas et al. (2008) by direct imaging with the HST. Their findings indicate a giant planet at a distance of 119 AU from the star. By assuming that this planet is the cause of the inner edge of the dust disc, dynamical modelling indicates that it should have a mass of $\lesssim 3$ M$_{\rm Jup}$.

Fomalhaut b's existence was questioned the next year by Marengo et al. (2009) when they attempted to observe it with *Spitzer* and were unable to detect it. So the original data was revisited and new observations were done with Subaru by Currie et al. (2012) who could indeed confirm a substellar object in orbit around Fomalhaut. They suggested a dust-enshrouded giant planet of $< 2\, M_{\rm Jup}$, and that the HST images were showing scattered light from a dust cloud associated with the planet. Kalas et al. (2013) have since made additional observations and studied possible orbits of the candidate planet. They found that Fomalhaut b is on a Keplerian orbit with high eccentricity, and possibly dust belt crossing. This is a highly interesting system to continue studying.

However, both β Pictoris and Fomalhaut are A-class stars. More observations and detections of dust around FGK-stars are required to find Solar system analogues. A nearby Solar-like star would be preferred so that higher resolution can be achieved.

One of the *Herschel* Space Observatory (see below) key-projects is called Dust around Nearby Stars (DUNES, P.I. C. Eiroa)[4]. It is dedicated to finding cold dust around nearby Solar-like stars (F, G, and K spectral classes), i.e. EKB analogues.

The obvious example of a nearby Solar-like star is the Solar neighbour α Centauri (α Cen). This is a binary with G2 V and K1 V stars (Kervella et al. 2003) at a distance of only 1.3 pc (Söderhjelm 1999) where the primary star is sometimes considered a Solar twin.

Simulations have shown that planetary formation is possible here despite its binary nature

[4] http://www.mpia-hd.mpg.de/DUNES/

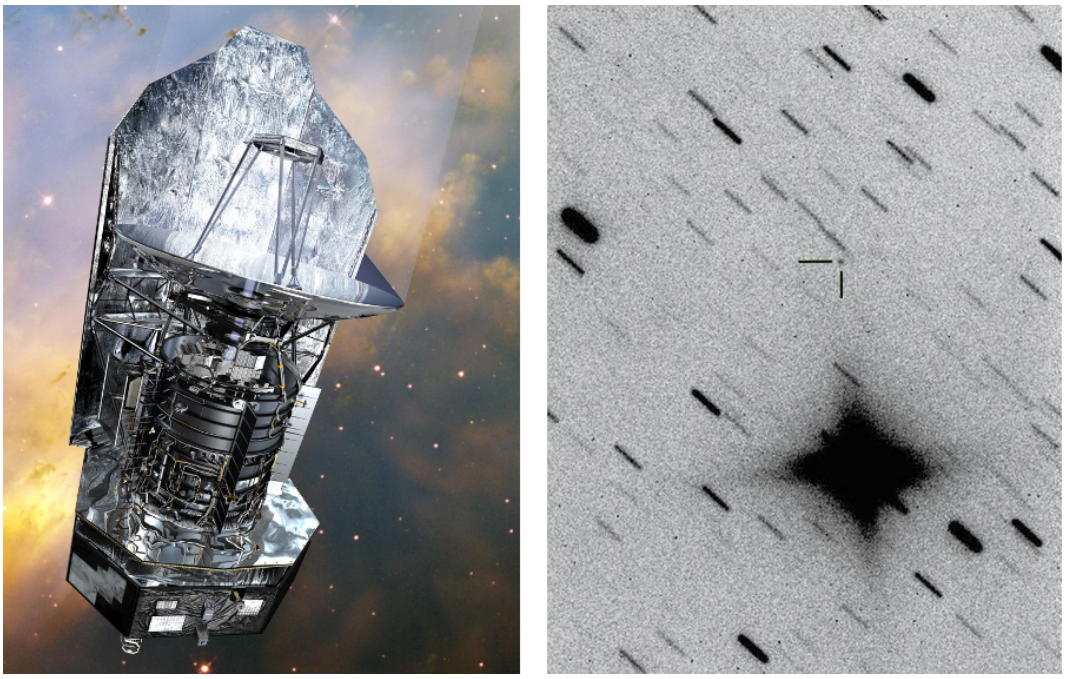

Figure 1.4: The left image is an artist impression of the *Herschel* Space Observatory, image credit: ESA/AOES Medialab. The right image is an observation of *Herschel* as it was being decommissioned, image credit: N. Howes and E. Guido at Faulkes Telescope/LCOGT, Hawaii.

(see Chapter 3). The higher than normal metallicity of both stars is also favours the possibility of planetary systems (Maldonado et al. 2012).

Holman & Wiegert 1999 showed that circumstellar orbits are stable inside ~ 2 to 3 AU of each star. A planet has been suggested to exist by Dumusque et al. (2012) around the companion star, α Centauri B, making this the nearest exoplanet candidate (previously it was the candidate ε Eridani b, Hatzes et al. 2000). However, this planet is difficult to detect with its Earth-like mass (only $1.3\,M_{\oplus}$, and a semi-major axis of 0.04 AU), and it has yet to be confirmed (Hatzes 2013; Demory et al. 2015; Rajpaul et al. 2016). Evidently it is possible for planets to exist around these stars and there is one candidate. The questions are then, how much dust is there, and what more we can learn by using α Centauri as a nearby laboratory?

1.4 *Herschel* Space Observatory

Herschel is an ESA far-infrared/submillimetre (FIR/submm) space telescope (Pilbratt et al. 2010) with a 3.5 m dish (see Figure 1.4). It was launched by ESA in May 2009 and put into orbit around the second Lagrangian point of the Earth-Sun system (L2). It ran out of liquid helium as planned (its main coolant) by the end of April 2013, as planned and was decommissioned later that same year.

It was equipped with two photometers, Photodetecting Array Camera and Spectrometer (PACS, Poglitsch et al. 2010) and Spectral and Photometric Imaging Receiver (SPIRE, Griffin et al. 2010, and one heterodyne instrument, Heterodyne Instrument for the Far Infrared (HIFI,

de Graauw et al. 2010).

PACS provided photometry at the wavelengths 70, 100, and 160 μm, useful for projects like DUNES. Exo-Kuiper belts can, for example, be expected to have their strongest emission at these wavelengths due to the temperature of dust at Kuiper belt-like distances to a Solar-like star. PACS 100 μm also provided the best combination of sensitivity and contrast to the star when searching for EKBs (Eiroa et al. 2013). SPIRE observations at 250, 350, and 500 μm could then complement the PACS observations to further constrain the shape of the Rayleigh-Jeans tail of the dust emission.

1.5 Structure of the thesis

This thesis is structured in the following way: Chapter 2 summarises the physics required to correctly model dust discs and their emission. Chapter 3 introduces Paper I on α Centauri, and adds new results based on simulations with higher resolution. Chapter 4 introduces Paper II with the work done on 94 Ceti. Chapter 5 summarises the work being done for Paper III on the coherently re-reduced combined DUNES data sets of Eiroa et al. (2013) and Montesinos et al. (2016). Modelling results on two interesting case studies from the DUNES catalogue are presented in Chapter 6; the stars EP Eridani (HIP 13402) and Gliese 42 (HIP 4148). The future prospects of my projects are finally discussed in Chapter 7.

Chapter 2

Physics of circumstellar dust

Planetary systems are highly dynamical and in constant evolution. Everything from the largest bodies such as gas giants, to the smallest planetesimals and dust grains are always interacting. In this chapter I summarise the most important physics used for modelling circumstellar discs. These are divided into two parts; dynamics (orbits and motions) of dust grains and radiative transfer through a dusty medium.

First of all, one must consider the system we are modelling. Is it a binary star and are there any large or small planets? This sets constraints that a realistic disc must satisfy and can also give indications of the dynamics in the disc, e.g. where we can expect to find the dust producing planetesimal rings. The location of the dust must also coincide with what dust temperatures we can infer from the observed dust emission. If this agreement can not be met for certain case studies, one may need to re-think the dust disc model or explore the possibility of background contamination.

Grain properties, which are directly dependent on the dust production, give us all the information we need to understand how the dust absorbs and emits radiation. This in turn gives us estimates on physical quantities, e.g. the total dust cloud mass. However, the grain properties might be the weakest part in the modelling, as these are most often based on assumptions. These assumptions are, however, based on previous studies and experiments. For example, there are studies where the contents of the Zodiacal cloud are studied directly, there are also laboratory experiments on how dust grains collide and fragment, and there are large scale simulations of collisions and disc dynamics (see e.g. Krivov 2010; Aumatell & Wurm 2011; Moro-Martín 2013). However, it is difficult to directly measure grain properties of dust around other stars. It is possible, in some circumstances, to constrain some of the grain properties (for example the constituents) by looking for certain resonances in the emission. However, more commonly the wavelength resolution is not sufficiently high and the observed data then agree with some simpler modified black body.

In this chapter I connect these points to summarise the radiative transfer in a dust disc and show observational implications these give. But first I describe the equations used, how they are interconnected, and how one can calculate useful physical quantities from the observations, with the help of all the assumptions.

2.1 Disc dynamics

The circumstellar dust considered in this thesis is purely what we refer to as debris, i.e. dust produced by collisions of planetesimals and larger grains in rings of *parent bodies*. It is not dust that is left from the protoplanetary disc (the proplyd), but a product of the continued evolution of the planetary system.

In the Solar system, for example, we have both the asteroid belt and the Kuiper belt that act as rings of parent bodies for production of dust. The dust from the asteroid belt either gains or loses angular momentum due to interaction with the radiation field from the Sun and the gravitational field from e.g. Jupiter.

The physics that affect the movement of dust grains are summarised in a simple equation of motion (see the reviews by Krivov 2010; Moro-Martín 2013). This can be written as the acceleration

$$\begin{aligned}\ddot{\boldsymbol{r}}_n = &- \frac{G\,M_\star}{r_n^3}\,(1-\mathcal{B}_n)\,\boldsymbol{r}_n \\ &- \frac{(1+SW)\,\mathcal{B}_n}{c}\,\frac{G\,M_\star}{r_n^2}\,(\dot{r}_n\,\hat{r}+\dot{\boldsymbol{r}}_n) \\ &+ \sum_i \frac{G\,m_i}{|\boldsymbol{r}_i-\boldsymbol{r}_n|^3}\,(\boldsymbol{r}_i-\boldsymbol{r}_n)\end{aligned} \tag{2.1}$$

for each dust grain n. $M_\star$ is the mass of the central star, G is Newton's gravitational constant, $\boldsymbol{r}_n$ is the grain's position relative to the star, r_n is the radial distance between the star and dust grain, m_i is the mass of any planet in the system, and the rest of the terms are described below.

The equation is divided into three parts. The first line describes the gravitational influences from the central star and how that is reduced by radiation pressure. The second line describes Poynting-Robertson (PR) drag and stellar wind (SW) drag. Finally, the third line describes gravitational influences from surrounding planets.

The parameter $\mathcal{B}_n$ is the ratio between radiation pressure and gravitation exhibited on particle n from the central star, and SW is the ratio between SW drag and PR drag (for the Sun about one third, $\sim 0.2-0.3$, Gustafson 1994).

The radiation pressure quite simply counteracts the grain's orbit of the central star. A grain released from a parent body in a circular orbit will be bound into an elliptical orbit if $\mathcal{B}_n \leq 0.5$ (see Figure 2.1). Larger $\mathcal{B}_n$ will result in escape trajectories ($0.5 < \mathcal{B}_n < 1$ gives hyperbolic trajectories). The boundary between bound orbits and escape trajectories is somewhat smeared if the parent body has an elliptical orbit. However, all grains with $\mathcal{B}_n < 1$ have some kind of Keplerian trajectory (Krivov 2010). This provides one way of finding a lower limit of the size of the dust grains (a_n), because $\mathcal{B}_n$ depends on a_n, through

$$\mathcal{B}_n \equiv \frac{F_{\rm rad}}{F_{\rm grav}} = \frac{3}{16\,\pi\,c}\frac{L_\star}{G\,M_\star}\frac{1}{\rho_n a_n} \tag{2.2}$$

under the assumption of full absorption by the grain. The $L_\star$ is the luminosity of the star and ρ_n is the mass density of the grain.

The PR drag term instead counteracts the forward motion of the grains. As a grain orbits the central star it also moves through the radiation field. This results in loss of angular

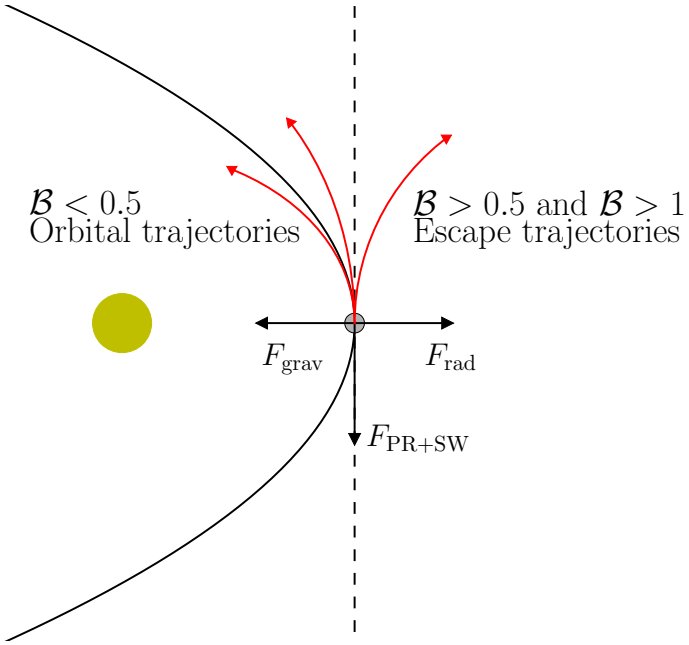

Figure 2.1: Schematic representation of the forces included in Equation 2.1 (not including the gravitational influences from planets). Curved red arrows represent possible trajectories of a dust grain released from a parent body in a circular orbit. The area left of the black curve (orbital trajectories) is where $\mathcal{B} \leq 0.5$, the intermediate area inside the dashed line (hyperbolic escape-trajectories) is where $1 > \mathcal{B} > 0.5$, and the outer area (also escape trajectories) is where $\mathcal{B} > 1$.

momentum and thus also a decreasing semi-major axis, or a spiral motion inwards towards the star. The PR drag affects primarily larger grains (1 μm to 1 mm), while smaller grains ($<$ 1 μm) are more affected by the outward-pushing radiation pressure.

Stellar wind can also provide both an outward pushing pressure force, and a counteracting drag force. The stellar wind's outward pushing pressure is often negligible when compare to the radiation pressure, however, it is not possible to totally ignore the SW drag. Stellar wind forces can, for example, be very important for dust around late-type stars, i.e. red dwarfs (Krivov 2010; Moro-Martín 2013).

The combination of these forces results in the expectation to see smaller grains in the outer part of a disc, and larger grains in the inner parts of the disc (Thébault et al. 2010).

Much work has already been done on studying the dynamics and evolution of dust discs. We see examples of particle based work by e.g. Stark & Kuchner (2008); Thébault (2012). Fluid dynamical models are also implemented, see e.g. Krivov et al. (2006); Thébault & Augereau (2007). Additionally, extensive work has been done on planet-disc interaction and the detectability of possible gaps (see e.g. Regály et al. 2012; Ertel et al. 2012; Su & Rieke 2014).

However, in some cases it is sufficient to just study the gravitational force's influences on the dust disc, to e.g. find possible disc sizes in binary (or more multiple) systems and/or systems with giant planets.

Table 2.1: List of grain properties

Mass density (ρ)	$1 - 5\,\mathrm{g\,cm^{-3}}$ $^{(a)}$
Lower size limit (a_{min})	$\sim 6\,a_{\mathrm{blow-out}}$, Equation 2.3
Upper size limit (a_{max})	1 mm
Temperature/radial distance ($T_{\mathrm{dust}}/r_{\mathrm{grain}}$)	Approximated by Equation 2.8
Snow line	Equations 2.5 through 2.7
Evaporation temperature (T_{vap})	$\sim 1500\,\mathrm{K}^{(a,b)}$

References. $^{(a)}$ Moro-Martín (2013). $^{(b)}$ Pollack et al. (1994).

2.2 Grain properties

A number of grain properties were already seen in Equations 2.1 and 2.2. These properties are microscopic and can sometimes even be studied in laboratories. They are also essential for the understanding of both the global dynamics of the disc, and the radiative transfer in the disc that in the end will give correct dust emission models. These properties are summarised in Table 2.1.

The first property mentioned before was the grain size, a_n. As already shown, the size affects the orbital dynamics of the grain. However, the allowed range of sizes and the size distribution also affect opacity and the radiative transfer (described later), and the total mass of the dust disc. This is because the small grains are the primary absorbers and re-emitters in a disc, while the larger grains hold the majority of the total disc mass.

The size range is often, in the literature, limited to be $\lesssim 1$ mm since larger grains do not contribute much to the thermal emission, and using the same limit is useful when comparing results with other studies. The reason for this effect is a combined effect related to extinction coefficients, and these are discussed in Section 2.3. It can be summarised, though, by the fact that absorption tends to be smaller for larger grains (see several studies, e.g. Miyake & Nakagawa 1993; Draine 2006; Kataoka et al. 2014), due to that the total dust grain surface area in a cloud of small grains is much larger than the total grain surface area of a cloud of large grains and similar total dust mass. This way we effectively exclude any larger grains and planetesimals.

The lower size limit is often estimated by inferring the blow-out radius ($a_{\mathrm{blow-out}}$). The blow-out radius is the smallest radius possible for grains to have stable orbits, i.e. grains that are large enough not to be affected by the combined effects of the radiation field and stellar wind from the central star (Strubbe & Chiang 2006; Plavchan et al. 2009; Krivov 2010). This can be estimated from

$$a_{\mathrm{blow-out}} \approx \frac{3}{8\,\pi\,G\,M_\star\,\rho_{\mathrm{grain}}} \left(\frac{L_\star}{c} + \dot{M}_\star v_{\mathrm{SW}} \right) \tag{2.3}$$

where the first term inside the parenthesis is the radiative momentum rate, and the second term is the mechanical momentum rate. However, the stellar mass loss rate ($\dot{M}_\star$) of e.g. α Cen A is close to that of the Sun, i.e. $2 \times 10^{-14}\,M_\odot\,\mathrm{yr}^{-1}$, and the average wind speed (v_{SW}) is roughly $\sim 400\,\mathrm{km\,s^{-1}}$ (Wood et al. 2001, 2005). The right term is negligible when compared to the left term, and we can approximate $a_{\mathrm{blow-out}}$ by setting $0.5 = \mathcal{B}_n$ in Equation 2.2

and solving it for a_n.

It has also been shown through simulations that the lower cut-off is smooth (Wyatt et al. 2011; Löhne et al. 2012). A better approximation of the smallest allowed grains would be around six times the blow-out radius, $a_{\min} \sim 6\, a_{\mathrm{blow-out}}$.

Furthermore, the emission at wavelength λ is dominated by grains of sizes around $\lambda/(2\,\pi)$. So at e.g. $\lambda = 100\,\mu$m we primarily observe grains of sizes around 10 to 20 μm.

Grain sizes are most commonly assumed to be distributed as a power-law (Dohnanyi 1969) on the form

$$n(a_n) \propto a_n^{-q} \tag{2.4}$$

in cases of collisionally dominated discs as the Zodiacal cloud. Similar power-law distributions are also assumed for interstellar dust (Mathis et al. 1977). Dohnanyi (1969) found that $q = 3.5$, a number that is often cited for dust modelling. Similar power-law distributions have been found since then, with the help of simulations in a number of studies. More recently e.g. Bernstein et al. (2004) who found $q = 4 \pm 0.5$ for the Kuiper belt, and Gáspár et al. (2012) who found $q = 3.65$. Other recent simulations (e.g. Krivov et al. 2006; Thébault & Augereau 2007; Löhne et al. 2008; Kral et al. 2013; Krivov et al. 2013) find deviations from the power law, however, averages of these variations are still consistent with the steady state of Dohnanyi (1969). The value $q = 3.5$ is initially, and generally, assumed in this thesis since this is a "standard" value and is also more easily compared with other studies using the same assumption.

A final note on the size distribution (Equation 2.4) is that the grain sizes tend to be inhomogeneously distributed throughout the disc. Smaller grains tend to be more abundant in the outer parts of the disc and they may even temporarily recide in dynamically unstable regions. This is due to collisions and the radiation pressure (see e.g. Thébault et al. 2010). However, we have so far mainly studied grains that are large enough not to be heavily affected by non-gravitational forces, and homogeneous distributions are hereafter assumed for simplicity.

Finally, we have ρ, the average grain mass density. This is important for e.g. the previously described dynamics, the total dust mass, and the optical properties. It can vary, but is typically somewhat smaller than Earth's mean mass density ($5.5\,\mathrm{g\,cm^{-3}}$), between 1 to $5\,\mathrm{g\,cm^{-3}}$ (Moro-Martín 2013) depending on their constituents. A mix of graphite and silicate is often assumed, with or without water ice, and sometimes with iron. Mostly we are forced to just assume something based on what is known about the Zodiacal dust and what has been used in other studies, for easier comparison.

One can, for example, investigate the possibility of icy grains in the disc. This can be done by calculating the radius of the snow line, inside which any ice will sublimate. Discs that are dynamically limited to smaller radii may be inside the snow line and thus not harbour any icy grains, which in turn limits realistic choices of dust opacities and albedo.

Artymowicz (1997) states that the snow line can be defined as the largest radial distance from a star at which the sublimation time scale is shorter than all other relevant time scales of the system. An upper limit time scale is the age of the system (some 10^9 yr for Solar-like stars) whereas a lower limit can be the orbital period of the grains. The sublimation time scale can be written as (Lamy 1974; Grigorieva et al. 2007)

$$t_{\rm sub} = \frac{a_0\,\rho\,\eta}{\Phi} \tag{2.5}$$

where a_0 is the initial grain size before sublimation (e.g. 1 mm), and η is the covering factor (fraction of the grain covered with ice). Φ can in turn be written as

$$\Phi = 3.06 \times 10^{-4} \left(\mu\,\frac{P_{\rm sat}}{T}\right)^{1/2} {\rm g\,cm^{-2}\,s^{-1}} \tag{2.6}$$

where μ is the atomic weight of water (18 u). The saturation pressure of water vapour, $P_{\rm sat}$ is written within two temperature ranges as

$$\begin{cases} P_{\rm sat} &= 3.56 \times 10^{12}\,\exp\left(-\frac{6141.67}{T}\right)\,{\rm Pa};\ \text{when}\,T \geq 170\,{\rm K} \\ P_{\rm sat} &= 7.59 \times 10^{14}\,\exp\left(-\frac{7043.51}{T}\right)\,{\rm Pa};\ \text{when}\,T < 170\,{\rm K} \end{cases} \tag{2.7}$$

see equations 2 and 3 in Grigorieva et al. (2007). Note that the unit in Equations 2.6 and 2.7 have here been changed from torr (as was used by Grigorieva et al. 2007) to Pa.

Finally, to estimate which radial distance each temperature corresponds to, we use (Liseau et al. 2008)

$$T = T_\star \left(\frac{R_\star}{2\,r_{\rm grain}}\right)^{1/2} \left(\frac{Q_{\rm abs}}{Q_{\rm em}}\right)^{1/4} \tag{2.8}$$

where $T_\star$ is the effective temperature of the central star, $R_\star$ is the stellar radius, $r_{\rm grain}$ is the semi-major axis of an orbiting grain, and $Q_{\rm abs}$ and $Q_{\rm em}$ are the absorption and emission coefficients (see further details on optical properties of grains in the next section).

2.3 Dust emission

We assume that Kirchhoff's law for thermal radiation, i.e. thermal equilibrium, is true (what is absorbed is also emitted), that the dust consists of spherical grains, and initially that the discs are optically thin (see the reviews by Zuckerman 2001; Wyatt 2008; Krivov 2010). This can be described with an energy balance equation, $dE_{\rm abs}/dt = dE_{\rm emit}/dt$, where the cooling term for dust is

$$S_{\rm dust}(\nu) = \int\int 4\,\pi\,a^2\,Q_{\rm abs}(a)\,\frac{\pi\,B_\nu[T(a,\boldsymbol{r})]}{4\,\pi\,D^2}\,n(a,\boldsymbol{r})\,da\,d\boldsymbol{r}^3 \tag{2.9}$$

which also describes the amount of dust emission received at Earth from the distance D. Here we see how several of the dust properties described earlier are used to describe their emission, e.g., the grain size a, density ρ, and absorption efficiency $Q_{\rm abs}(a)$. Dust temperatures are included in the black body function $B_\nu[T(a,\boldsymbol{r})]$, and the number density is a function of grain size and position $n(a,\boldsymbol{r})$.

The absorption efficiency is a unitless parameter connected to the absorption cross-section ($C_{\rm abs}$ [cm^2]) and mass absorption coefficient ($\kappa_{\rm abs}$ [cm^{2}g^{-1}]) through

$$Q_{\rm abs} = \frac{4}{3}\,\frac{C_{\rm abs}}{a^2} = \kappa_{\rm abs}\,\frac{4a\rho}{3}. \tag{2.10}$$

Furthermore, absorption, extinction, and albedo are all interrelated through

$$\begin{cases} \kappa_{\rm ext} &= \kappa_{\rm abs} + \kappa_{\rm scat} \\ \kappa_{\rm abs} &= \kappa_{\rm ext}\,(1-\eta) \\ \kappa_{\rm scat} &= \kappa_{\rm ext}\,\eta \end{cases} \tag{2.11}$$

where η is the albedo of the grains and $\kappa_{\rm scat}$ is the corresponding mass scattering coefficient. All of these opacity coefficients are also functions of frequency. The computation of these belong to a major field where the effects of e.g. grain composition, grain shape ("fluffiness"), and coatings of ice are studied (e.g. resonances and molecular lines in the extinction curves). Several good references for the interested reader are Draine (1988); Miyake & Nakagawa (1993); Krügel & Siebenmorgen (1994); Weingartner & Draine (2001); Draine (2003); Zubko et al. (2004); Draine (2006); Kataoka et al. (2014).

These studies give ample supply of results to estimate these coefficients when modelling dust emission. We usually just use results for compact, bare grains (spherical, non-porous). This is because we simply do not know most of these characteristics of exodebris, as it would require in situ experiments, so we are forced to apply simpler assumptions.

However, it is possible to study interplanetary dust particles (IPDs) caught by the Earth (see Moro-Martín 2013 and references therein). These grains often have irregular, porous shapes, contain silicates, and have mass densities around $1-3\,\mathrm{g\,cm^{-3}}$. The *Voyager* 1 probe, when traversing the outer parts of the Solar system, detected dust in the Kuiper belt region ($>$ 30 AU) with a number density of $\sim 2\times10^{-8}\,\mathrm{m^{-3}}$. These data are, however, poorly calibrated, and they say nothing on the shape or contents of the grains except that the smallest grains detected were $\sim 2\,\mu$m size. While writing this it was one year since *New Horizons* made its flyby of Pluto, and the probe is expected to spend at least a decade exploring the Kuiper belt. It is also planned to make a flyby of the Kuiper belt object (KBO) 2014 $\mathrm{MU_{69}}$ (PT1) in January, 2019, and will undoubtedly significantly expand our knowledge of the Kuiper belt's small and large components.

It is possible to infer a total dust mass from simpler emission models by using some drastic, but sometimes useful, approximations. By assuming isothermal dust in a ring around the star, a ring which only contains grains of one constant size, we can follow Hildebrand (1983) and re-write Equation 2.9 as

$$S_{\rm dust}(\nu) \approx \pi\, a^2\, Q_{\rm abs}(a)\, \frac{B_\nu(T_{\rm dust})}{D^2} N_{\rm tot} \tag{2.12}$$

where $N_{\rm tot}$ denotes the total number of dust grains in the ring. Skipping a few steps, we can find that the total disc mass ($M_{\rm dust}$) of an isothermal ring with grains of size a is

$$M_{\rm dust} = \frac{4\,a\,\rho}{3}\,\frac{S_{\rm dust}(\nu)\,D^2}{Q_{\rm abs}\,B_\nu(T_{\rm dust})} = \frac{S_{\rm dust}(\nu)\,D^2}{\kappa_{\rm abs}\,B_\nu(T_{\rm dust})}. \tag{2.13}$$

Equation 2.12 can also be simplified into a modified black body formulated as

$$S_{\rm dust} \approx B_\nu(T_{\rm dust})\,\left(\frac{\nu}{\nu_0}\right)^\beta \times \mathcal{D} \tag{2.14}$$

where $\mathcal{D}$ incorporates the grain properties, optical properties, dust mass, and distance from us to the star. The parameters β and ν_0 are due to the wavelength dependence of the extinction coefficients, where β is usually found to be smaller than 2 and valid for frequencies smaller than the cut-off ν_0.

Such approximations can be expanded by assuming several rings to fit the models to observed dust emission. However, it is also possible to apply more advanced radiative transfer simulations when more precise disc and dust models are used.

2.3.1 Background contamination

Extrasolar EKB-analogues are primarily observed at wavelengths around 100 μm. The sensitivity to the emission of dust with temperatures of $\sim$30 K and the contrast between the dust and the host star are both higher at this wavelength. However, background confusion is also an important issue at 100 and 160 μm. For example, dust emission from high-redshift galaxies may have significant flux density at this wavelength which could be misinterpreted as part of the disc emission.

The probability of chance alignment with background galaxies has for these reasons been estimated, based on number counts by e.g. Berta et al. (2011) (see their figure 7). In the literature we can find varying numbers, due to varying flux density limits and wavelengths. Eiroa et al. (2013) find for their cases a probability of just 1.2% , while Krivov et al. (2013) find the higher 4.8% for their studies of the coldest dust disc detected so far (at 160 μm and higher). In Paper II we estimate it for the case of 94 Cet and find a value of 2.3% . In effect, there seems to be a relatively low, but not insignificant, chance of alignment with background galaxies.

2.3.2 Emission modelling with RADMC-3D

In this project we have used the Monte-Carlo based 3D radiative transfer program RADMC-3D, written by Dullemond (2012)[1], to simulate dust emission. This program requires inputs of opacities, disc shape, positions and spectra of stars, and the output can be either SEDs or synthetic images as seen from any direction. It suits our needs when modelling dust emission from multiple star systems. It is easy to add more stars, their positions in- and outside the grid of dust, and photospheric spectral models of the stars.

The usage of radiative transfer programs is in particular useful in cases where the medium is optically thick. We expect debris discs to be optically thin, especially at those wavelengths we observe the emission. However, the disc is primarily heated at optical wavelengths, where the extinction is higher. If we estimate the optical thickness, we find that most cases of "normal" discs (with dust cloud densities of 10^{-20} – 10^{-19} g cm^{-3}) are in fact optically thin also at optical wavelengths.

In multiple star systems as e.g. α Cen (with Paper I) and 94 Cet (Paper II), the dynamics can often result in very radially constrained disc possibilities. In these cases we may have to use higher cloud densities, and risk having optically thick dust clouds. In such dense clouds we would risk overestimating the emission at FIR wavelengths without radiative transfer simulations.

[1] http://www.ita.uni-heidelberg.de/~dullemond/software/radmc-3d/

RADMC-3D does not include any previous assumptions on dust grain properties, dust masses, or disc shape. To run the program we need to include; (i) stellar spectra and positions, (ii) a 3D grid of dust mass densities, i.e. total dust mass is here one of the input parameters, and (iii) dust opacity properties, i.e. mass absorption and mass scattering coefficients, $\kappa_{\rm abs}$ and $\kappa_{\rm scat}$.

The DUNES team has the stellar spectrum of each star in the catalogue[2]. They were computed through an adapted PHOENIX/GAIA grid (Brott & Hauschildt 2005). The positions of the stars are based on their orbits and observations.

The grid of dust mass densities can be filled by using results from particle simulations. By assuming a total dust mass, radial power law density distribution, and homogeneous radial particle size distribution (in fact by approximating the dust dynamics to the simplest model) we obtain a 3D distribution of masses with "soft" edges due to the gravitational interaction of the other components. The radial surface density distribution can be adapted to the form $\Sigma = \Sigma_0 \left(R/R_0\right)^{-\gamma}$. The final step is just to insert a grid and find how much mass there is in each grid cube, which directly gives us the total mass density at each grid coordinate.

The mass absorption coefficient includes the grain size limits, grain size distribution, and grain mass density, i.e. $\kappa_{\rm abs}(a_{\rm min}, a_{\rm max}, q, \rho)$, where q is from the grain size distribution in Equation 2.4. Suitable absorptions can be found in the literature (see Section 2.3).

The albedo is more complicated. However, by computing the radii of the snow lines (Equations 2.5 through 2.8) in the system it is possible to at least select an albedo model that fits the possible ice contents of the proposed discs. Miyake & Nakagawa (1993) and Inoue et al. (2008) studied the albedo of grains with different sizes and with/without ice covering. Small silicate particles ($a \lesssim 10\,\mu$m) have a relatively stable albedo (between 0.5 and 0.6) which then drops down to zero at longer wavelengths (between 100 to 500 μm).

RADMC-3D works by sending out 10^5 photons in random directions from each star. These interact with the dust mass density grid (isotropic scattering is the default setting). The program must first compute a temperature model in the grid, before it can produce SEDs and images. This is all described in detail in the manual that is available at the program's homepage.

2.4 Disc size estimation

The disc size can obviously be observed directly in cases where the dust emission is resolved around the star. However, this requires that the disc is large enough, that the star is nearby enough, and that the telescope has sufficient sensitivity to detect the weak extended emission.

In most cases, however, the excess sources are point sources. Then it is common to infer the disc extent directly from the dust emission temperature (Equation 2.8). Using the black body assumption ($Q_{\rm abs} = Q_{\rm em}$), we can infer a black body disc radius of

$$R_{\rm BB} = \frac{R_\star}{2}\left(\frac{T_\star}{T_{\rm dust}}\right)^2 \tag{2.15}$$

which can be rewritten to

[2] http://sdc.cab.inta-csic.es/dunes/jsp/masterTableForm.jsp

$$R_{\rm BB} = \left(\frac{278\,{\rm K}}{T_{\rm dust}}\right)^2 \left(\frac{L_\star}{L_\odot}\right)^{0.5} {\rm AU} \tag{2.16}$$

where $L_\star$ is the total luminosity of the central star, and $T_{\rm dust}$ can be estimated from Wien's displacement law (for spectral flux per unit frequency) as

$$T_{\rm dust} = 5100\,{\rm K} \times \frac{1\mu{\rm m}}{\lambda_{\rm max}} \tag{2.17}$$

with $\lambda_{\rm max}$ as the wavelength of the peak of the dust emission.

However, Pawellek et al. (2014); Pawellek & Krivov (2015) compared the sizes of resolved discs with their black body radii to find how the dust emission temperature is related to the disc size. They varied the grain properties and parametrised this with a "real" disc radius as

$$R_{\rm real} = \Gamma \times R_{\rm BB} \tag{2.18}$$

where

$$\Gamma = A \times \left(\frac{L_\star}{L_\odot}\right)^B \tag{2.19}$$

where estimates of the parameters A and B are presented in Table 4 of Pawellek & Krivov (2015). A varies between 5 and 8, and B between -0.3 to -0.6, depending on grain constituents. They warn, however, that the commonly used artificial dust material, known as "astrosilicate", predicts too large discs for Solar-like stars.

Chapter 3

Introduction to Paper I: α Centauri

In this chapter I summarise the work done in Paper I, its relation to Liseau et al. (2013), and present some additional details on the simulations and modelling, as well as some results that were not published in Paper I.

At a distance of only 1.3 pc (Söderhjelm 1999), $\alpha\,\mathrm{Cen}$ is the nearest stellar neighbour. This system can provide a unique opportunity to study dust discs and exoplanetary systems around Solar-like stars in detail.

This is a binary system with the primary, $\alpha\,\mathrm{Cen\,A}$ (a G2 V star), and the companion $\alpha\,\mathrm{Cen\,B}$ (a K1 V star) on an 80 yr orbit with a semi-major axis of $\sim$ 24 AU (Torres et al. 2010; Pourbaix et al. 2002). Proxima Centauri (an M6 V star) shares a similar proper motion and seems to be bound to $\alpha\,\mathrm{Cen}$ AB, but with a separation of $\sim$ 15 000 AU (2° southwest from the binary). Assuming a circular orbit gives Proxima Cen a period of roughly 1.3 Myr. Together with Proxima Centauri, the $\alpha\,\mathrm{Cen}$ system is a triple star system and Proxima Cen is sometimes called $\alpha\,\mathrm{Cen\,C}$ for this reason. Because Proxima Cen is currently between the Sun and $\alpha\,\mathrm{Cen}$ AB, it is the nearest known neighbour of the Sun.

Proxima Cen was very recently the subject of much attention due to the discovery by the Pale Red Dot project of a probably rocky planet in its temperate zone (Anglada-Escudé et al. 2016).

The binary $\alpha\,\mathrm{Cen}$ is one of the brightest stars on the night sky and the brightest in the constellation of Centaurus. It is also known as Rigil Kentaurus (or Rigil Kent), as it is supposed to be the "foot of the Centaur". $\alpha\,\mathrm{Cen\,A}$ has the catalogue designations HD 128620 and HIP 71683, and $\alpha\,\mathrm{Cen\,B}$ has HD 128621 and HIP 71681, and is located on the southern hemisphere at declination $-61°$, in the direction of the galactic plane.

The orbit of the stars allows for circumstellar stable orbits to exist inside $2-4$ AU of each star (Holman & Wiegert 1999), and for circumbinary orbits to exist at radii $\gtrsim 75$ AU from their barycenter (Wiegert & Holman 1997). Consequently, these are the sizes of the three dynamically stable regions.

Are these regions large enough to have allowed planetary formation? We know that binarity is not necessarily an obstacle for this as more than 12 % of detected exoplanets are in

multiple systems (Röll et al. 2012)[1]. The stars also have higher metallicities than the Sun (Maldonado et al. 2012) which is an argument for possible rocky exoplanets. Furthermore, simulations have also shown that planetary formation is possible in a binary system. For example, Thébault et al. (2009) showed that planetary formation around $\alpha\,\mathrm{Cen\,B}$ is possible, but only in the inner parts of the stable zone at $\lesssim 0.5 - 0.75$ AU, i.e. at the inner edge of the $\alpha\,\mathrm{Cen\,B}$ habitable zone ($0.5 - 0.9$ AU). More optimistic estimates (Paardekooper & Leinhardt 2010; Xie et al. 2010) give the range of $1 - 1.5$ AU. However, the current orbit of any planets may not coincide with that at formation due to migration. This can act in both directions, meaning that planets may reside at any semi-major axis inside the stable regions.

Limited circumstellar planetary systems are clearly possible around the $\alpha\,\mathrm{Cen}$ stars. Radial velocity measurements have shown that an upper limit of planetary masses is $2.5\,M_{\mathrm{Jup}}$ inside 4 AU of either star (Endl et al. 2001). More recently Dumusque et al. (2012) presented results from their substantial radial velocity data set from which they suggest an Earth-like planet of $1.13\,M_{\oplus}$ around $\alpha\,\mathrm{Cen\,B}$ with a semi-major axis of 0.04 AU, denoted $\alpha\,\mathrm{Cen\,Bb}$ (see Section 1.3 for more discussion on this planet).

The $\alpha\,\mathrm{Cen}$ system is extremely nearby and interesting, and with potential for associated planets. With this in mind, we and DUNES used observations from *Herschel*, *Spitzer*, and the Atacama Pathfinder Experiment (APEX)[2] to investigate possible amounts of dust around these stars.

APEX is a 12-m mm/submm-telescope located at 5105 m altitude on the Llano de Chajnantor in Chile. The telescope pointing accuracy is $2''$ and it is equipped with heterodyne receivers and bolometer arrays. The Large APEX BOlometer CAmera (LABOCA, Siringo et al. 2009) has an operating wavelength of 870 μm centred on a 150 μm wide window. The 295 bolometers in LABOCA yield a circular field of view of $11\farcm4$ and the telescope beam FWHM at this frequency is $18\farcs1$.

3.1 Binary dynamics and simulations

Previous work on the dynamics of $\alpha\,\mathrm{Cen\,AB}$ resulted in a semi-analytical expression that describes the semi-major axis of stable circumstellar orbits around each star (Holman & Wiegert 1999). The largest stable semi-major axis (hereafter the critical semi-major axis, r_{crit}) around $\alpha\,\mathrm{Cen\,A}$ can be written as

$$r_{\mathrm{crit}} = \left(c_1 + c_2\,\mu + c_3\,e + c_4\,\mu\,e + c_5\,e^2 + c_6\,\mu\,e^2\right)\,r_{\mathrm{AB}} \tag{3.1}$$

where $\mu = M_{\mathrm{B}}/(M_{\mathrm{A}} + M_{\mathrm{B}})$, i.e. the fractional mass of the binary companion (reverse the masses in μ to find the r_{crit} around $\alpha\,\mathrm{Cen\,B}$), e is the binary eccentricity, r_{AB} is the binary semi-major axis, and c_1 through c_6 are coefficients computed by Holman & Wiegert (1999). Equation 3.1 was first computed from simulations of the $\alpha\,\mathrm{Cen}$-system which makes it convenient for our purposes. However, the large error bars for r_{crit} prompted us to verify the accuracy of the expression with our own simulations.

Using known properties of the system (see Table 3.1) and the given c_1 to c_6 coefficients of Holman & Wiegert (1999), we could calculate the critical semi-major axis for each star,

[1] This number may be reduced to $\sim 5\%$ based on recent statistics at `http://www.openexoplanetcatalogue.com/`

[2] `http://www.apex-telescope.org/telescope/`

Table 3.1: Properties of the α Centauri binary

	α Cen A	α Cen B
Sp.type[a]	G2 V	K1 V
$T_{\rm eff}$ (K)[b]	5824 ± 24	5223 ± 62
$L_{\rm star}$ ($L_\odot$)[b]	$1.549^{+0.029}_{-0.028}$	$0.498^{+0.025}_{-0.024}$
$M_{\rm star}$ ($M_\odot$)[bc]	1.105 ± 0.007	0.934 ± 0.006
$R_{\rm star}$ ($R_\odot$)[a]	1.224 ± 0.003	0.863 ± 0.005
$r_{\rm crit}$ (AU)[d]	2.778 ± 1.476	2.522 ± 1.598
$\log g$ [b]	4.3059	4.5364
[Fe/H][c]	+0.195	+0.231
Common parameters		
Inclination to LOS, i (°)[c]	79.20 ± 0.04	
Arg. of periapsis, ω (°)[c]	231.65 ± 0.08	
Long. of asc. node, Ω (°)[c]	204.85 ± 0.08	
Period (yr)[bc]	79.91 ± 0.01	
Eccentricity[c]	0.5179 ± 0.0008	
Semi-major axis, $r_{\rm AB}$ (AU)[c]	23.684 ± 0.64	
Distance (pc)[b]	1.348 ± 0.035	
Age (yr)[e]	$(4.85 \pm 0.50) \times 10^9$	

References. [(a)] Kervella et al. (2003); [(b)] Torres et al. (2010); [(c)] Pourbaix et al. (2002); [(d)] Holman & Wiegert (1999); [(e)] Thévenin et al. (2002).

denoted $r_{\rm crit}$ in Table 3.1, again roughly 2 to 4 AU for each star. It can be noted for future studies that the parallax and stellar masses were recently updated by Pourbaix & Boffin (2016).

Finally we also know that any circumbinary orbits are stable outside $\gtrsim 70 - 75$ AU (e.g. Wiegert & Holman (1997) and Jaime et al. (2012)). These size limits give us realistic temperature limits for any dust emission.

We created a code[3] to run complementing simulations. These solved the restricted three-body problem, i.e. massless particles in motion around the two stars in 3 dimensions. The three disc possibilities, two circumstellar and one circumbinary, were simulated separately and the stellar orbits were part of the simulation (as a small validity test).

Initial conditions were varied for the circumstellar and circumbinary runs. The circumstellar discs had 10^4 massless particles on initially circular orbits around the relevant star, and at most 5 AU from the star. The initial particle surface distribution was homogeneous, and we varied the thickness. Different thickness settings were tested, including no thickness, Gaussian distribution with a standard deviation of 0.5 AU, and a flaring disc with thickness $0.1 \times R$. These simulations were in general run with a timestep of 0.01 yr for 10^3 binary periods, i.e. 8×10^4 yr. Longer runs were also made with e.g. 10^4 periods to test the stability.

The circumbinary runs had discs with outer radii of 100 AU and 200 AU and a Gaussian distributed thickness of 5 and 10 AU respectively. The particles were initially set on circular

[3] Runge-Kutta 4 written in C

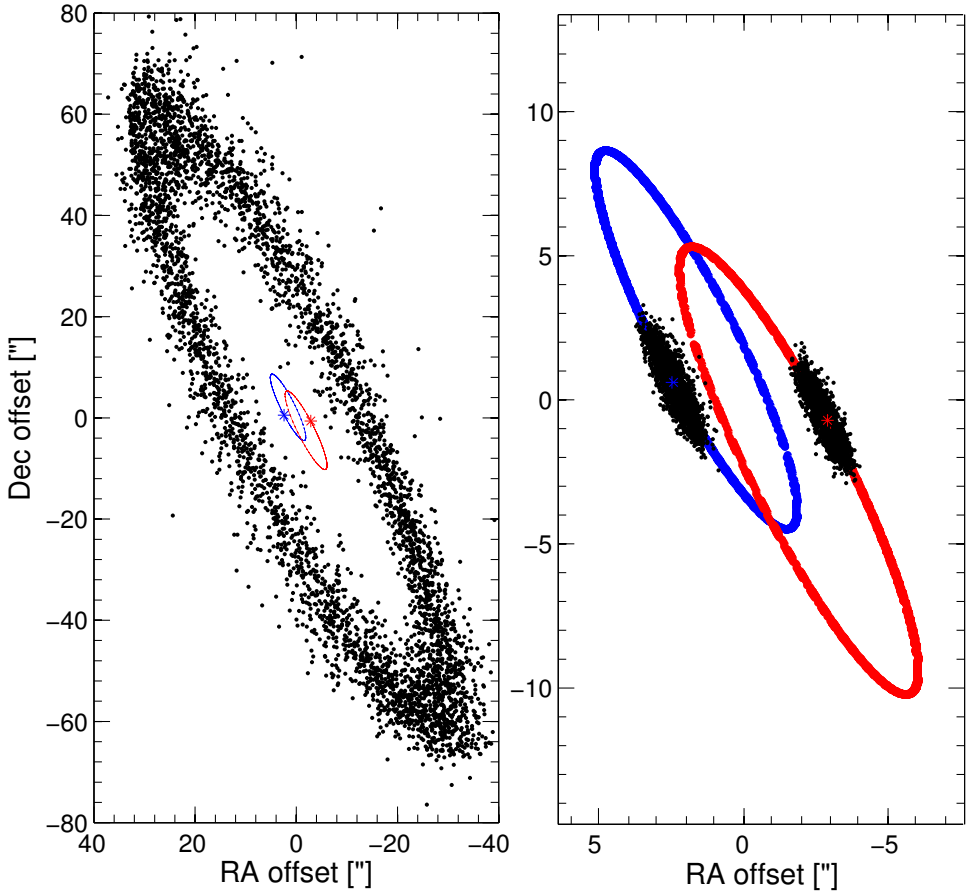

Figure 3.1: **Left:** circumbinary test particle disc in the stellar orbital plane as seen from the Earth. Outer radius is ~ 100 AU. **Right:** circumstellar test particle discs as seen from the Earth. Blue is for the hotter α Cen A, red is for the colder α Cen B, and their orbits.

orbits around the stellar barycenter and they were distributed homogeneously. For these larger discs a time step of 0.1 yr was sufficient and the simulations were left running for 10^3 periods. Longer runs were tested with e.g. 2×10^4 periods.

Results from these runs can be seen in Figures 3.1 and 3.2. Here we see how accurate the previously cited radii are. The critical semi-major axes were formulated with large uncertainties to make the expression useful for others binaries than just α Cen.

Additional circumstellar disc simulations were done with even higher time step resolution but smaller radii. The reason for this was to fill the inner parts of the circumstellar discs with particles, ranges that the previous simulations had too low resolution to be able to correctly simulate. These had an outer radius of just 1 AU, a timestep of 10^{-4} yr to reach inner radii of 0.03 AU, and were only run for 10 binary periods. The final states of these discs could be combined with the larger circumstellar discs which instead have correctly simulated outer edges.

However, the discovery of the exoplanet α Cen Bb (Dumusque et al. 2012, discussed in Section 1.3) could complicate the high resolution small disc around α Cen B. This planet

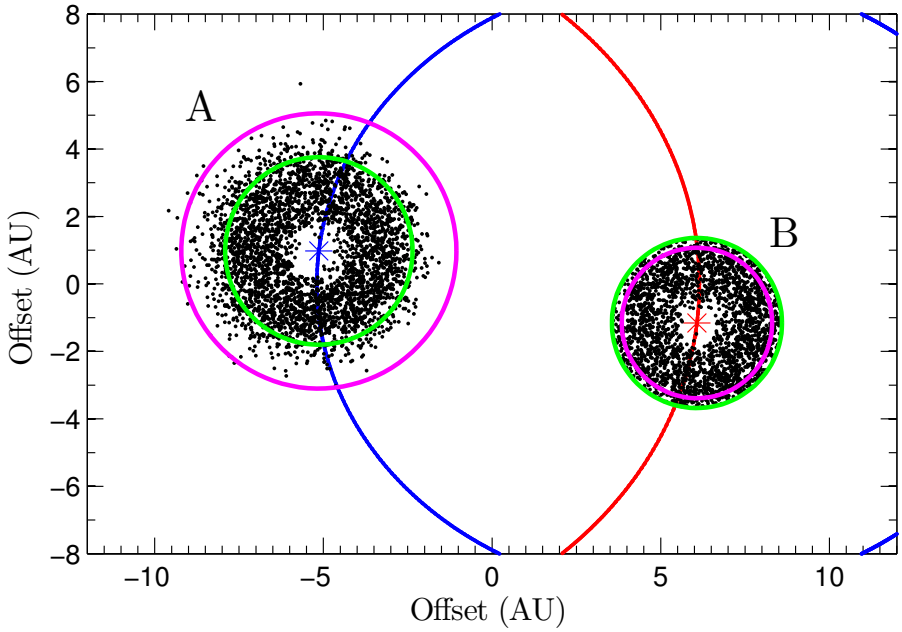

Figure 3.2: Circumstellar test particle discs for both stars, seen face on. The green circles correspond to the critical semi-major axis ($r_{\rm crit}$) and the purple circles correspond to the snow lines.

was, initially, disregarded due to its small mass which gives it a Hill radius of just 4×10^{-4} AU[4]. Our circum-α Cen B disc first reached only to 0.08 AU and the planet could be disregarded (as seen in the results of Paper I). The smaller, higher resolution disc, however, reaches all the way in to 0.03 AU while the semi-major axis of α Cen Bb is 0.04 AU.

In short: the combined, high-resolution discs were never used in Paper I, but are presented here in this chapter. The existence of α Cen Bb was never confirmed (Hatzes 2013; Demory et al. 2015; Rajpaul et al. 2016), and was disregarded in both Paper I and in the high resolution simulations. If the planet does exist, however, we can expect it to limit the amount of *hot* dust around 0.04 AU.

3.2 Observations

Through the DUNES Open Time Key Programme we obtained *Herschel*/PACS photometric images at $100\,\mu$m and $160\,\mu$m. From the Hi-GAL survey we received archive PACS data at $70\,\mu$m and $160\,\mu$m and SPIRE data at 250, 350, and $500\,\mu$m. With APEX-LABOCA we obtained data at $870\,\mu$m, and with SHeFI (Swedish Heterodyne Facility Instrument) APEX-1 we obtained complementing spectroscopic data during Directorâs Discretionary Time to map CO emission in the region around α Cen. More details on these observations are presented in Paper I.

[4]The Hill radius is a measurement of the sphere of influence that can be estimated from $\sim a(m/3M)^{1/3}$ for a planet of mass m at a distance a from a star of mass M.

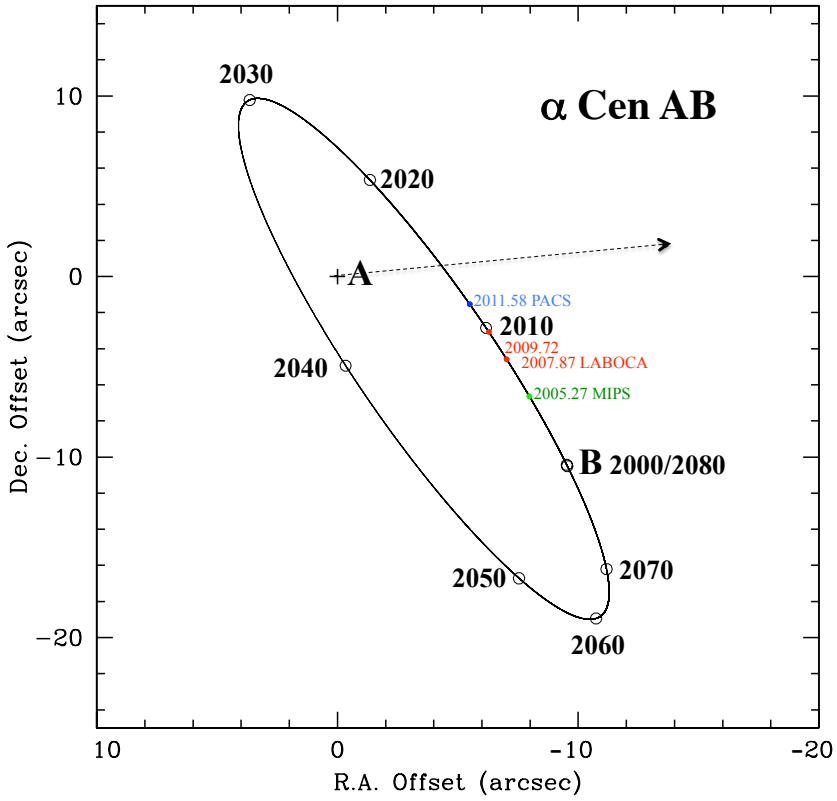

Figure 3.3: The orbit of α Cen B around A as seen from the Earth. The coloured dates signify when the observations were done and the relative position of α Cen B during these. The dashed arrow is the direction of the binary's proper motion, and the length of the arrow is the distance covered between the LABOCA (red, 2007-11-10 to 13) and PACS (blue, 2011-07-29) observations ($3\farcs7\,\mathrm{yr}^{-1}$). Green is the position of α Cen B and the date of the MIPS observation (2005-04-09). $1''$ corresponds to 0.74 AU at this distance.

The PACS data reduction were done with the Herschel Interactive Processing Environment version 8.0.1 (HIPE, Ott 2010). The LABOCA data were reduced with the Comprehensive Reduction Utility for SHARC-2 (CRUSH)[5], and the SHeFI data were reduced with the xs-package[6]. These all described in more detail in section 2.1 and 2.2 of Paper I.

In Figure 3.3 we see the orbit of α Cen B around α Cen A and their positions during the observations. The two stars are within $10''$ of each other on the sky and will stay so during the coming 30 years, as seen from Earth. This complicates future observations as they will not be resolved with anything less than the largest telescopes. Liseau et al. (2015, 2016) observed α Cen AB with ALMA, and these observations confirmed and refined the findings of the SEDs, and temperature minima of the two stars.

Because of the proximity of these stars they have a quite high proper motion of $3\farcs7\,\mathrm{yr}^{-1}$. The APEX-LABOCA and APEX-1 observations were made to be able to disentangle α Cen and everything associated with these stars from the confusing background.

[5] http://www.submm.caltech.edu/sharc/crush/
[6] http://www.chalmers.se/rss/oso-en/observations/data-reduction-software

The observed flux densities of both stars are summarised in Table 3.2.

3.3 The SEDs of α Centauri

The observed fluxes (Table 3.2) are plotted in Figures 3.4 and 3.5. The stellar models in those figures were computed by a 3D interpolation in a smoothed version of the PHOENIX/GAIA grid (Brott & Hauschildt 2005). It uses effective temperature and surface gravity from Torres et al. (2010) and metallicity from Thévenin et al. (2002), see Table 3.1.

The models span the wavelength region up to 45 μm, and at longer wavelengths a black body extrapolation is assumed. The accuracy of this is discussed in Section 3.3.1.

We see marginal excesses at $24\,\mu$m of 2.5 and $2.6\,\sigma$ for $\alpha\,\mathrm{Cen\,A}$ and B, respectively, in the SEDs. These are studied in detail in Section 3.3.2 and correspond well to Zodiacal cloud dust temperatures.

We also see a flux dip at, and around, $160\,\mu$m. The Sun exhibits a temperature minimum (temperature less than T_{eff}) in the Solar atmosphere, a few hundred kilometres above the photosphere, specifically at the lowest parts of the chromosphere. The temperature rises again above this altitude, through the chromosphere and the corona. The physics are, however, not well understood.

Liseau et al. (2013) discuss the observations of this phenomenon in $\alpha\,\mathrm{Cen\,A}$ in detail. In Paper I we are more concerned with the effects on dust observations. The temperature inversion is probably common in Solar-like stars, as is visible in the histogram of figure 6 of Eiroa et al. (2013). We revisit this histogram in Paper III and Chapter 5.

In cases other than $\alpha\,\mathrm{Cen}$, where the observed fluxes coincide well with a stellar black body extrapolation, we risk missing small amounts of cold Kuiper belt analogue dust if a stellar temperature minimum is not considered. In Section 3.3.1 we use $\alpha\,\mathrm{Cen\,A}$ as a template for other, more distant, stars to discuss how much dust we might miss.

Finally, we are not able to see any excess from possible circumbinary dust in the SED, assuming there is no edge-on disc. This is because the circumbinary dust is expected to exist at radii larger than 75 AU, well outside our beam size.

3.3.1 Temperature minimum

In the lowest parts of the Solar chromosphere the temperature drops below the effective temperature (around $\sim$ 500 km above the photosphere, see e.g. figure 4 of Avrett 2003). In the Sun this phenomenon is visible at wavelengths around $150\,\mu$m. Liseau et al. (2013) presented the first similar detection in the FIR spectrum of $\alpha\,\mathrm{Cen\,A}$. In Paper I we also see (tentatively) a similar effect in the SED of $\alpha\,\mathrm{Cen\,B}$, see Figure 3.5. In these papers we used a flux ratio between the two stars because they were not resolved with *Herschel*. This ratio was later confirmed with ALMA observations by Liseau et al. (2015).

The temperature minimum is expected to be common in other Solar-like stars, and to be visible in the 100-200 μm wavelength region because H and free-free interactions limit the visibility of the photosphere at these wavelengths. These *Herschel*/PACS observations (see Eiroa et al. 2013) are the first steps to help understanding the underlying physics.

In the case of $\alpha\,\mathrm{Cen\,A}$, we found a minimum temperature of $T_{\mathrm{min}} = 3920 \pm 375$ K, and for $\alpha\,\mathrm{Cen\,B}$, $T_{\mathrm{min}} = 3020 \pm 850$ K near $160\,\mu$m. It is common to express the temperature

Table 3.2: Photometry and FIR/flux densities of α Centauri

$\lambda_{\rm eff}$ (μm)	α Cen A S_ν (Jy)	α Cen B S_ν (Jy)	Photometry & reference
0.440	2215 ± 41	536 ± 10	B (1)
0.550	3640 ± 67	1050 ± 19	V (1)
0.790	4814 ± 89	1654 ± 30	I (1)
0.440	2356 ± 43	572 ± 10	B (2)
0.550	3606 ± 66	1059 ± 20	V (2)
0.640	4259 ± 78	1387 ± 26	R_c (2)
0.790	4784 ± 88	1666 ± 31	I_c (2)
1.215	4658 ± 86	1645 ± 30	J (3)
1.654	3744 ± 69	1649 ± 31	H (3)
2.179	2561 ± 47	1139 ± 21	K (3)
3.547	1194 ± 22	521 ± 10	L (3)
4.769	592 ± 11	258 ± 5	M (3)
24	30.84 ± 0.76	13.63 ± 0.33	MIPS (4)
70	3.35 ± 0.28	1.49 ± 0.28	PACS (5)
100	1.41 ± 0.05	0.67 ± 0.037	PACS (6)
160	0.56 ± 0.06	0.21 ± 0.06	*PACS (5), (6)
250	0.24 ± 0.05	0.11 ± 0.05	*SPIRE (5)
350	0.145 ± 0.028	0.064 ± 0.028	*SPIRE (5)
500	0.08 ± 0.03	0.04 ± 0.03	*SPIRE (5)
870	0.028 ± 0.007	0.012 ± 0.007	*LABOCA (7)

Notes. * Asterisks indicate values determined using $S_{\nu,\,\rm A}/S_{\nu,\,\rm B} = 2.25$ see Paper I.

References. (1) *Hipparcos*. (2) Bessell (1990). (3) Engels et al. (1981). (4) A. Mora [priv. comm.; FWHM(24 μm) = 6″], binary separation on 9 April 2005, 10.″4. (5) Hi-GAL: KPOT_smolinar_1, fields 314_0 & 316_0. *Herschel*-beams FWHM(70 μm) = 5.″6, (100 μm) = 6.″8, (160 μm) = 11.″3, (250 μm) = 17.″6, (350 μm) = 23.″9, (500 μm) = 35.″2, binary separation on 21 August 2010, 6.″3. (6) DUNES: KPOT_ceiroa_1, binary separation 29 July 2011, 5.″7. (7) 384.C-1025, 380.C-3044(A): FWHM(870 μm) = 19.″5, binary separation 20-13 November 2007, 8.″8 and 19 September 2009, 7.″0.

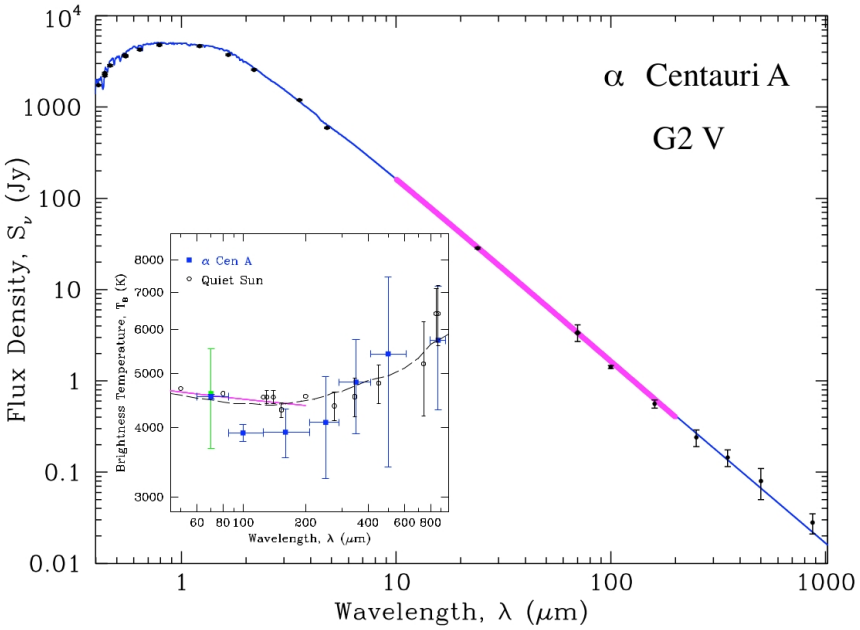

Figure 3.4: SED of α Cen A. The blue line is from a PHOENIX/GAIA model, the thick purple line is from an Uppsala model (up to 200 μm). The data points are presented in Table 3.2. The inset figure shows the FIR brightness temperature of α Cen A (blue squares) and of the Sun (black circles, Gu et al. 1997; Loukitcheva et al. 2004). The dashed black curve is from a semi-empirical chromosphere model for the Sun (Vernazza et al. 1981). See Paper I for details.

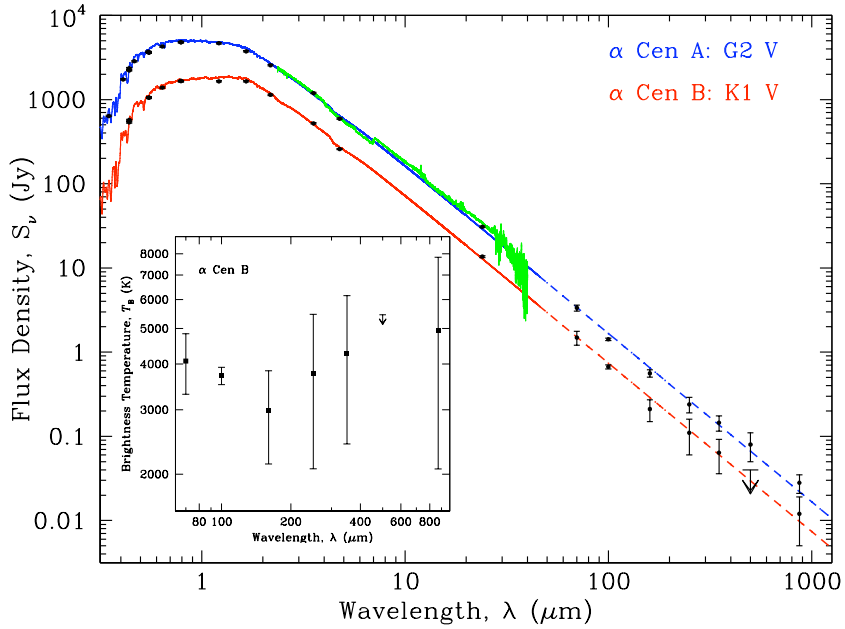

Figure 3.5: SEDs of α Cen A and B. As in Figure 3.4 for α Cen A, the red line is from a PHOENIX/GAIA model for α Cen B. The dashed lines correspond to where black body extrapolations are assumed. The data points are the observed flux densities listed in Table 3.2. Green is an ISO-SWS low resolution observation (see Decin et al. 2003). The inset figure shows the FIR brightness temperature of α Cen B.

minimum as the ratio $T_{\rm min}/T_{\rm eff}$. In our case we find the temperature ratios $T_{\rm min}/T_{\rm eff} = 0.67 \pm 0.06$ for $\alpha\,\mathrm{Cen\,A}$, and $T_{\rm min}/T_{\rm eff} = 0.58 \pm 0.17$ for $\alpha\,\mathrm{Cen\,B}$. Liseau et al. (2016) have since this expanded the observations with ALMA and estimated the $T_{\rm min}/T_{\rm eff} = 0.61$ for $\alpha\,\mathrm{Cen\,A}$.

These temperature ratios are slightly lower than what has been observed in the Sun by Ayres et al. (1976), who found a value of ~ 0.78, through optical observations of the Ca II K line. They also estimated the temperature minimum of $\alpha\,\mathrm{Cen}$ in this way and found temperature ratios of 0.78 or 0.79 for $\alpha\,\mathrm{Cen\,A}$, and 0.71 or 0.72 for $\alpha\,\mathrm{Cen\,B}$ (depending on stellar properties).

$\alpha\,\mathrm{Cen}$ is a good "laboratory" for other Solar-like stars. Because we do not expect to see any dust at these wavelengths for these stars, we can safely assume that we are observing the stars directly (more on circumbinary dust in Section 3.4). Thus we can use $\alpha\,\mathrm{Cen\,A}$ as a template for more distant stars that do have Kuiper belt dust. The question is how much dust emission is required to "fill" the temperature minimum so that the combined dust and stellar spectrum follows a stellar black body. This is the focus of Section 4.3 of Paper I.

In Figure 3.6 (bottom frame) we see the flux difference of the observation and extrapolation, $\Delta S = S_{\rm model} - S_{\rm min}$, of $\alpha\,\mathrm{Cen\,A}$ set at a distance of 10 pc ($S_{\rm min}$ is the observed flux density of the temperature minimum). To this curve we fitted modified black bodies, i.e. dust emission models written as in Equation 2.14 where $T_{\rm dust}$ is set to correspond with the peak wavelength of ΔS. This gives a dust temperature of 53 K.

It is common to express the strength of dust emission as a fractional luminosity, $f_d \equiv L_{\rm dust}/L_\star$. So with $\alpha\,\mathrm{Cen\,A}$ as a template, we can deduce that the difference in flux corresponds to emission with a fractional luminosity, $f_d = \left(2.2\,^{+1.2}_{-1.5}\right) \times 10^{-7}$. This is comparable with the Solar system Kuiper belt debris with a fractional luminosity of $\sim 10^{-7}$ (Vitense et al. 2012).

A fractional luminosity of 10^{-7} is, however, very small and difficult to detect. *Herschel* was estimated to have been able to observe Kuiper belts with a fractional luminosity of $\gtrsim 10^{-6}$ (Eiroa et al. 2013), and this is the largest space based telescope that has been in operation.

It is also possible to estimate, to the first order, a corresponding total dust mass from ΔS. Using the Hildebrand (1983) mass estimate (see Equation 2.13) we can exchange the dust flux density $S_{\rm dust}$ with $\Delta S = S_{\rm model} - S_{\rm min}$. The mass absorption coefficient, $\kappa_{\rm abs}$ depends on e.g. dust grain size distribution and grain size limits. By studying the literature we can assume a value of $\gtrsim 10\,\mathrm{cm^2\,g^{-1}}$ (with particles smaller than 1 mm and a size distribution $\propto a^{-3.5}$) for this estimate (see e.g. Miyake & Nakagawa 1993; Ossenkopf & Henning 1994; Draine 2006).

Using these assumptions, together with the observed flux density, the black body extrapolation flux density, and the corresponding dust temperature of 53 K, we find that the flux density difference can correspond to masses $\lesssim 10^{-3}\,M_{\rm Moon}$.

3.3.2 Circumstellar dust

From studies of the dynamics, we already know to what extent stable circumstellar orbits are possible around each of the two stars. It is difficult not to be reminded of the Solar system asteroid belt and Zodiacal dust cloud because of the stable region sizes, which are smaller

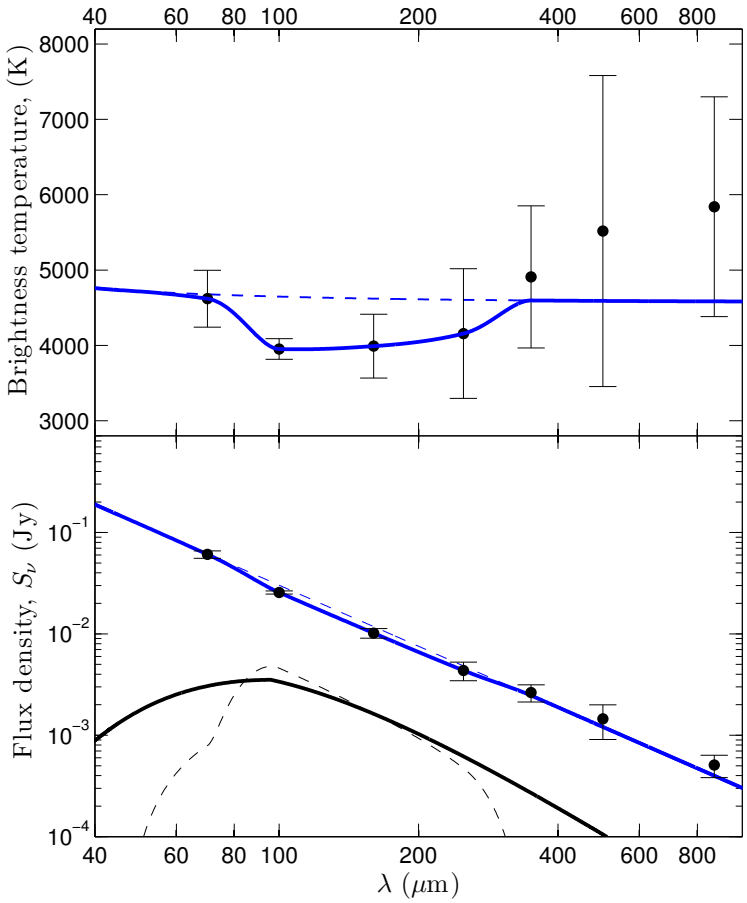

Figure 3.6: The part of the FIR spectrum of α Cen A (blue) which harbours the temperature minimum. The dashed blue line corresponds to the black body extrapolation of the stellar spectrum model. The top panel shows the flux density of α Cen A as expressed as brightness temperature. The bottom panel shows the flux density with α Cen A moved to a distance of 10 pc. The dashed black line corresponds to ΔS, the difference in model flux and observation, and the thick black line corresponds to a dust black body with the temperature 53 K.

than $3 - 4$ AU.

From the *Spitzer* observations presented in Paper I and Figure 3.5 we can deduce tentative excesses at $24\,\mu$m for both α Cen A and B with signal-to-noise ratio (SNR) of just 2.5 and 2.6. If interpreted as dust emission this corresponds to dust in the circumstellar regions. We aim here to model discs in these stable regions, and to set upper limits on fractional luminosities and mass estimates.

In order to correctly model these discs we choose to use the previously mentioned radiative transfer program RADMC-3D by Dullemond (2012) (see Section 2.3.2 for details).

In RADMC-3D, we used the stellar positions that correspond to the PACS $160\,\mu$m observations. We used the particle simulated discs, with the radial mass density distribution $\Sigma = \Sigma_0 \, (R/R_0)^{-\gamma}$, and homogeneously distributed particle sizes. We turned to the work by Miyake & Nakagawa (1993) for extinction coefficients. They computed the coefficients for spherical grains of different sizes, size ranges, and grain size distributions.

To summarise the grain properties used for the absorption; the blow-out radius of grains around α Cen A (mass density of $2.5\,\mathrm{g\,cm^{-3}}$) is 0.64 μm. We can approximate the minimum grain size to be six times as large (see Section 2.2), i.e. $\sim 4\,\mu$m. Furthermore, the observed emission is at a wavelength of $24\,\mu$m. We can thus infer that the minimum grain size, which also dominates the emission we are observing, is also $\sim 4\,\mu$m (this is usually assumed to be roughly $\lambda/2\pi$). We also know from Miyake & Nakagawa (1993) that larger grains exhibit less, or no, resonances. Largest grain size is, as usual, limited to 1 mm. Miyake & Nakagawa (1993) also computed absorption coefficients with size distributions of $q = 2$, 2.5, 3, 3.5, and 4.

As for the albedo; Miyake & Nakagawa (1993) assumed ice covered grains in their computations with the result of very high albedo in the optical. However, by computing the radii of the snow lines around both stars (see Section 2.2) we found that ice-covered grains seem unlikely in the stable regions (see more details in Paper I and Figure 3.2 where the ice lines are plotted). From Inoue et al. (2008) we learn that the albedo is roughly half of ice-free silicates for $\sim 10\,\mu$m grains, which gives us more realistic albedo models (we assumed isotropic scattering).

Summary of the resulting SED models

The results presented here are from using more high resolution discs than those that were used in Paper I. These discs stretch from 0.03 AU (the grain evaporation temperature is ~ 1500 K and corresponds to roughly 0.03 AU from the stars) out to the critical semi-major axis, and have radial surface density distributions formulated as $\Sigma(R) = \Sigma_0 \, (R/R_0)^{-\gamma}$, with γ varying from 0 to a maximum of 10. $\gamma > 2$ represents small rings close to the star.

Figures 3.7 and 3.8 show dust SEDs for both α Cen A and B as computed with RADMC-3D. The discs here have $\gamma = 0$, and the different frames are for different grain size distributions, q from Equation 2.4. To set upper limits, the dust emission was constrained by the observations at 5, 24, and $70\,\mu$m, where the observed fluxes at $70\,\mu$m correspond well with the stellar models. One SED of each plot matches the $24\,\mu$m flux. However, none of these fits within the uncertainties at $70\,\mu$m (this may be difficult to see in Figures 3.7 and 3.8 due to the very small error bars). This tells us that the dust distribution is either more radially constrained or that the emission is weaker.

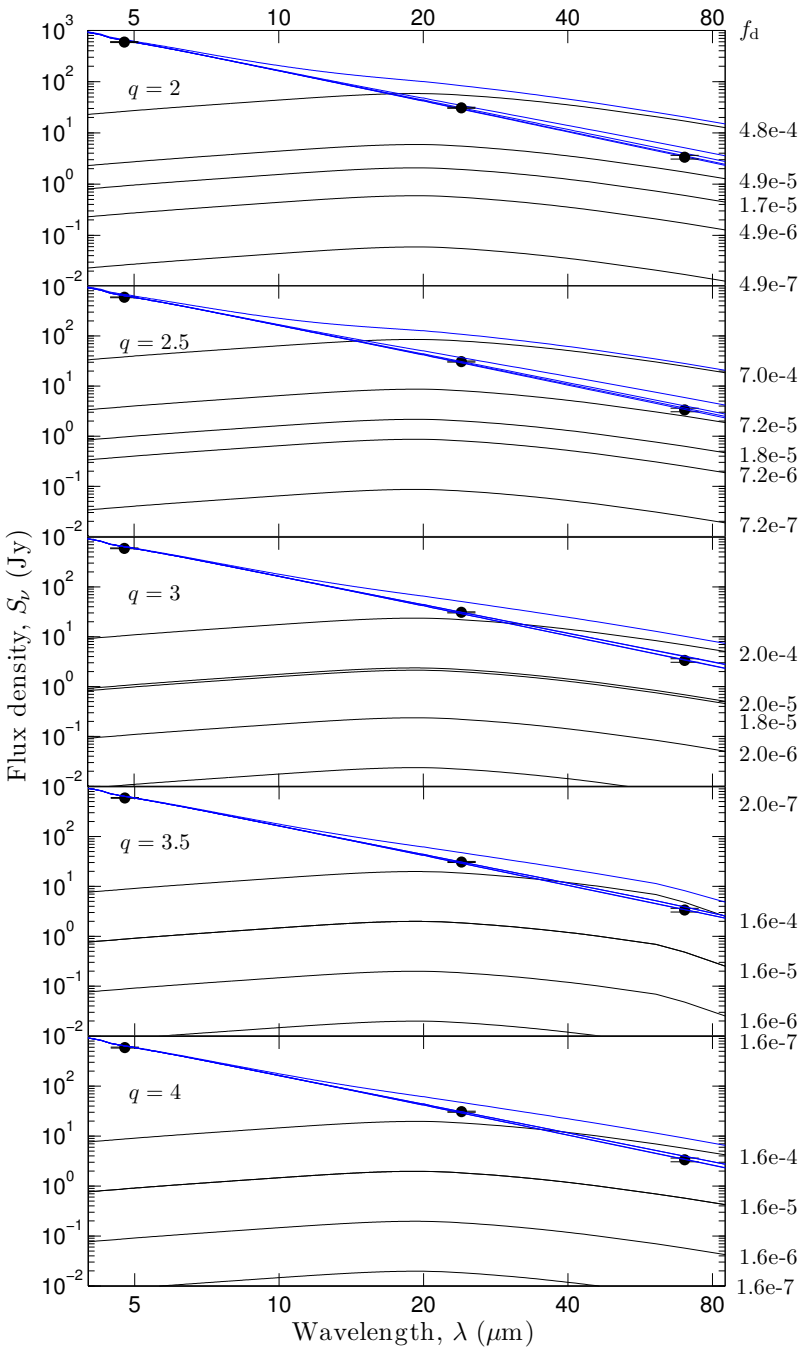

Figure 3.7: Dust emission models for $\alpha\,\mathrm{Cen\,A}$ with circumstellar dust discs with various grain size distributions (varying q) and flat radial disc density distribution ($\gamma = 0$). Black lines are dust emission (corresponding fractional luminosities to the right) and blue lines are combined dust and stellar emission. The fractional luminosities on the right axis are positioned by their corresponding black dust emission curve. The photometry error bars are indicated with horisontal lines and are smaller than the data point markers.

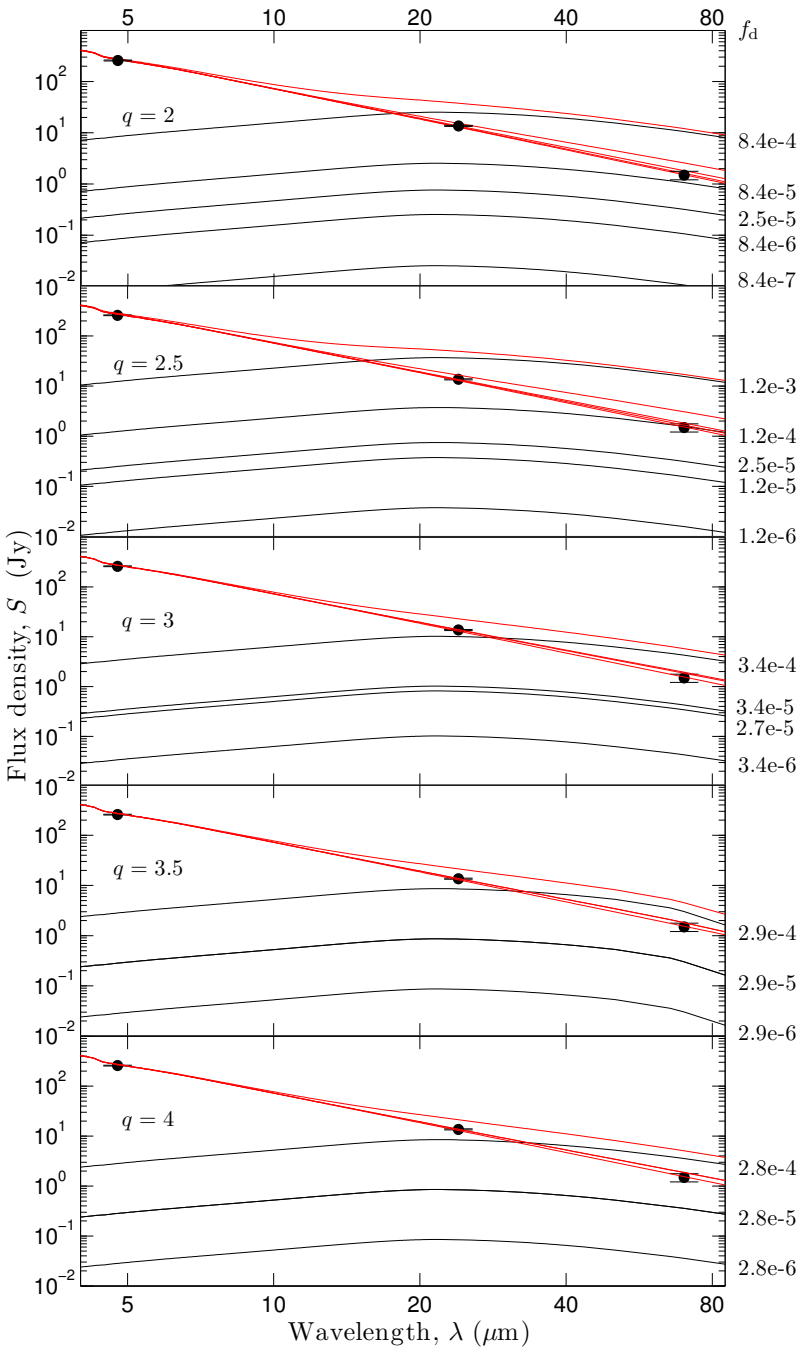

Figure 3.8: Dust emission models for α Cen B with circumstellar dust discs with various grain size distributions (varying q) and flat radial disc density distribution ($\gamma = 0$). Black lines are dust emission (corresponding fractional luminosities to the right) and red lines are combined dust and stellar emission. The fractional luminosities on the right axis are positioned by their corresponding black dust emission curve. The photometry error bars are indicated with horisontal lines and are smaller than the data point markers.

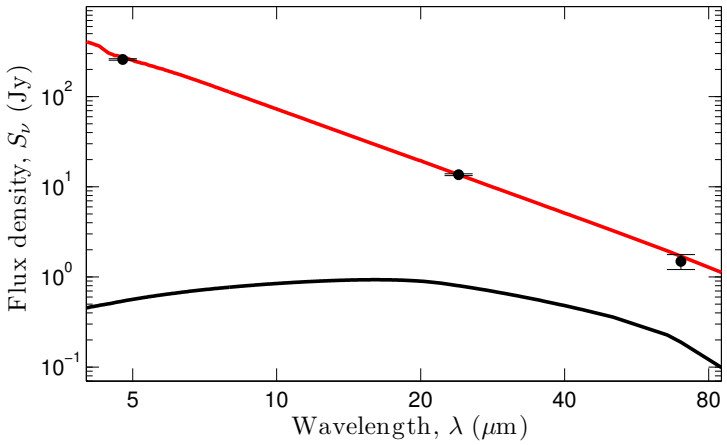

Figure 3.9: α Cen B SED with dust emission (black curve) from a dust disc with $\gamma = 1.0$, $q = 3.5$. The red curve is the combined stellar and dust spectrum.

The α Cen B observations have larger errors in general than the α Cen A observations, which allow a wider range of emission models. The observations allow discs with $\gamma \gtrsim 1.0$. In Figure 3.9 one model SED is shown for α Cen B with $\gamma = 1.0$ and $q = 3.5$. For α Cen A only extremely constrained rings close to the star ($\gamma > 6.0$ for example) would give model fluxes that are inside the 70 μm error.

However, for α Cen A, acceptable models tend to have fractional luminosities of roughly $f_\mathrm{d} < 2 \times 10^{-5}$. For α Cen B, similar models have fractional luminosities of $f_\mathrm{d} < 3 \times 10^{-5}$. More radially constrained discs, i.e. with $\gamma \sim 1$ around α Cen B, are warmer and have fractional luminosities of $f_\mathrm{d} < 4 \times 10^{-5}$. These results are principally the same as those already published in Paper I.

The models described here correspond to total dust masses (grain sizes between 4 μm and 1 mm) of roughly 10^{-5} to $5 \times 10^{-6}\, M_\mathrm{Moon}$ when assuming size distributions with $q = 3.5$. This can be compared with the estimated total mass of the Zodiacal cloud, i.e. 0.3 to $1.5 \times 10^{-7}\, M_\mathrm{Moon}$ (Fixsen & Dwek 2002). In general, the models with $q = 3.5$ or $q = 4$ fit the data better than corresponding discs with smaller q.

3.4 Circumbinary dust

Circumbinary orbits are allowed at radii $\gtrsim 75$ AU from the stellar barycenter. At a distance of 1.348 pc, this corresponds to an angular size of $\sim 56''$, i.e. clearly resolvable at all PACS-wavelengths. This section summarises the discussion in Paper I concerning circumbinary dust.

What such a ring should look like depends on its inclination and outer radius. The Kuiper belt in the Solar system, for example, is estimated to have an outer radius of some 60 AU (with scattered objects further out, Vitense et al. 2010). There are examples of much larger debris discs such as the Fomalhaut ring with an outer radius of some 200 AU (Acke et al. 2012). The outer radius is unconstrained by the dynamics, so the outer radii of the simulated

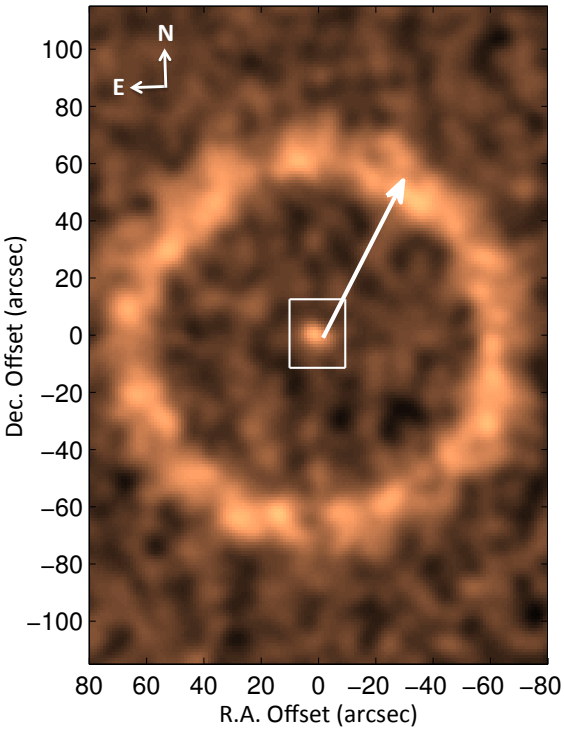

Figure 3.10: Synthetic observations of a face-on circumbinary ring around α Cen. The arrow represents a distance of 80 AU. The image was made with RADMC-3D with a disc with radius $\lesssim 100$ AU. Each pixel side is $1\farcs04$. The noise is Gaussian-distributed, and the image was smoothed with a Gaussian filter to mimic the beam size of the PACS-photometry (see Figure 3.11 below).

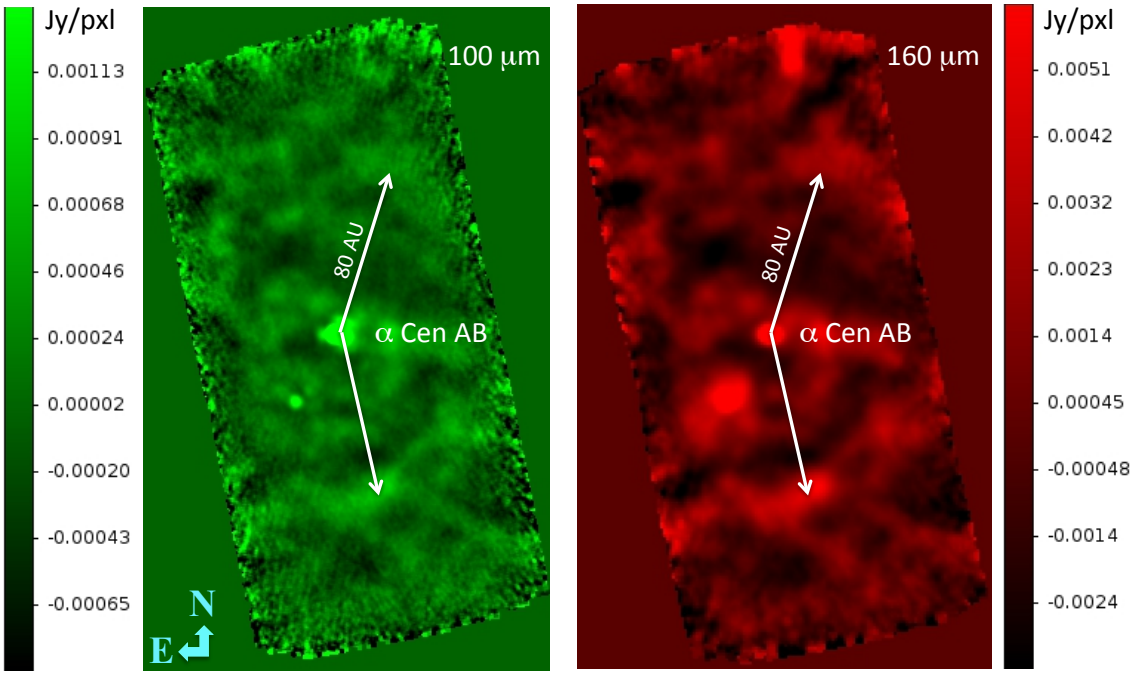

Figure 3.11: Left frame shows *Herschel*/PACS photometry at 100 μm with α Cen in the centre and the arrows represent a distance of 80 AU from the stars, i.e. where circumbinary dust could be expected. The right frame shows the same as the left frame, but at 160 μm.

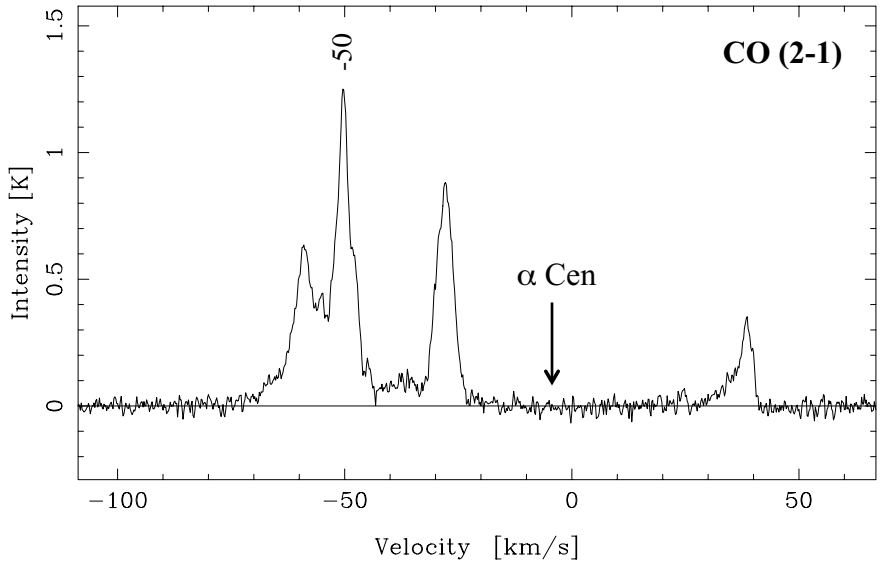

Figure 3.12: Average of all CO $(2-1)$ spectra toward $\alpha\,\mathrm{Cen}$ plotted against v_{LSR}. The LSR velocity associated with $\alpha\,\mathrm{Cen}$ is indicated.

discs we show here are purely due to initial conditions.

Figure 3.1 shows the results of particle simulations of a circumbinary ring with zero inclination to the binary orbital plane, and initial outer radius of $100\,\mathrm{AU}$. The inclination can, however, also be unconstrained for circumbinary rings (Wiegert & Holman 1997; Moutou et al. 2011), whereas circumstellar discs are limited to inclinations $< 60°$. Observations of the binary 99 Herculis, for example, indicate that these stars have a circumpolar and circumbinary disc (Kennedy et al. 2012).

Figure 3.10 is a synthetic observation of a face-on ring, as seen from the Earth, around $\alpha\,\mathrm{Cen}$ that represents what a circumbinary ring could look like at $160\,\mu\mathrm{m}$. In the *Herschel*/PACS photometry shown in Figure 3.11 we do indeed see persistent, curved/circular like structures at the correct angular distances from the stars.

In order to investigate if these structures are associated with $\alpha\,\mathrm{Cen}$ or the galactic background, we mapped CO $(2-1)$ emission from the surrounding background with APEX, see Figure 3.12. This gives the local-standard-of-rest (LSR) velocities of the background seen in the PACS images. We see here that both proper motion and spectral line data rule out that we have observed circumbinary features since all detections have LSR velocities of -30, -50, -60, and $40\,\mathrm{km\,s^{-1}}$. These agree with observations of CO $(1-0)$ in the Milky Way (Dame et al. 2001). In conclusion; if there is any circumbinary dust associated with $\alpha\,\mathrm{Cen}$, it remains undetected by us.

Chapter 4

Introduction to paper II: The triple star 94 Ceti

94 Ceti is an intriguing system. It has interesting observational history, it was believed to be a binary star since Admiral Smyth (Smyth 1844; Raghavan et al. 2006) was able to observe the two components in 1836, at a distance of 220 AU. However, Röll et al. (2011, 2012) recently found that its binary companion is in fact two M dwarfs on a tight (~ 1 AU) one year-orbit, making it a triple system.

Considering that a dust excess was observed already by Trilling et al. (2008) with *Spitzer*, and later expanded by Eiroa et al. (2013) with *Herschel*. This makes one of the few known triple systems harbouring both at least one planet (Queloz et al. 2004; Mayor et al. 2004) and a dust disc.

In Paper II we bring up questions on how multiple star systems are important when considering e.g. planet formation processes and the continued evolution of planetary systems. Interest in this system was initially triggered by Eiroa et al. (2013). They noted that the dust emission corresponds to dust that recides in a dynamically unstable region of the system. It was also noted that the main source in the *Herschel* images appears extended. In Paper II we note that weak extensions are visible to the east, west, and south from the main source. Note that this was before the triple star status was known for 94 Cet, which is why Eiroa et al. (2013) list this as a binary.

94 Cet's status as a triple system with a planet and gas disc of unknown configuration, and its extended emission of unknown origin prompted us to explored this system.

We ran N-body simulations of the possible disc configurations as well as used RADMC-3D to simulate the emission from such discs. The excess at the source would appear to fit with circumsecondary dust on a circumbinary orbit around the two companion stars. Also, the eastern and western extensions appear to fit both spatially and to the SED of circumtertiary dust. However, the circumtertiary dust SED is unconstrained at long wavelengths and there are spatial gaps in the extended emission. We were not able to observe a spectral map of e.g. the CO $(2-1)$ in the field as we did for $\alpha\,\mathrm{Cen}$ to compare the v_{LSR} of the background with the presumed circumbinary emission. On the other hand, $\alpha\,\mathrm{Cen}$ is in the direction of the galactic plane which provides plenty of background cirrus, while most other DUNES sources are chosen so that they would avoid confusing backgrounds. So the question is: how useful

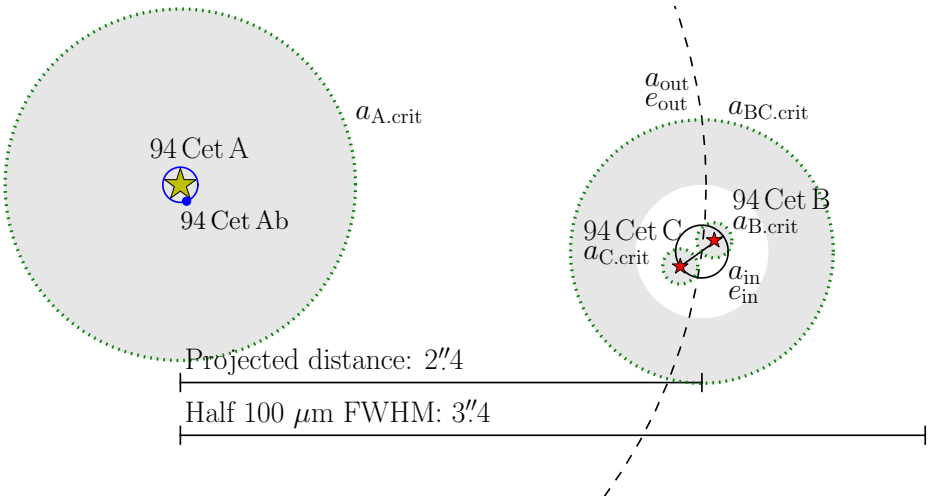

Figure 4.1: Schematic overview of the known components of the 94 Cet system (not to scale). The dashed black curve is the orbit of the binary pair, 94 Cet BC, around 94 Cet A, and is denoted as the *outer orbit*. The solid black circle is the orbit of 94 Cet C around 94 Cet B, and is denoted as the *inner orbit*. The blue circle with a dot indicates the orbit of the planet 94 Cet Ab. The regions where we can expect stable orbits are shown by the shaded regions and the green dotted lines are the critical semi-major axes. These are denoted as $a_{\mathrm{A.crit}}$, $a_{\mathrm{B.crit}}$, $a_{\mathrm{C.crit}}$, and $a_{\mathrm{BC.crit}}$ ($a_{\mathrm{ABC.crit}}$ is outside this figure). The projected distance refers to the angular distance between the stars during the observations and this is compared to half of the *Herschel* beam FWHM at 100 μm. All parameters are listed in Table 4.1

would similar CO $(2-1)$ observations around 94 Cet be?

Gas content may be low in older stars, while it is not uncommon in young (< 50 Myr) A-type stars (Greaves et al. 2016). The gas may come from volatile cometary breakups, or from a very prolonged protoplanetary disc phase. The disc of β Pic, for example, contains asymmetrically distributed gas that resides in clumps throughout the disc. The total mass of CO at β Pic is $2.3 \times 10^{-3}\, M_{\mathrm{Moon}}$ (Dent et al. 2014). The lack of gas detections from older stars may be due to observational bias, however, bias-effects may be small. The amount of gas contents in debris discs are still widely discussed.

Our findings on this intriguing system were published in Paper II, and are summarised in this chapter.

4.1 System properties

94 Cet is a hierarchical triple system, where it is common to denote the larger orbit as the *outer orbit*, while the smaller orbit of the binary pair-component is the *inner orbit*. See Figure 4.1 for a schematic overview of this system.

The companion binary component, 94 Cet B and C, orbit the primary 94 Cet A on a 2000 year period, with a semi-major axis of 220 AU. This time scale has made the observations of the outer orbit difficult, which is why the more recent orbital refinement of Roberts et al. (2011) differs significantly from the parameters found by Hale (1994).

Table 4.1: 94 Cet orbital parameters.

	Outer orbit[a]	Inner orbit[b]	Planetary orbit[c]
Semi-major axis, a (AU)	220 ± 5	0.99 ± 0.02	1.42 ± 0.01
Period (yr)	2029 ± 41	1.04 ± 0.01	1.47 ± 0.01
Eccentricity, e	0.26 ± 0.01	0.36 ± 0.01	0.30 ± 0.04
Inclination to LOS, i (°)	104 ± 2	108.5 ± 0.7	...
Arg. of periapsis, ω (°)	342 ± 7	334.9 ± 2.3	...
Long. of asc. node, Ω (°)	97 ± 2	190.9 ± 1.0	...
Critical semi-major axis[d]			
$a_{\rm A.crit}$	47.1 (14%) AU	1.″8 (15%)	
$a_{\rm B.crit}$	0.2 (22%) AU	0.″009 (22%)	
$a_{\rm C.crit}$	0.1 (39%) AU	0.″004 (44%)	
$a_{\rm BC.crit}$	36.4 (22%) AU	1.″6 (23%)	
$a_{\rm ABC.crit}$	660 (2%) AU	29″ (3%)	

References. [a] Roberts et al. (2011). [b] Röll et al. (2011, 2012). [c] Mayor et al. (2004). [d] Holman & Wiegert (1999).

Furthermore, this system hosts the circumprimary gas giant planet, 94 Cet Ab, that was found in the CORALIE survey (Queloz et al. 2004; Mayor et al. 2004). It has a mass of $m_{\rm b} \sin i = 1.7\, M_{\rm Jup}$, and a period of 536 days which corresponds to a semi-major axis of 1.4 AU.

The orbital parameters of this system are listed in Table 4.1. The critical semi-major axis refers to radii inside which stable orbits are expected (outside in the case of $a_{\rm ABC.crit}$, which refers to circumtertiary orbits). These were calculated with the same semi-analytical expression as used for α Cen, presented in Equation 3.1. Although, this expression was formulated for binaries, we were able to use it by coupling the different components (see section 5 of Paper II for details). As a result, we have indications of the positions and sizes of the regions where we can expect dust.

4.2 Dust disc models

We used the symplectic integrator Hierarchical Jacobi Symplectic (HJS) of Beust (2003)[1] to perform N-body simulations for the discs in this system. This code is suitable for a hierarchical system such as this. Interestingly, the way we handle the semi-analytical equation for binaries from Holman & Wiegert (1999), applied onto a triple system is quite accurate.

[1] `http://ipag.osug.fr/~beusth/hjs.html`

Table 4.2: Parameters for RADMC-3D simulations.

Parameter	Value
Grain size range, a (μm)	8 to 10^{3*}
Blow out radius, $a_{\rm blow-out}$ (μm)	1.3^{a}
Grain density, ρ (g cm^{-3})	2.5
Size distr., $n(a) \propto a^{-q}$ (cm^{-3})	$q = 2$ to 4^{b}
Surface density, $\Sigma(r) \propto r^{-\gamma}$ (g cm^{-2})	$\gamma = -2$ to 2
Vertical distribution, $h(r)$ (AU)	$0.1 \times r^{c}$
Absorption coeff., $\kappa_{\rm abs}(a, q, \rho)$ (cm^2 g^{-1})	$\kappa_{\rm ext}\,(1-\eta)^{d,e}$
Scatter coeff., $\kappa_{\rm scat}(a, q, \rho)$ (cm^2 g^{-1})	$\kappa_{\rm ext}\eta^{d,e}$
Inner disc radius, $r_{\rm in}$ (AU)	$r(T_{\rm vap})^{\dagger}$
Outer disc radius, $r_{\rm out}$ (AU)	$a_{\rm crit}{}^{\ddagger}$

Notes. * $a_{\rm min} \approx 6 \times a_{\rm blow-out}$ (Wyatt et al. 2011; Löhne et al. 2012; Thébault 2016). †: Inner disc radius is limited by vaporisation temperature, $T_{\rm vap} = 1800$ to 1300 K (Pollack et al. 1994; Moro-Martín 2013). ‡: See Equation 3.1 and dynamical simulations.

References. (a) Plavchan et al. (2009). (b) Dohnanyi (1969). (c) Artymowicz (1997). (d) Miyake & Nakagawa (1993). (e) Inoue et al. (2008).

Each simulation was run for 20 Myr and for three different configurations; one circumstellar (a disc inside $a_{\rm A.crit}$), one for circumsecondary and binary dust (a disc inside $a_{\rm BC.crit}$), and finally one for the circumtertiary disc (outside $a_{\rm ABC.crit}$). However, we also considered circumstellar dust around the two companion stars, i.e. inside $a_{\rm B.crit}$ and $a_{\rm C.crit}$, that was based on the simpler code written for α Cen (see Section 3.1).

The methodology here is similar to the one we used for α Cen. We applied RADMC-3D by using the results from the particle simulations, with radial density distributions, and the dust properties described in Section 6.1.1 of Paper II, and in Table 4.2 of this thesis.

We considered the system in an unbiased fashion by modelling dust emission from all four disc configurations (we consider circumstellar dust around both companion stars as one combined configuration). However, we suspected early that a circumsecondary disc was the most probable outcome. This was primarily based on two reasons: a) the disc black body radius (assuming circumprimary dust) from Eiroa et al. (2013) places it far out in the unstable region, closer to the outer orbit. b) There is a marginal pointing offset of 2.1 to 2.6 times the average pointing offset of the telescope between the tabulated position of 94 Cet A (compensated for proper motion) and the observed source position. This offset is in the direction of where the companion binary is, which results in a significantly smaller offset to these stars.

We also compared the observed SED with that of a FIR, high-redshift galaxy (using models from Chary & Elbaz 2001, to be revisited in Chapter 6). However, in the case of 94 Cet this was inconclusive, as the galactic SED's FIR dust emission was indistinguishable from circumstellar dust emission. The probability of chance alignment with background galaxies, on the other hand, has been estimated to be lower than 3% .

We find best fits with circumbinary dust around the two companion stars in a disc between

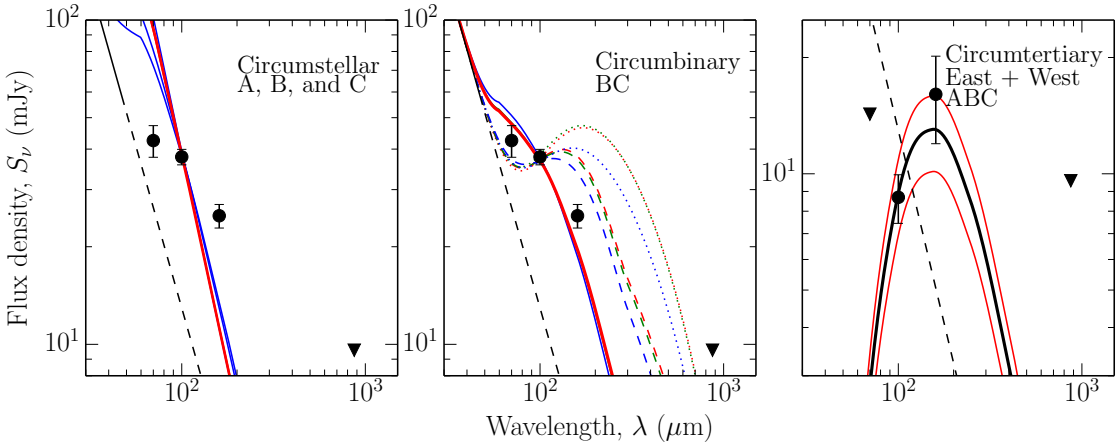

Figure 4.2: 94 Cet excess models. The thin black line is the model stellar photosphere and the dashed line indicates where a Rayleigh-Jeans tail is assumed. Black dots are photometric data points and the black triangle is a $3\,\sigma$ upper limit. The left panel shows circumstellar discs, both circumprimary (blue) and circumsecondary (red). The middle panel shows circumbinary discs around the secondary pair of stars where the best fit is shown with a thick red line. Models with $\gamma = -2$ are red, $\gamma = 0$ are green, and $\gamma = 2$ are blue, and $q = 3.5$ is shown with solid lines, $q = 3.0$ with dashed lines, and $q = 2.5$ with dotted lines. The right panel shows the best fit circumtertiary dust (black curve) with error estimates as thin red curves, and the data points are the combined flux density of the eastern and western extensions.

~ 3 to ~ 40 AU, with the temperatures 30.3 ± 7.4 K. This model has a grain size distribution, $q = 3.5$, however, the χ^2 measurements we used to test model accuracy implies that a q between 3 and 3.5 would formally fit better. The radial surface density distribution is $\propto r^2$, and the fractional luminosity is $f_\mathrm{d} = 4.6 \pm 0.4 \times 10^{-6}$. These model parameters and the grain size range imply a total dust mass of $6.0 \pm 0.5 \times 10^{-2}\,M_\mathrm{Moon}$.

Circumtertiary dust is possible. If the eastern and western extensions in the PACS images are part of this, they would correspond to a ring with the fractional luminosity $f_\mathrm{d} \approx 1.4 \pm 0.3 \times 10^{-6}$ and temperature of < 30 K. We assume that $q = 3.5$, and that the surface density distribution $\propto r^{-1}$ between an inner edge at 600 – 650 AU to ~ 750 AU. These models, and some of the poor fits, are plotted together in Figure 4.2.

4.3 The observed fields

One of the earlier reasons for studying this source was, apart from the the dynamically unstable dust disc size, the background. The focus of Paper II is the dust emission, while the background is discussed in Appendix A of the paper.

Eiroa et al. (2013) observed 94 Cet with *Herschel*/PACS, and we added additional submm observations from APEX-LABOCA at 870 μm. The PACS observations were reduced with HIPE v.13.0.0, and the LABOCA observations were reduced with CRUSH. Observations and data reduction are described in detail in sections 3.1 and 3.2 of PaperII.

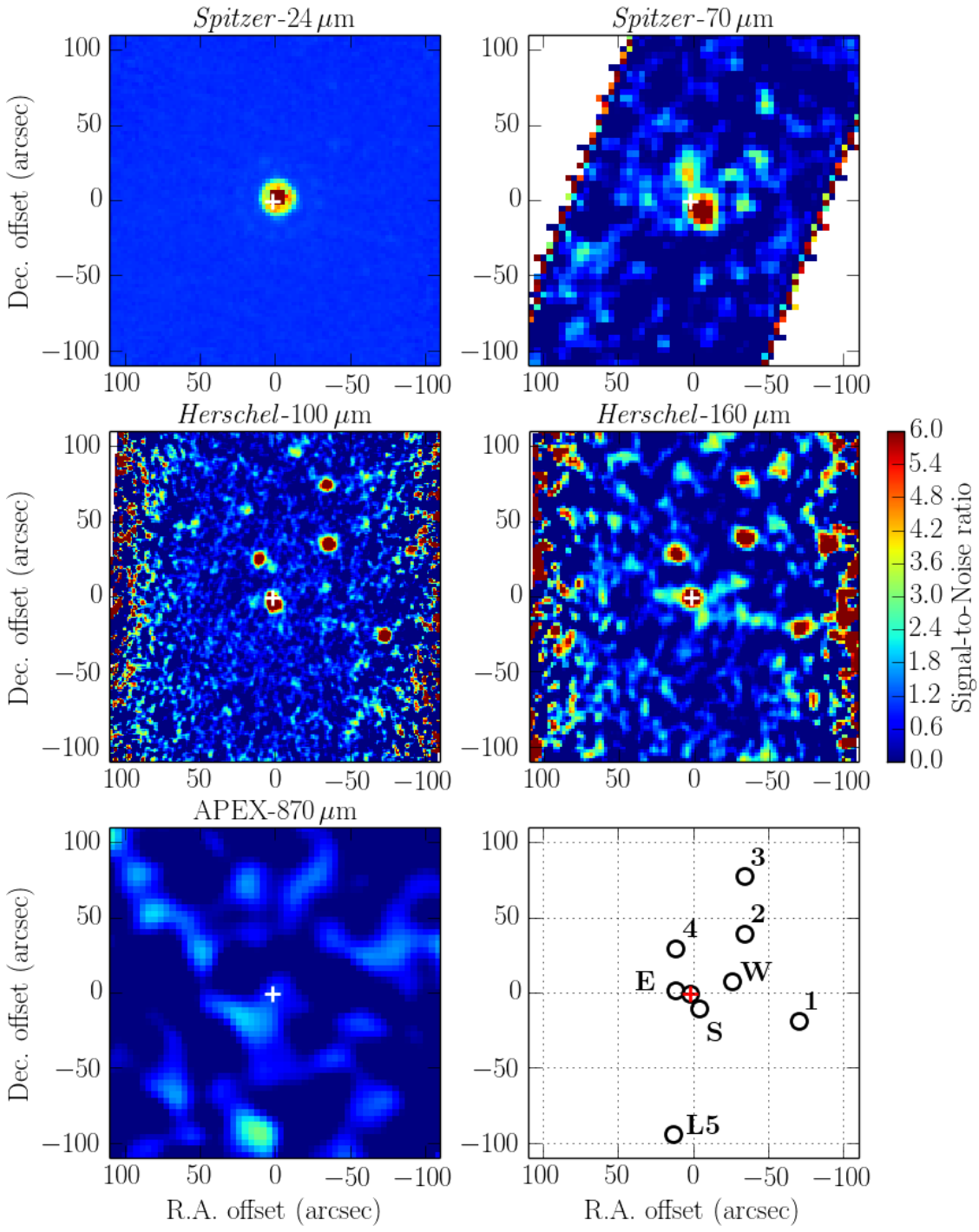

Figure 4.3: SNR maps from Paper II of the *Spitzer*/MIPS 24 μm and 70 μm images (as extracted from the *Spitzer* archive, Trilling et al. 2008), the *Herschel*/PACS 100 μm and 160 μm images (observed by Eiroa et al. 2013), and our APEX-LABOCA 870 μm observation. The lower right image identifies background sources found in the field. The stellar position is indicated with a cross, and E, S, and W denote the eastern, southern, and western extensions.

Table 4.3: LABOCA-field background sources, coordinates, and flux densities.

Source	R.A. (J2000) h m s	Dec. (J2000) ° ′ ″	S_ν (mJy)
94 Cet-L1	3 12 39.08	-1 17 06.8	18.70 ± 5.93
94 Cet-L2	3 12 42.30	-1 15 32.2	14.55 ± 3.73
94 Cet-L3	3 12 46.02	-1 16 16.3	16.13 ± 4.81
94 Cet-L4	3 12 46.56	-1 07 00.0	16.56 ± 5.49
94 Cet-L5	3 12 47.37	-1 13 20.3	14.62 ± 2.73
94 Cet-L6	3 12 51.89	-1 09 36.0	17.97 ± 4.11
94 Cet-L7	3 12 58.34	-1 13 02.5	16.05 ± 3.90

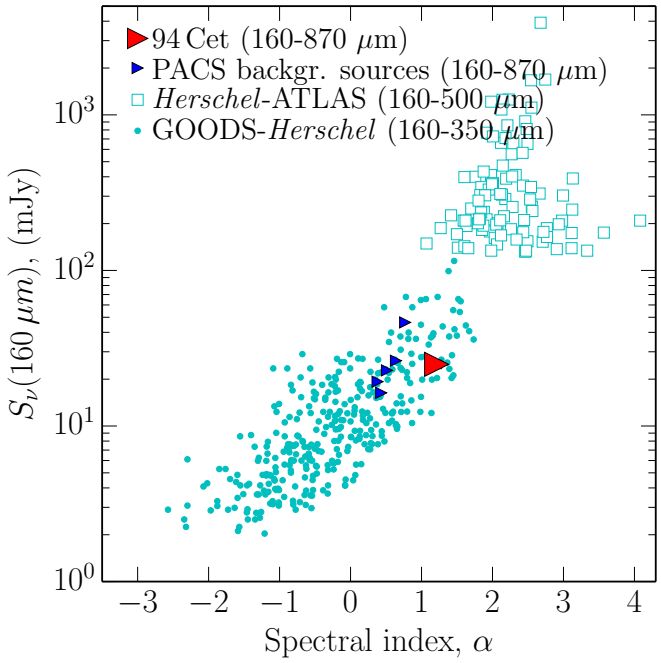

Figure 4.4: Spectral index map of the PACS background sources in the 94 Cet field and FIR galaxies. Cyan dots are spectral indices of FIR galaxies from the north field of the GOODS-*Herschel* (Elbaz et al. 2011, 2013) with $\lambda = 160$ to 350 and 500 μm. Cyan squares are spectral indices of FIR galaxies from *Herschel*-ATLAS (Rigby et al. 2011) with $\lambda = 160$ to 500 μm. Red triangle indicate 94 Cet upper limit spectral index (using $1\,\sigma$ upper limit at 870 μm), and the blue triangles are background sources upper limits with $\lambda = 160$ to 870 μm ($3\,\sigma$ upper limit at 870 μm).

In the immediate neighbourhood of the main source of 94 Cet are the previously mentioned eastern, western, and southern extensions located. We also mapped out five additional point sources in the PACS field, and seven other sources in the LABOCA field (the LABOCA sources' flux densities are listed in Table 4.3), all with SNR>3. SNR maps of the fields observed at five different wavelengths are plotted in Figure 4.3, where the last panel is a map of sources closer than $100''$ from the main source.

One of the earlier ideas we explored was the possibility to distinguish between circumstellar dust emission and high-redshift galaxies in the background sources. The probability of chance alignment is widely discussed in the circumstellar dust literature (e.g. Eiroa et al. 2013; Krivov et al. 2013; Montesinos et al. 2016 and Paper II), and a general consensus is that the high-redshift galaxy contamination is less than 5% , depending on dust temperatures and flux densities.

As mentioned in Section 4.2, we used model SEDs of high-redshift galaxies from Chary & Elbaz (2001) to compare with the stellar SEDs. We also compared the spectral indices of high-redshift galaxies, with the PACS sources in the 94 Cet-field, and with 94 Cet itself, as shown in Figure 4.4. In reality, this is merely a comparison between circumstellar dust and galactic dust emission, similar to the SED model comparison. Note that the spectral indices from the 94 Cet-field are upper limits since they are not detected at 870 μm. 94 Cet itself is plotted as a 1σ upper limit to be able to distinguish it better.

We were able to identify two of the PACS background sources. At the positions of the PACS sources 94 Cet-2 and 5, we found the catalogued sources SSTSL2 J031244.01-011111.8 and SSTSL2 J031248.04-010850.9, respectively, in the *Spitzer* Heritage Archive[2]. However, they were not found in any other large catalogues nor in the Palomar Sky Survey (where 94 Cet exhibits a very large Point Spread Function, PSF, in the infrared). At MIPS 24 μm, at these coordinates, there exist tentative sources.

Even though these studies on the background sources proved inconclusive, we list the background sources in the paper's appendix as they might be of interest in fields of research that includes high-redshift galaxies.

[2]Available via the NASA/IPAC Infrared Science Archive, Caltech/JPL. `https://irsa.ipac.caltech.edu/`

Chapter 5

Introduction to paper III: New reduction of the DUNES archive

DUst around NEarby Stars (DUNES, Eiroa et al. 2013), and Disc Emission via a Bias-free Reconnaissance in the Infrared/Submillimetre (DEBRIS, Matthews et al. 2010) are two *Herschel* open time key programmes. Both projects observed and characterised debris discs of nearby stars by observing FIR excesses above the stellar photospheres. DUNES prioritised Solar-like stars (F, G, and K), and DEBRIS had a wider volume-limited sample of A to M type stars.

DUNES observed in total 133 stars within 25 pc and the results were published by Eiroa et al. (2013), E13. An additional 55 F, G, and K type stars were observed by DEBRIS and shared with DUNES. The results on these were published by Montesinos et al. (2016), M16.

The DUNES and DUNES/DEBRIS-shared sources, hereafter the E13 sources and M16 sources, were chosen from the *Hipparcos* catalogue and are those where the photosphere would be detectable with an SNR greater than 5 with *Herschel*/PACS (Poglitsch et al. 2010) at 100 μm.

The E13 PACS-fields were originally reduced with HIPE version 7.2 and PACS calibration version 32, and the M16 fields were similarily reduced with HIPE version 10 and PACS calibration version 45. Reduction scheme details are described by Eiroa et al. (2013).

Our aim here was to combine these two data sets into one set of data, coherently reduced with the same calibration strategy, using the same version of HIPE and calibration, and to coherently measure the flux densities of all 188 sources. This would guarantee to result in a homogeneous statistical sample of nearly 200 stars observed at 100 μm and 160 μm, including all F and G stars within 20 pc (Eiroa et al. 2013; Montesinos et al. 2016).

As the M16 data were reduced with a more recent software, it can be used as a control group. In our diagnostics we find that the M16 data correspond well with the results we have on the same sources, while we systematically estimate about 1σ higher flux densities for the E13 sources.

We used several diagnostics, i.e. comparing the old and new flux data with the line of regression of the $F_{\rm old} \propto F_{\rm new}$ relation, an SNR comparison between the old and new data sets, a Gaussian flux comparison ($\chi_{\rm F}$), and the amount of excess flux ($\chi_{\rm d}$).

With these diagnostics we identified several outliers. These outliers were studied case-

by-case in an attempt to find causes for their abnormal behaviour (e.g. background contamination), and are listed in Paper III.

The systematical 1σ higher flux density of the E13 data changed the previous weak excesses of several sources (just below the detection limit of $\chi_{\rm d} > 3$) , to detected excesses. However, in order to avoid overestimating the excess amount, we define two sets of limits, i.e. marginal excesses with $3 < \chi_{\rm d} < 5$, and detected excesses with $\chi_{\rm d} > 5$.

The remaining new excess sources, with excesses that do not seem to be caused by anything other than circumstellar dust, are singled out. There are 17 new possible excesses, and one of these has $\chi_{\rm d} > 5$, i.e. HIP 99240 (δ Pavonis, HD 190248) from the E13 data set. The δ Pav source exhibits a 7.6σ excess at 100 μm, while it corresponds well with the stellar photospheric model at both 70 and 160 μm. This is a very steep excess which is unusual for dust excesses.

5.1 Data reduction

The observations were reduced using HIPE, version 13.0.0, PACS calibration version 69. The reduction is described in more detail in section 2.2 of Paper III. In short;

we used high-pass filters that eliminate background structures larger than $82''$ and $102''$ at 100 and 160 μm, while masking sources that are stronger than $10 \times \sigma$, to reduce the shot noise. Deglitching was done with built-in tasks in HIPE and a drizzling method was used to obtain the final image scales ($1''$ per pixel at 100 μm and $2''$ per pixel at 160 μm).

5.2 Flux density and error estimates

Flux densities were estimated with aperture photometry, using built-in commands in HIPE.

The coordinates for each source were first found using the built-in Gaussian fitting tools (called *sourceFitting*). We used the tabulated J2000 coordinates of each source[1], and compensated for 10 years of proper motion (the data were observed during 2009 to 2011) to identify the main source (more accurate time-constraints were used in cases of very high proper motion). We then fitted a 2D Gaussian on each of the sources at each wavelength, and obtained the source's angular coordinates, pixel coordinates in the image, and the corresponding standard deviation (std) of the Gaussian fit.

Point source flux densities were estimated with the standard method described by Balog et al. (2014), i.e. the total flux density inside a certain aperture divided by the corresponding Encircled Energy Fraction (EEF). We have not applied any colour corrections in order to keep our flux estimates directly comparable with those of Eiroa et al. (2013) and Montesinos et al. (2016).

The flux density of an extended source can be estimated with larger apertures. These were identified by comparing the full width half maximum (FWHM) of the 2D Gaussian fits with the beam FWHM (HPBW). The sizes of the extended aperture were determined from the ratio of the source FWHM to the HPBW. The EEF was approximated linearly from this ratio. This works well for marginally extended sources, while large extended sources, with FWHM is $\gtrsim 1.5$ times the HPBW, require more detailed analysis to correctly estimate their total flux

[1] As listed by the SIMBAD Astronomical Database `http://simbad.u-strasbg.fr/simbad/`.

densities. These cases are commented as "special source" in Section 5.2 of Paper III, and our results are flagged as dubious where necessary.

The uncertainty was estimated from the background around each source, similar to Eiroa et al. (2013). We measured the total fluxes of 40 squares (with the same size as the aperture used on the source), put at random positions in annulii usually between 10″ to 20″ from the source aperture. The annulii and positions were varied to avoid nearby sources. The background error is the std of the fluxes, multiplied by $\sqrt{1+1/N}$ (where $N = 40$, the number of background squares). The final error estimate is then given by the quadratic sum of the background error and a calibration error of 5% (see Balog et al. 2014).

The SNR we use is the final total flux density of the source divided by the error estimate described here. Sources with an SNR > 5 are considered as detected. We can compare this with the SNR that Eiroa et al. (2013) used, i.e. $F_{\rm obs} \times EEF/{\rm Noise}$. They used a detection limit of $F_{\rm obs} \times EEF/{\rm Noise} > 3$, which is comparable to our SNR > 5 limit. Note that we did not redefine the old upper-limit sources.

5.3 Discussion

We use several diagnostics to compare the newly reduced data with the older data set. As an initial diagnostic, we compared the flux densities directly, shown in Figure 5.1. We see that there is a spread in the data points, but that they are generally well assembled along the diagonal.

We also linearly fitted the fluxes of the detected sources to compare the estimates. However, this did not shed much clarity on the quality of the data. The fits we found are

$$\begin{cases} F_{\rm old}(100\,\mu{\rm m}) = {\rm F}_{\rm new}(0.94 \pm 0.04) + 0.61 \pm 0.52;\ {\rm E13\,\&\,M16} \\ F_{\rm old}(100\,\mu{\rm m}) = {\rm F}_{\rm new}(0.93 \pm 0.04) + 0.13 \pm 0.39;\ {\rm E13} \\ F_{\rm old}(100\,\mu{\rm m}) = {\rm F}_{\rm new}(1.05 \pm 0.06) + 0.15 \pm 0.56;\ {\rm M16} \end{cases} \tag{5.1}$$

$$\begin{cases} F_{\rm old}(160\,\mu{\rm m}) = {\rm F}_{\rm new}(0.87 \pm 0.08) + 4.38 \pm 0.26;\ {\rm E13\,\&\,M16} \\ F_{\rm old}(160\,\mu{\rm m}) = {\rm F}_{\rm new}(0.90 \pm 0.08) + 2.69 \pm 0.48;\ {\rm E13} \\ F_{\rm old}(160\,\mu{\rm m}) = {\rm F}_{\rm new}(0.80 \pm 0.10) + 8.82 \pm 0.60;\ {\rm M16} \end{cases} \tag{5.2}$$

where $F_{\rm old}$ denotes the older flux density estimates by Eiroa et al. (2013) and Montesinos et al. (2016), and $F_{\rm new}$ are our estimates.

We see that these fits are close to the diagonal $F_{\rm old} = F_{\rm new}$, especially at 100 μm, while the fits are less accurate at 160 μm, due to both the larger uncertainties at this wavelength and that we have fewer detected sources. In most cases we find that the slope of the line is < 1, which implies that our new flux estimates are higher than the old ones (except for the M16 sources at 100 μm). There are few detected sources at small flux densities at 160 μm, which results in a large offset term.

Additionally, we compared the SNR of the old and new estimates to look for other systematic differences in our estimates. The old SNRs are plotted against the new ones in Figure 5.2 and we can see that our estimates have, in general, higher SNR, up to a ${\rm SNR} \approx 20$. The dashed line is the diagonal, for reference, while the dotted lines are ${\rm SNR}_{\rm old} > 3 \times {\rm SNR}_{\rm new}$ and ${\rm SNR}_{\rm new} > 3 \times {\rm SNR}_{\rm old}$. We see that there are only a few outliers in the SNR comparison,

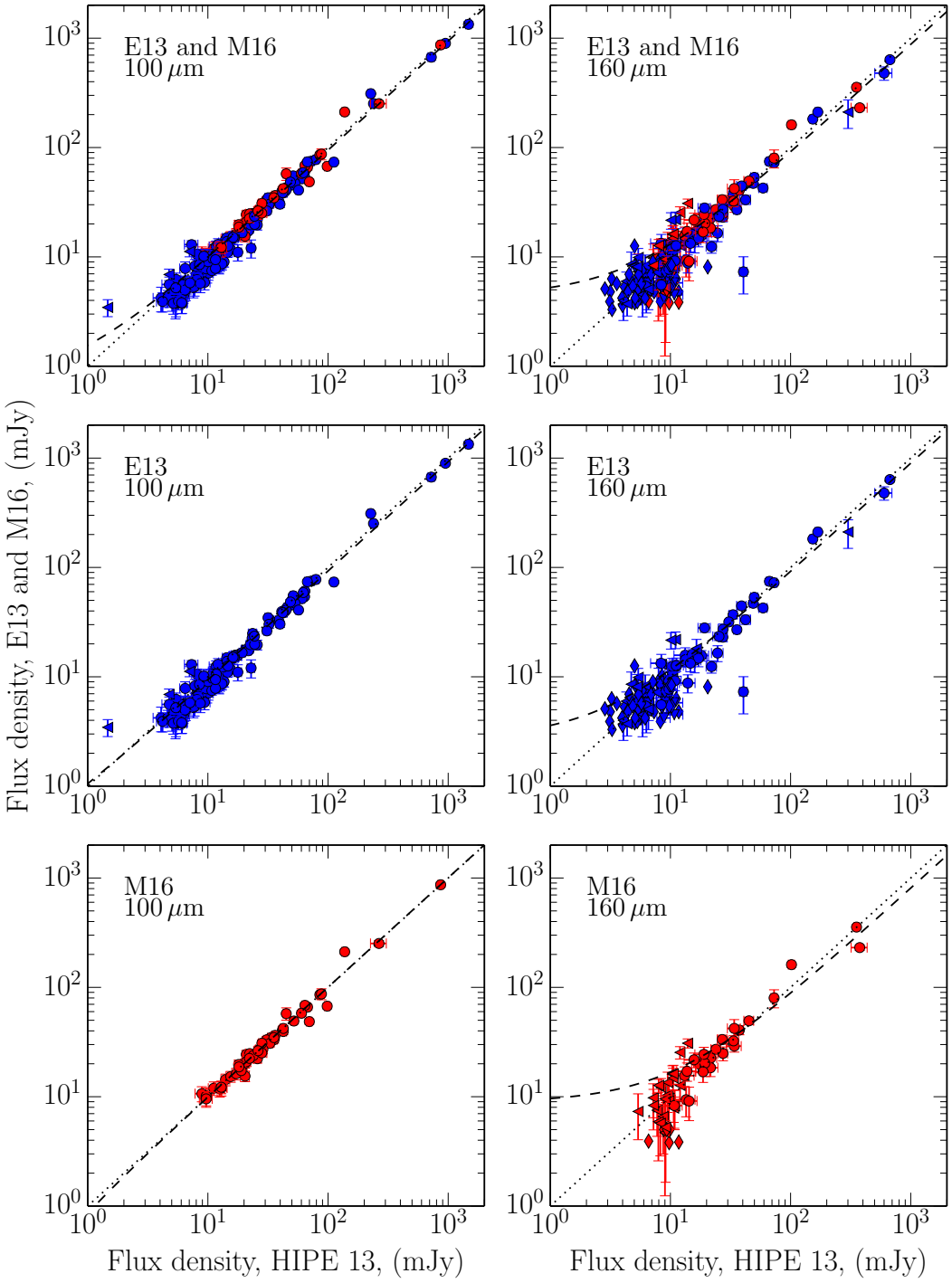

Figure 5.1: Flux density estimates. The y-axis is the older reduction flux density estimates and the x-axis is the flux densities estimated in this work. The blue data points are E13 sources and the red data points are M16 sources. Triangles are $3\,\sigma$ upper limits, pointed in the correct direction. Diamonds are upper limits in both the older estimates and in this work. The dotted line is the diagonal (only for reference), and the dashed line is the line of regression for the detected sources. A logarithmic scale is used due to the large flux density range of the sources.

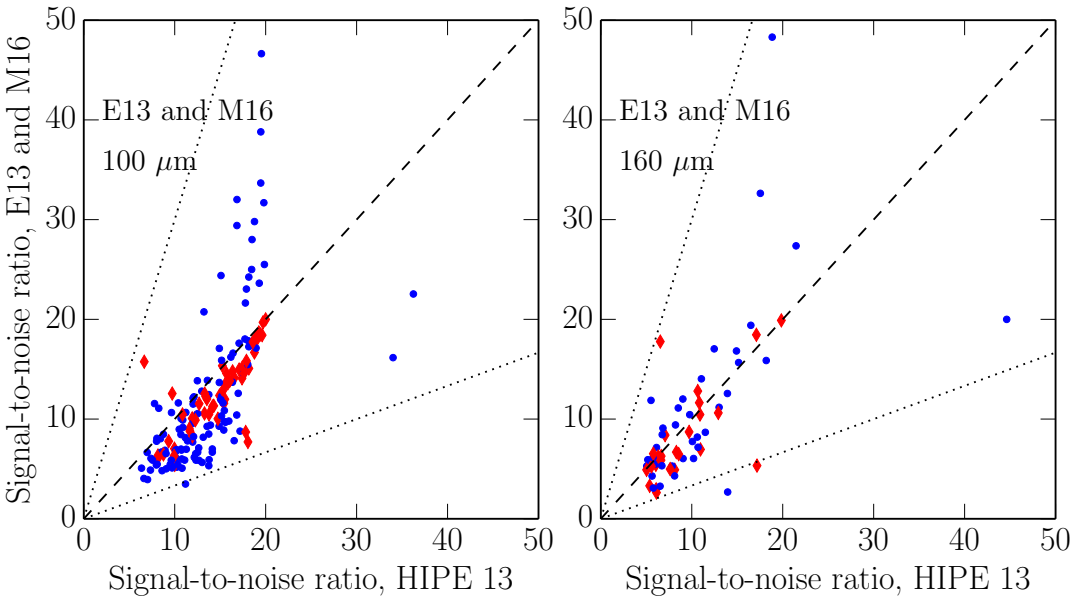

Figure 5.2: Signal-to-noise estimates. The y-axis are the older estimates SNRs, and the x-axis are the SNRs from this work. The blue dots are the E13 sources and the red diamonds are the M16 sources. Only detected sources are shown. The dashed line is the diagonal, and the two dotted lines indicate where $\mathrm{SNR}_{\mathrm{old}} > 3 \times \mathrm{SNR}_{\mathrm{new}}$ the reverse.

and these are listed in Paper III. The feature at $\mathrm{SNR}_{\mathrm{new}} \sim 20$ is most probably due to our flux estimation scheme, which is not optimised for estimating flux densities of stronger (and more extended) sources.

The source strength of all sources are also plotted in the all-sky map of Figure 5.3, where the size of each ring indicates the SNR normalised by the observation duration (as it is stated in the Herschel Science Archive). The case-study sources presented in this thesis are also indicated in this figure. We can see that the SNRs are homogeneously distributed over the sky, and that high noise regions were avoided during the source selection process.

Another, more useful diagnostic tool, is the Gaussian flux density comparison, χ_{F}, defined as

$$\chi_{\mathrm{F}} = \frac{F_{\mathrm{new}} - F_{\mathrm{old}}}{\sqrt{\sigma^2_{\mathrm{new}} + \sigma^2_{\mathrm{old}}}} \tag{5.3}$$

where the σ parameters are the uncertainties, from which we define the parameter $\sigma_{\mathrm{F}} = \sqrt{\sigma^2_{\mathrm{new}} + \sigma^2_{\mathrm{old}}}$. Histograms of χ_{F} are plotted in Figure 5.4. We have also plotted Gaussians on top of these histograms, that are based on the data's mean and standard deviations (std) with the dashed curves, and median and median absolute deviation (MAD) with the solid curves. These numbers are summarised in Table 5.1.

With the χ_{F} we find systematically higher flux density for the sources. However, we also see that this is primarily due to the E13 sources, for which we find $\sim 1\sigma_{\mathrm{F}}$ higher flux densities. Whereas for the M16 data we find a significantly smaller offset. This shows us that

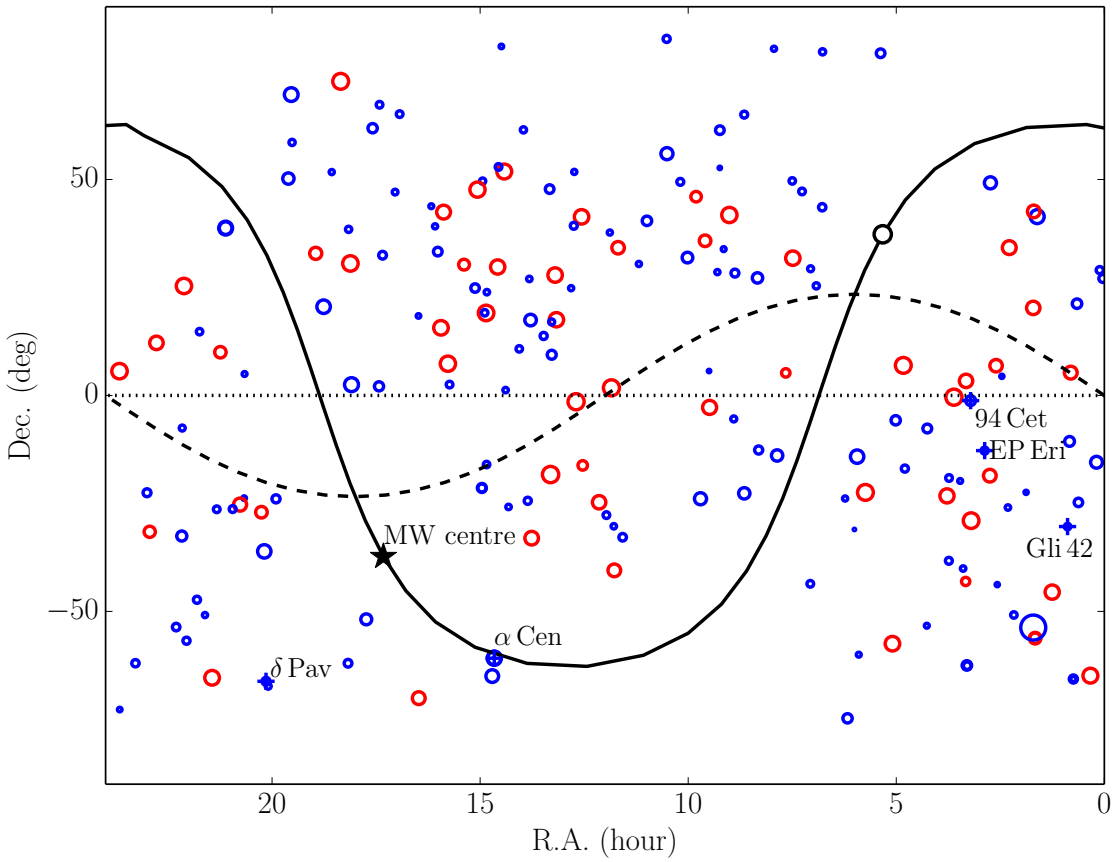

Figure 5.3: An all-sky map of the whole dataset, blue for E13 sources and red for M16 sources. The size of each ring is proportional to the relative SNR (normalised to observation duration) at 100 μm. The black curve is the MW where the centre (black star) and anti-centre (white circle) are indicated, the dashed black curve is the ecliptic and the dotted line is the equator. The individual sources that are studied in this thesis are indicated in the figure by name.

Montesinos reduction with HIPE 10 is not that different from using HIPE 13, and also confirms that our reductions are accurate. We see a higher spread due to outliers when using standard deviation, while the MAD numbers are smaller since median statistics is less sensitive for outliers.

The dust excess "strength" is similarily defined by a $\chi_{\rm d}$ parameter that is defined as

$$\chi_{\rm d} = \frac{F_{\rm obs} - F_{\rm phot}}{\sqrt{\sigma_{\rm obs}^2 + \sigma_{\rm phot}^2}} \tag{5.4}$$

where $F_{\rm obs}$ and $\sigma_{\rm obs}$ denote the observed flux densities and error bars, and $F_{\rm phot}$ and $\sigma_{\rm phot}$ are the flux densities and error bars for the stellar photospheric SED models that were extracted from the PHOENIX/GAIA grid (Brott & Hauschildt 2005) by Eiroa et al. (2013) and Montesinos et al. (2016). To quote Montesinos et al. (2016), incorporating $\sigma_{\rm phot}$ does not give noticeable effects on $\chi_{\rm d}$ as it amounts to $\sim 1\%$ of the predicted flux density.

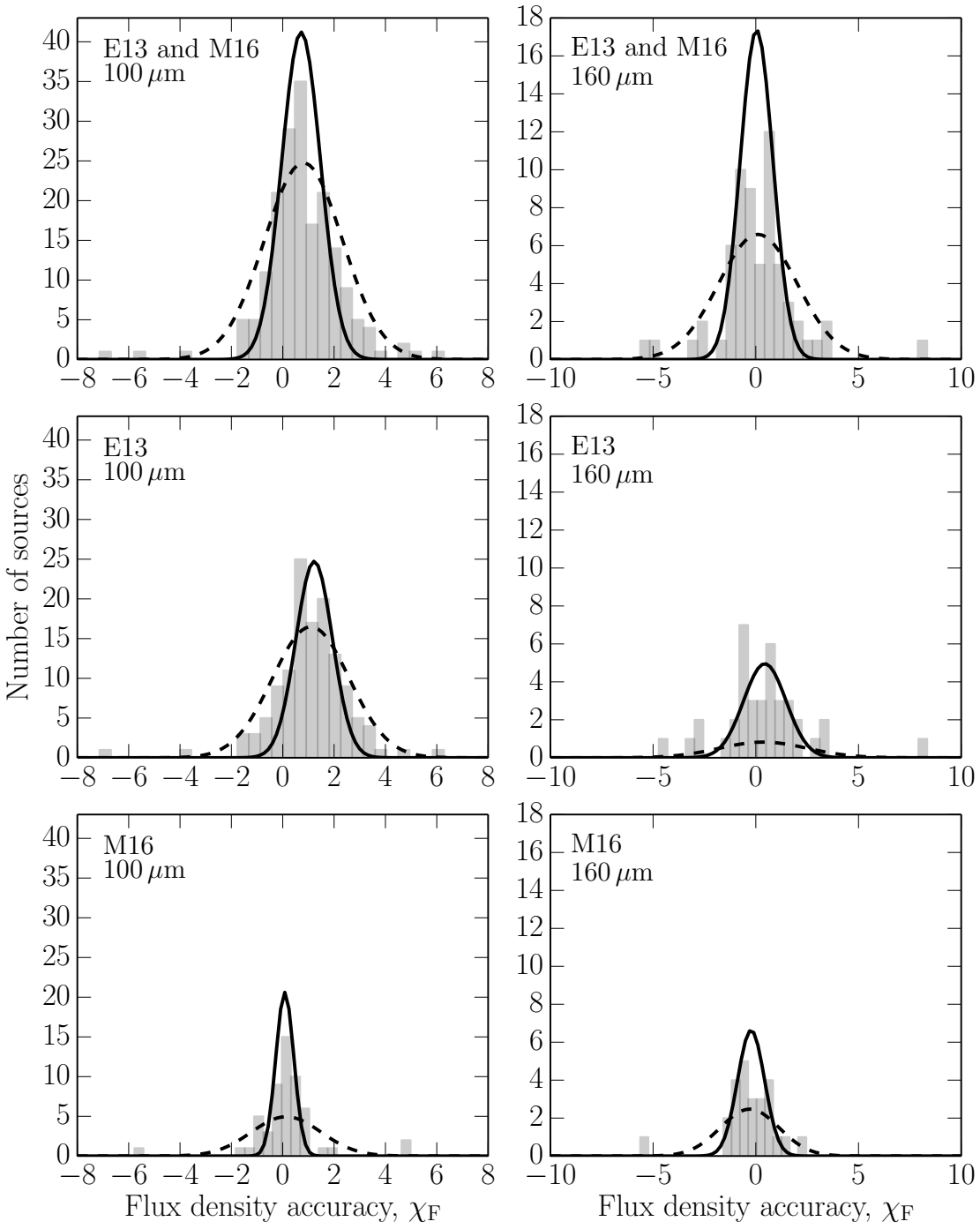

Figure 5.4: Histograms of χ_F at each wavelength for all sources (E13 and M16 in the top row), for only E13 (the middle row), and for only M16 sources (the third row). The dashed curve is a Gaussian based on the data's standard deviation and mean values, and the solid curve is a Gaussian based on the data's MAD and median values (Table 5.1).

Table 5.1: Parameters from χ_F for Gaussian fits.

Wavelength	Data set	Mean	STD	Median	MAD
100 μm	E13 & M16	0.81	1.51	0.72	0.76
100 μm	E13	1.09	1.50	1.23	0.71
100 μm	M16	0.14	1.36	0.08	0.35
160 μm	E13 & M16	0.10	1.91	0.04	0.80
160 μm	E13	0.37	2.14	0.44	1.03
160 μm	M16	−0.30	1.42	−0.23	0.66

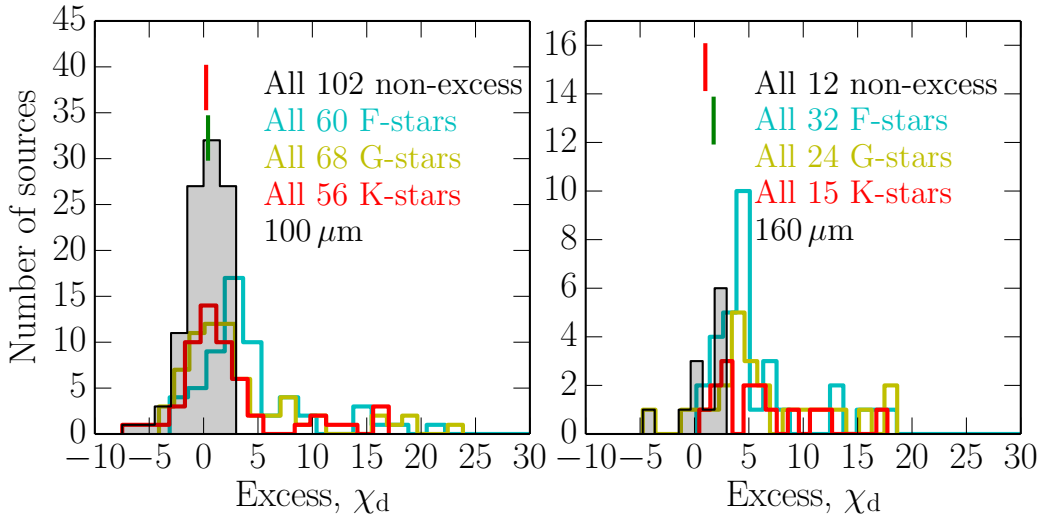

Figure 5.5: Histograms of χ_d at each wavelength of all detected stars. The mean (red line) and median (green line) of χ_d for all stars with $\chi_d < 3$ are also indicated.

A histogram of all detected sources with excesses $\chi_d < 30$ is shown in Figure 5.5. We can compare this figure with figure 6 of Eiroa et al. (2013) and figure 5 of Montesinos et al. (2016). They showed that the non-excess sources have a negative average of χ_d. However, when we measure the mean and median χ_d of non-excess sources from our estimates we now find positive values instead. The average value is 0.37 and the median is 0.69 for non-excess sources at 100 μm. This is probably due to the higher flux densities we estimate for the E13 sources.

The negative average of χ_d was attributed to the chromospheric temperature minimum that was detected in α Cen by Liseau et al. (2013) and in Paper I. These results are a good reminder that the effects of reducing data with older and newer software can be significant. The actual reasons behind these results must be investigated in detail before we can draw any conclusions on the incidence of this temperature minimum.

Finally, we identified new excess sources that are listed in Table 5.2. There are 17 sources with $\chi_d > 3$. These were found to not be contaminated, or show any other reason to their

Table 5.2: New (not dubious) excess sources. Bold face indicate new excesses that exceed $\chi_{\rm d} > 5$.

HIP	New $\chi_{\rm d}(100)$	New $\chi_{\rm d}(160)$	Old $\chi_{\rm d}(100)$	Old $\chi_{\rm d}(160)$	Catalogue
910	3.84	-0.90*	2.31	N/A*	E13
3497	4.46	1.23*	0.95	N/A*	E13
3909	4.09	0.62*	0.94	N/A*	E13
7513	4.26	4.81	1.69	1.82	E13
17651	3.76	-0.27*	2.56	-0.01	M16
36439	3.38	-0.39*	0.13	N/A*	E13
37279	2.94	3.65	2.99	3.81†	M16
43587	-0.12	3.50	-1.15	0.27*	E13
44897	3.15	0.34*	-0.25	N/A*	E13
56997	3.13	0.68*	0.35	1.97	M16
65026	4.91	0.71*	0.29	N/A*	E13
67620	4.61	0.36*	1.60	1.31*	E13
68184	3.04	0.03*	-0.13	N/A*	E13
89937	1.24	3.35	0.59	2.83	M16
91009	3.81	0.71*	1.18	N/A*	E13
96100	3.47	1.56	-0.70	0.97	E13
99240	**7.58**	0.18	1.95	-0.12	E13

Notes. * Based on estimate that is an upper limit. † Older estimate that was considered dubious.

excesses. Of these, there is only one source with $\chi_{\rm d} > 5$. This is HIP 99240, or δ Pavonis, for which we measured a 7.6σ excess at 100 μm.

The star, δ Pav is a remarkable Solar-like star due to its high age. Eiroa et al. (2013) list it as a G5 IV–V star with the effective temperature 5597 K, an age between 4.5 to 8.3 Gyr, and the relatively high metallicity of [Fe/H] around 0.30 or 0.33 (Boesgaard et al. 2015). Mamajek & Hillenbrand (2008) gives it the classification G8 IV, and an age of ~ 6.2 Gyr. It is evidently a very old Solar-type star and there are indications that it is just about to leave the main sequence and evolve into a red giant. There exist no previous evidence for either dust discs nor planets (Eiroa et al. 2013; Moro-Martín et al. 2015). If our data analysis holds true, we will have an exciting prospect of studying dust of a nearby, relatively old, Solar-type star. However, the excess is very steep which makes dust an improbable explanation.

5.4 Conclusions

Our conclusions can be summarised as follows:

– Our reductions and subsequent flux estimates agree well with those of Montesinos et al. (2016) for the additional 55 sources that we denote as M16 sources. However, there exist non-negligible differences when comparing with the results of Eiroa et al. (2013) for the original 133 DUNES sources (E13 sources). This means that a marginal difference in flux estimates can be attributed to differences in versions of HIPE and the PACS

calibration tree.

– We can confirm all the excess sources found by both Eiroa et al. (2013) and Montesinos et al. (2016).

– We find marginally higher SNR values for most sources up to an SNR of 20, than that of both Eiroa et al. (2013) and Montesinos et al. (2016) did.

– We find a $1\sigma_{\rm F}$ higher flux density for the E13 sources, resulting in 17 new possible dust excess sources. One of these fulfils $\chi_{\rm d} > 5$, and that is the Solar-like star δ Pav (HIP 99240, HD 190248).

Chapter 6

Additional studies: EP Eridani and Gliese 42

This chapter treats additional studies I made on two interesting cases that were singled out by Eiroa et al. (2013) from the DUNES catalogue (among other sources) because of the confusing backgrounds in their photometry. The sources are EP Eridani and Gliese 42, which both host far-infrared excesses that were observed with *Spitzer*/MIPS and *Herschel*/PACS, and are interpreted as circumstellar dust emission. Gli 42, for example, exhibited a significantly higher 70 μm flux density in the older MIPS observations, than with PACS. However, in the PACS images we see how Gli 42 is surrounded by several background sources that have most probably contaminated the MIPS data. EP Eri, on the other hand, exhibit an extended source but does not seem to be contaminated, even though there are several background sources in the field.

As mentioned earlier, background confusion is an important issue at 100 and 160 μm (see Section 2.3.1). Number counts of high-redshift galaxies at 100 μm (Berta et al. 2011) indicate that a few hundred galaxies deg^{-2} can be expected with flux densities higher than around 6 mJy (three times the expected noise level with *Herschel*/PACS at 100-160 μm).

As for 94 Cet, we observed these two fields at 870 μm with APEX-LABOCA, and compared them with *Herschel* observations as well as with older archived optical observations. We also searched catalogues (Two Micron All Sky Survey, 2MASS[1], Skrutskie et al. 2006, and NASA/IPAC EXTRAGALACTIC DATABASE, NED[2], Helou et al. 1991) to identify the background sources. The APEX observations also provides us with constraints on the Rayleigh-Jeans tail of the dust emission.

Similar as with and 94 Cet, we formulated dust disc models and simulated radiative transfer through the discs with RADMC-3D to obtain model SEDs. We also compared the stellar SEDs with model SEDs from high-redshift galaxies because of the background sources surrounding Gli 42.

We found that EP Eri's extended emission fits well with a possible face-on dust disc smaller than 110 AU in radius, with an inner hole of 5 to 10 AU, and a luminosity ratio of $(2.9 \pm 0.2) \times 10^{-5}$. Gli 42's excess is difficult to fit by a "standard" dust SED and we

[1] http://www.ipac.caltech.edu/2mass/releases/allsky/
[2] http://ned.ipac.caltech.edu/

Table 6.1: Stellar properties.

Property	EP Eridani HIP 13402, HD 17925	Gliese 42 HIP 4148, HD 5133
ICRS (J2000) R.A.	2h 52m 32.12s	0h 53m 01.13s
ICRS (J2000) Dec.	-12°46′10.″96	-30°21′24.″90
Spectral class	K1 V - K3 V	K2 V - K3 V
Effective temperature (K)	5217	4940
Luminosity ($L_\odot$)	0.39	0.30
Mass ($M_\odot$)	0.89[a]	0.74*
Radius ($R_\odot$)	0.77†	0.79[b]
$\log(g)$	4.57	4.70
Metallicity [Fe/H]	0.10	-0.15
Age (Gyr)‡	0.14 - 0.40	1.79 - 3.64
Distance (pc)	10.35 ± 0.04	12.22 ± 1.58
Proper motion (mas yr^{-1}), R.A.	397.41 ± 0.45	620.35 ± 0.63
Proper motion (mas yr^{-1}), Dec.	-189.32 ± 0.36	30.26 ± 0.48

Notes. The general reference for all parameters is Eiroa et al. (2013, and references therein) except when stated otherwise. * Estimate from $L \propto M^4$. † Estimate from Stefan-Boltzmann law $L \approx 4\pi R^2 \sigma T^4$. ‡ Age range based on both X-ray luminosities and activity index $\log R'_{\rm HK}$.

References. [a] Metchev et al. (2004). [b] Fracassini et al. (1988).

had to use flatter grain size distributions to achieve colder dust. The best fit model has the luminosity ratio $(8.7 \pm 1.0) \times 10^{-6}$. However, we could also find a wide range of FIR galactic SEDs that fit these data. These correspond to a background galaxy with a redshift between 0.7 and 1.9 and IR luminosities between 0.4 to $8.3 \times 10^{12}\, L_\odot$. Thus, the conclusion we can draw about the real nature of the Gli 42 excess, is that it is unclear.

6.1 Presentation of the sources

The physical properties of EP Eri and Gli 42 are summarised in Table 6.1.

6.1.1 EP Eridani

EP Eridani (HIP 13402, HD 17925) is one of the younger stars in the DUNES archive, estimated to be between 140 to 400 Myrs old. It is a warm K star at 5217 K, slightly cooler than the sun. It has been speculated that it might be an unresolved binary, however, Cutispoto et al. (2001) showed that this was not the case.

Its dust excess was observed with *Spitzer*/MIPS at 70 μm (Trilling et al. 2008) and was later expanded with *Herschel*/PACS and SPIRE at 100, 160, 250, 350, and 500 μm. Eiroa et al. (2013) estimated a dust black body temperature of 52 K, indicating a disc radius of 17.9 AU.

Table 6.2: Observing log.

Source	Instrument/ Mode	Obs/Pgm ID	$\lambda_{\rm eff}$ (μm)	HPBW ($''$)	Observing Date year–mo–day	$t^a_{\rm int}$ (s)	Offset ($''$)^b
EP Eri	*Herschel*-PACS	1342215731	100	6.8	2011-02-26	1440	2.45
		1342215732	160	11.4	2011-02-26	1440	2.45
	Herschel-SPIRE	1342213481	250	18	2011-01-30	307	...
		1342213481	350	25	2011-01-30	307	...
		1342213481	500	36	2011-01-30	307	...
	APEX-LABOCA	090.F-9302(A)	870	18.1	2012-08-14 – 2012-11-26	32299	...
Gli 42	*Herschel*-PACS	1342212840	70	5.6	2011-01-18	360	2.28
		1342212842	100	6.8	2011-01-18	1440	1.65
		1342212843	160	11.4	2011-01-18	1440	3.55
	APEX-LABOCA	090.F-9302(A)	870	18.1	2012-08-18 – 2012-11-26	53365	...

Notes. ^{a} On-source integration time. ^{b} Offset between observed position and the J2000 coordinates (Table 6.1) compensated for proper motion (average offset for PACS is $2\farcs4$, Sánchez-Portal et al. 2014).

6.1.2 Gliese 42

Gliese 42 (HIP 4148, HD 5133) is also a K star, slightly cooler than EP Eri. Its excess has been previously observed with *Spitzer*/MIPS at 70 μm (Trilling et al. 2008), however, the flux density was overestimated due to the surrounding sources that were later resolved with *Herschel*/PACS. It was observed at all three PACS bands, 70, 100, and 160 μm. Eiroa et al. (2013) estimated a dust black body temperature of 32 K and a disc radius of 41.2 AU.

6.2 Observations and data reduction

The observations are described here and summarised in Table 6.2. The *Herschel* observations and data reduction were done by the DUNES team and are described in detail by Eiroa et al. (2013), and are only summarised here.

In addition to the PACS and SPIRE data, we also have access to *Spitzer*/IRS (Houck et al. 2004) spectra extracted by DUNES from *Spitzer* archival data (Eiroa et al. 2013).

Scan map observations from PACS were taken with the 100/160 channel combination, and additional observations were done with the 70/160 channel combination for Gli 42 (*Herschel*/PACS could observe in two channel modes, either at 70 μm and 160 μm, or at 100 μm and 160 μm). The final image pixel scales are $1''$ per pixel at 70 μm and 100 μm, and $2''$ per pixel at 160 μm, compared to the original $3\farcs2$ and $6\farcs4$ per pixel, respectively. Reductions were done with HIPE, version 7.2, and PACS calibration version 32.

Small map SPIRE observations were taken of EP Eri. The final image scales of these are

Table 6.3: Coordinates of background sources with a SNR larger than 3 (L refers to the LABOCA fields).

Source	R.A. (J2000) h m s	Dec. (J2000) ° ′ ″	Source	R.A. (J2000) h m s	Dec. (J2000) ° ′ ″
EP Eri*	2 52 53.30	-12 46 14.1	Gli 42*	0 53 01.78	-30 21 26.1
EP Eri–1	2 52 27.60	-12 49 06.4	Gli 42–1	0 52 57.39	-30 22 28.3
EP Eri–2	2 52 27.83	-12 45 40.6	Gli 42–2	0 52 58.72	-30 24 04.8
EP Eri–3	2 52 29.76	-12 48 09.5	Gli 42–3	0 53 00.62	-30 21 31.5
EP Eri–4	2 52 31.28	-12 48 09.4	Gli 42–4	0 53 01.33	-30 23 22.2
EP Eri–5	2 52 31.49	-12 48 54.4	Gli 42–5	0 53 01.37	-30 21 41.5
EP Eri–6	2 52 32.62	-12 47 59.1	Gli 42–6	0 53 01.95	-30 22 53.5
EP Eri–7	2 52 33.62	-12 48 53.3	Gli 42–7	0 53 02.47	-30 19 46.9
EP Eri–8	2 52 33.89	-12 45 22.2	Gli 42–8	0 53 02.65	-30 20 11.1
EP Eri–9	2 52 35.56	-12 46 03.9			
EP Eri–10	2 52 35.69	-12 46 59.1			
EP Eri–L1	2:52:04.38	-12:45:12.8	Gli 42–L1	0 53 00.08	-30 15 34.7
EP Eri–L2	2:52:10.93	-12:43:08.5	Gli 42–L2	0 53 16.74	-30 26 39.0
EP Eri–L3	2:52:21.60	-12:40:36.5	Gli 42–L3	0 53 18.01	-30 23 42.7
EP Eri–L4	2:52:29.26	-12:41:01.0			
EP Eri–L5	2:52:31.44	-12:42:05.0			
EP Eri–L6	2:52:35.52	-12:52:08.5			
EP Eri–L7	2:52:41.24	-12:49:12.7			
EP Eri–L8	2:52:41.52	-12:47:36.6			

Notes. * Observed coordinates, not from references.

6″, 10″, and 14″ per pixel for 250 μm, 350 μm, and 500 μm, respectively.

We used the bolometer camera LABOCA at APEX to observe these sources at 870 μm, project id 090.F-9302(A). A spiral mapping mode was used during observations to fill the undersampled parts of the array. These data were reduced with CRUSH with the deep field setting.

6.3 Results

The last column in the observing log in Table 6.2 refers to the offset, i.e. the difference between the telescope's commanded position and the observed position of the star. These are small when compared to the average offset of 2.″4 for PACS (Eiroa et al. 2013; Sánchez-Portal et al. 2014). The observed positions were found by fitting Gaussians to the sources, and the coordinates of all detected sources in the PACS and LABOCA fields are listed in Table 6.3.

The photometry of the sources are summarised in Table 6.4 and plotted in Figure 6.1. Both stellar sources exhibit significant excesses at PACS wavelengths of up to 38 σ when compared to a photospheric model (σ refers to the uncertainty at each wavelength). The photospheric models were computed from the high-resolution PHOENIX/GAIA grid (Brott

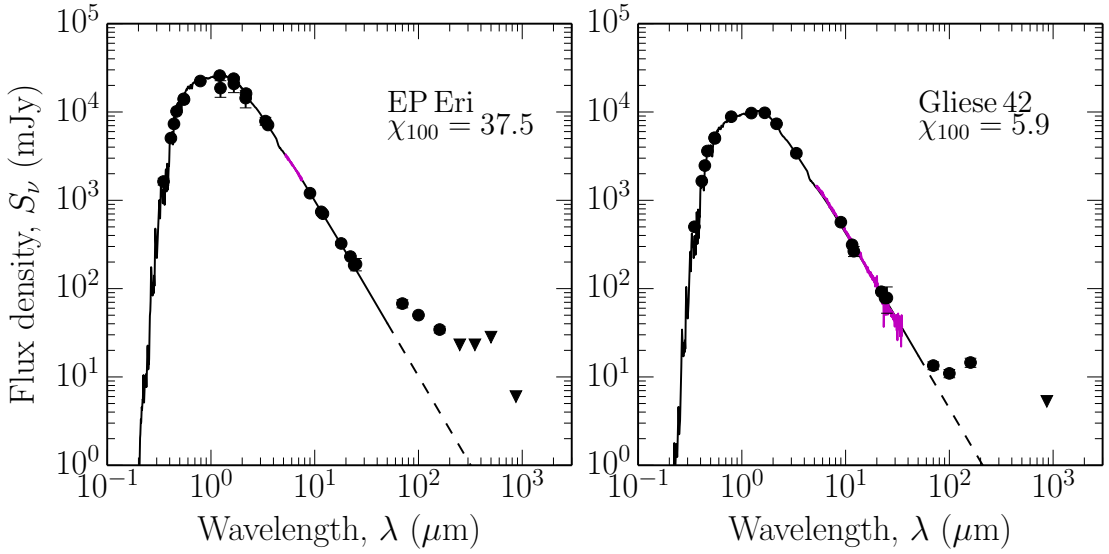

Figure 6.1: Observed photometry and model SEDs of EP Eri and Gli 42. The model photosphere is shown as a black line where the dashed part is an extrapolated Rayleigh-Jeans tail of the stellar photosphere from 50 μm, under the assumption of black body emission. The plotted photometric data points and 1 σ uncertainties are presented in Table 6.4 (several error bars are smaller than the data point symbol) and upper limits (black triangles) are 3 σ limits. The magenta spectra denotes the observed *Spitzer*/IRS spectra. The excesses are indicated by the χ_{100} values where $\chi_{100} = (S_{\rm obs}(100) - S_{\rm phot}(100))/\sigma_{100}$.

& Hauschildt 2005) with the parameters summarised in Table 6.1.

The excesses over the photospheric models are detected at the wavelengths 70, 100, and 160 μm. These are 6.7 σ, 37.5 σ, and 11.2 σ for EP Eri, and 3.4 σ, 5.9 σ, and 8.1 σ for Gli 42 at each wavelength, respectively.

The fields observed with *Herschel* and APEX are shown in Figures 6.2 and 6.3. EP Eri has extended emission in the PACS observations but is undetected in the LABOCA field. We mentioned earlier that the MIPS observations of Gli 42 at 70 μm gave a significantly higher flux density than the later PACS 70 μm observations. We can clearly see in the PACS observations how Gli 42 is surrounded by background sources, which must have contaminated the previous MIPS observations.

We also searched catalogues, e.g. 2MASS and NED, for known sources in the fields to identify the background sources. We compared the observations with older surveys, e.g. the Palomar Sky Survey (POSS)[3] and POSS infrared images[4], to see if any of the PACS background sources were visible there.

We detect a few other sources in the LABOCA images that do not coincide with other previously known sources nor the PACS sources. These are listed in Table 6.3 (they are positioned outside the PACS fields and are not visible the figures).

[3] `https://archive.stsci.edu/cgi-bin/dss_form`
[4] `http://irsa.ipac.caltech.edu/frontpage/`

Table 6.4: Photometry and FIR/flux densities.

$\lambda_{\rm eff}$ (μm)	S_ν(EP Eri) (mJy)	S_ν(Gli 42) (mJy)	Photometry Reference
0.440	7335 ± 135	2474 ± 46	Johnson B (1)
0.550	13840 ± 255	5025 ± 93	Johnson V (1)
0.790	22420 ± 413	8842 ± 163	Cousins I (1)
1.235	18640 ± 3979	9720 ± 260	2MASS J (2)
1.662	20810 ± 4246	9788 ± 262	2MASS H (2)
2.159	14360 ± 3228	7352 ± 210	2MASS K_s (2)
1.215	25830 ± 952	...	J (3)
1.654	23830 ± 878	...	H (3)
2.179	16150 ± 595	...	K (3)
3.547	7127 ± 263	...	L (3)
3.353	7883 ± 807	3410 ± 226	WISE (W1) (4)
11.561	740.4 ± 9.5	313.2 ± 4.9	WISE (W3) (4)
22.088	230.5 ± 4.5	92.18 ± 2.38	WISE (W4) (4)
0.349	1632 ± 145	501.7 ± 9.2	Strömgren u (5)
0.411	5060 ± 219	1650 ± 30	Strömgren v (5)
0.466	10160 ± 193	3614 ± 67	Strömgren b (5)
0.546	14080 ± 259	5112 ± 94	Strömgren y (5)
24	184.2 ± 3.8	78.30 ± 1.60	MIPS (6)
70	67.70 ± 7.06	37.10 ± 6.59	MIPS (6)
9	1203 ± 17	565.2 ± 5.7	Akarai (7)
18	324.7 ± 17.0	...	Akarai (7)
12	705.9 ± 35.3	265.2 ± 34.5	IRAS (8)
25	189.2 ± 30.3	78.57 ± 25.93	IRAS (8)
70	...	13.45 ± 1.37	PACS (9)
100	50.12 ± 1.11	10.97 ± 1.17	PACS (9)
160	34.40 ± 2.94	14.56 ± 1.72	PACS (9)
250	$\leq 23.1^*$	...	SPIRE (9)
350	$\leq 23.1^*$	...	SPIRE (9)
500	$\leq 28.2^*$	...	SPIRE (9)
870	$\leq 5.99^*$	$\leq 5.29^*$	LABOCA (10)

Notes. The first column lists the effective wavelengths, the second and third column lists the flux density at each wavelength for EP Eri and Gli 42 respectively, and the fourth column lists the references. * 3σ upper limits.

References. (1) *Hipparcos*. (2) 2MASS Point Source Catalogue, II/246 in Vizier. (3) Several sources, see references in Eiroa et al. 2013. (4) WISE All-Sky data Release Catalogue, II/311 in Vizier. (5) Hauck & Mermilliod (1997). (6) *Spitzer*/MIPS. (7) AKARI/IRC mid-IR all-sky Survey, II297 in Vizier, colour corrected. (8) IRAS Faint Source Catalogue, II/125 in Vizier, colour corrected. (9) *Herschel*-PACS and SPIRE, Eiroa et al. 2013, colour corrected. (10) Our work.

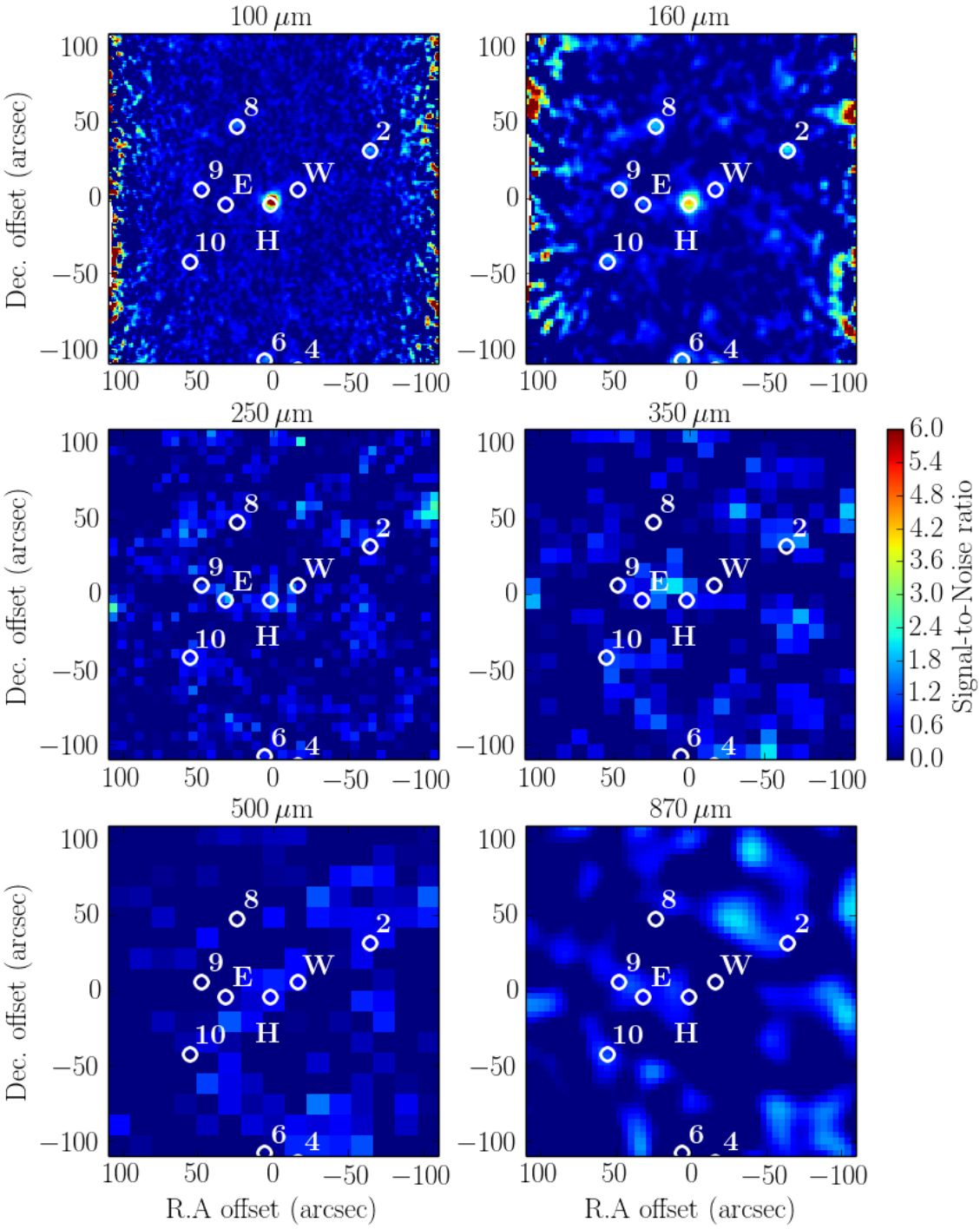

Figure 6.2: The EP Eri *Herschel* and APEX observations. The PACS background sources are numbered in the same order as in Table 6.3, where H denotes the star (H as in *Hipparcos*), and E and W denote the eastern and western sources. LABOCA background sources are all outside the PACS fields and not shown here.

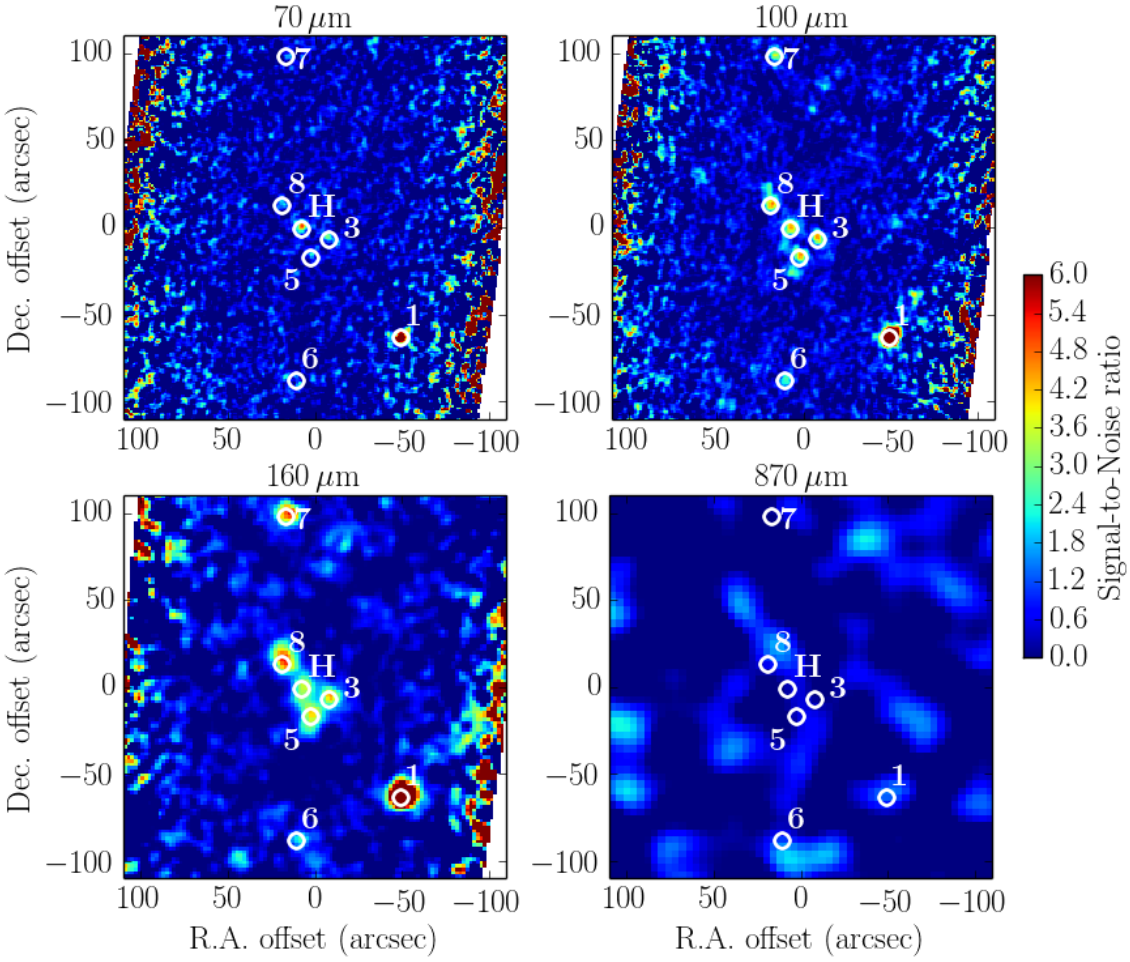

Figure 6.3: The Gli 42 *Herschel* and APEX observations. The PACS background sources are numbered in the same order as in Table 6.3, where H denotes the star (H as in *Hipparcos*). LABOCA background sources are all outside the PACS fields and not shown here.

6.3.1 The EP Eridani images

The observed offset for EP Eri is 2.″5, similar to the average offset given for PACS (Table 6.2, Sánchez-Portal et al. 2014).

The *Herschel*/PACS, SPIRE and APEX-LABOCA observations are shown in Figure 6.2 where the background sources are numbered as in Table 6.3.

Figure 6.4 shows the main source after subtraction with a PSF to visualise the extent of the source (the HPBW with a scan speed of 20″ sec^{-1} is 6.″8 at 100 μm and 11.″3 at 160 μm). By fitting Gaussian profiles to the main source, we estimated the diameters of the emission to 10.″9 at 100 μm and 14.″8 at 160 μm (two times the background noise was used as a lower limit, the radii are indicated with red dashed circles in Figure 6.4). These are clearly larger than the beam size and thus extended sources.

The PACS images contain 10 background sources with SNR$>$ 3 at either 100μm or 160 μm, or both. EP Eri–1 was also detected at 250μm and 350 μm. The LABOCA field

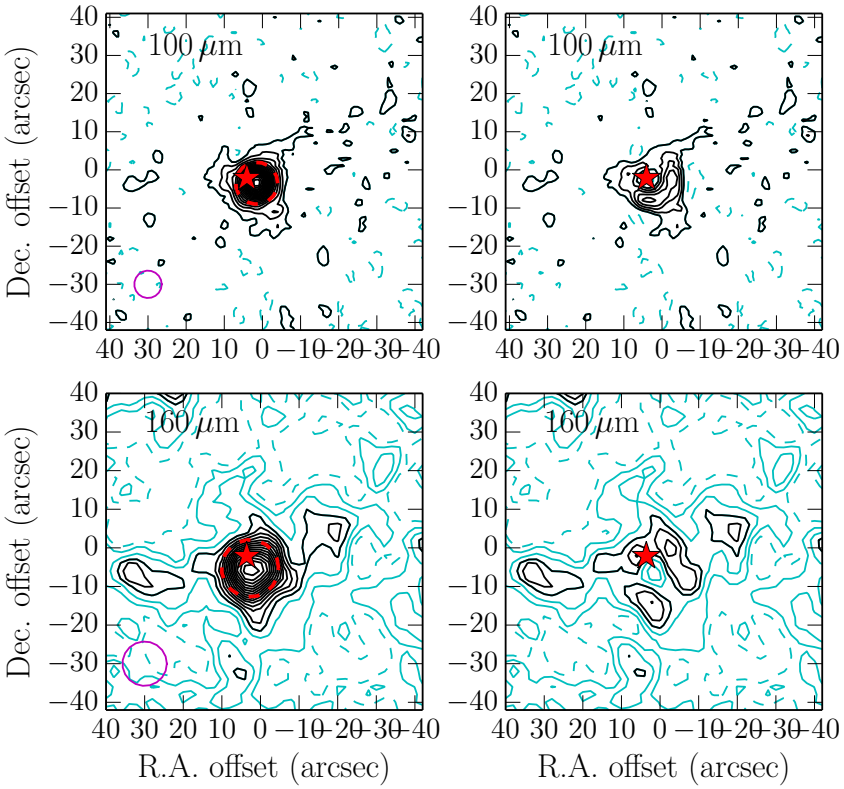

Figure 6.4: Contour plots of the area around EP Eri. Each row is for each PACS wavelength where the first column shows the observations, and the second column shows the observations subtracted by a PSF normalised to the main source flux density. Each contour corresponds to 0.03 mJy per pixel, where the cyan contours are below the corresponding RMS-level of each observation, the magenta circle is the HPBW (bottom left corner in the first column), and the dashed red circle corresponds to the measured radius of the source, i.e. $5\farcs5$ at 100 μm and $7\farcs4$ at 160 μm respectively. The image centre is at the observation coordinates and the red star is the correct position at the time of observation. $1''$ corresponds to $\sim$ 10 AU.

contains eight sources with SNR$>$ 3, although none of these are within the PACS fields.

We also found two weak sources directly to the east and west of the main source that we denoted E and W. The eastern source is only tentative at 160 μm with a SNR of 2.8 at the highest, while the western has a SNR of 5.1.

The sources we denote EP Eri–6 and EP Eri–7 coincide with known background galaxies, 2MASS J025232.62-124758.0 and 2MASS J025233.54-124850.5, respectively. The coordinates for the eastern source, EP Eri–E, coincides with the X-ray source J025234.1-124619 from the 2nd XMM-Newton Serendipitous Source Catalogue (2XMM, available through NED, Colless et al. 2003). The stronger EP Eri–W (western source) remains unidentified. We could also identify the two background sources, EP Eri–6 and EP Eri–7, in the POSS infrared image.

6.3.2 The Gliese 42 images

This Gli 42 field is more confusing due to the aforementioned number of background sources with high angular proximity to the main source.

The Gli 42 coordinates (see Table 6.2) have very small offsets from the observed emission at 70 μm and 100 μm. In Figure 6.5 we see that the images at 70 μm and 100 μm are quite clean while the surrounding background sources contaminate the main source at 160 μm. This complicated the Gaussian fitting procedure at 160 μm, resulting in a larger offset than at the other wavelengths.

The main source is treated as a point source even though the contamination at 160 μm makes it difficult to determine its angular size. The *Herschel* and APEX observations are shown in Figure 6.3, and the sources are numbered as in Table 6.3.

We detect eight background sources in the PACS-fields at 100 μm, six of these were detected at 160 μm, and only two at 70 μm.

Gli 42–4 is listed as the galaxy TGS370Z206 or 2dFGRS S370Z206 in NED, with the J2000 coordinates R.A. $0^{\rm h}\,53^{\rm m}\,01\overset{\rm s}{.}16$ and Dec. -30°23′23″.72. This galaxy is also visible in the POSS infrared images at the same J2000 coordinates. However, the sources surrounding the star (Gli 42–8, 3, and 5) are too close to the star to be visible in the POSS images due to the large stellar PSF.

However, there exist additional objects listed by NED and 2MASS in this region, none of which coincide with the observed background sources. Nevertheless, this still indicates that Gli 42 is in the direction of a cluster, or group, of galaxies. It is not strange, however, that the listed objects do not coincide with these FIR sources, because high-redshift galaxies tend to exhibit peak flux density at PACS wavelengths. So the sources we observe should be difficult to detect at optical and NIR wavelengths.

6.4 SED models

We formulated dust disc models and simulated the emission from them with RADMC-3D (see Section 2.3). This gives accurate models with which we can interpret the data. Model SEDs from Chary & Elbaz (2001) for high-redshift galaxies were also used.

The inputs are described in Section 2.3.2, and they can be summarised as (i) a 3D grid of dust mass densities, (ii) coordinates for all stars relative to the center of the grid and their SEDs, (iii) mass absorption and scattering coefficients for the dust cloud ($\kappa_{\rm abs}$ and $\kappa_{\rm scat}$).

We assumed a "standard" disc model, i.e. a flaring disc with the thickness $0.1 \times R$ (compare with e.g. β Pic, Artymowicz 1997) and the surface density distribution, $\Sigma(R) = \Sigma_0 \times (R/R_0)^{-\gamma}$.

The inner disc radius is defined from the grain sublimation temperature, $T_{\rm sub}$, which is between 1300 and 1800 K (Pollack et al. 1994; Moro-Martín 2013). The sublimation radius ($R_{\rm sub}$) is approximated by assuming black bodies, which imply that $R_{\rm sub} = 0.5\,R_\star \times (T_{\rm eff}/T_{\rm sub})^2$, where $R_\star$ is the stellar radius and $T_{\rm eff}$ is the star's effective temperature (Liseau et al. 2008).

The mass absorption coefficient ($\kappa_{\rm abs}$), and the albedo are described in Section 2.3 (see Equation Equation 2.11). We primarily used extinctions as computed by Miyake & Nakagawa (1993).

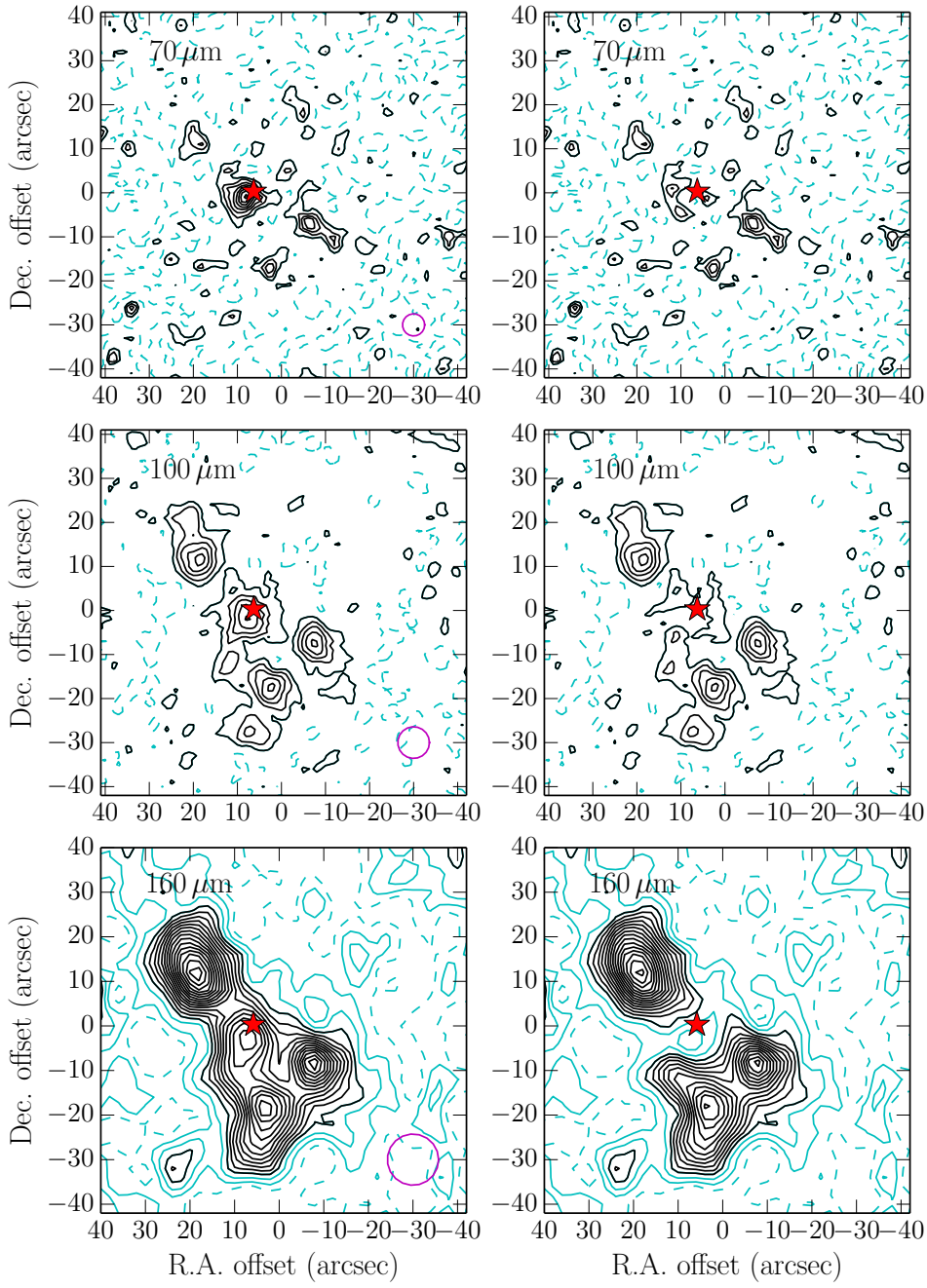

Figure 6.5: Contour plots of the area around Gli 42. Each row is for each PACS wavelength where the first column shows the observations, and the second column shows the observations subtracted by a PSF normalised to the main source flux density. Each contour corresponds to 0.03 mJy per pixel, where the cyan contours are below the corresponding RMS-level of each observation, and the magenta circle is the HPBW (bottom right corner in the first column). The image centre is at the observation coordinates and the red star is the correct position at the time of observation.

The grain size range and size distribution are crucial parameters for the extinction, and they are significant contributors to the inferred total dust disc mass (these are described in Section 2.2). The size distribution, q from Equation 2.4, was varied between 4, 3.5, 3, 2.5, and 2 (the value 3.5 is often used in the literature).

We assume an upper grain size limit of 1 mm, and the lower limit is based on an inferred blow-out radius ($a_{\rm blow-out}$ in Equation 2.3) of the grains. We found 0.2 μm for both EP Eri and Gli 42 when assuming the mass grain density of 2.5 g cm^{-3}. The smallest allowed grain size should be around 6 times the blow-out radius, ~ 1 μm, as described in Section 2.2.

With these parameters set we are able to use RADMC-3D to obtain model SEDs and synthetic images. We start the simulations with a "standard" disc using the grain size distribution with $q = 3.5$, and the surface density distribution with $\gamma = 1$. Through an iterative process we then explored the parameter space. A γ smaller than -2 is in reality a ring at the outer edge of the allowed radius, and a γ larger than 2 is instead a hot dust ring just outside the sublimation radius. We found that varying a $\gamma < -2$ gave small differences (or for a $\gamma > 2$).

The accuracy of each model was visually inspected and quantified by a reduced χ^2 defined as

$$\frac{1}{N} \times \sum_{\nu} \left[\frac{S_\nu^{\rm obs} - S_\nu^{\rm model}}{\sigma} \right]^2 , \tag{6.1}$$

where $S_\nu^{\rm obs}$ is the observed flux density and $S_\nu^{\rm model}$ is the corresponding model flux density. The sum is only over the values at the wavelengths 70, 100, and 160 μm since this is where the emission is found ($N = 3$). Each dust emission model is also quantified by the dust-to-star luminosity ratio $f_{\rm d}$.

6.4.1 Galaxy SED models

Due to the uncertainties of the nature of these sources we compared the data with dust emission from FIR background galaxies. For this reason we use the galactic SED models from Chary & Elbaz (2001) that are available online[5].

There are 105 templates available at the wavelength range 0.1 μm to 300 mm with different total IR luminosities, $L_{\rm IR}$ (defined as the total luminosity between $\lambda = 8$ μm and 1 mm).

To find fitting models we simply looped through these models at different redshifts. The redshift effects on the spectra are computed with standard cosmology assumptions, i.e. a flat Universe with $H_0 = 70\,{\rm km\,s^{-1}\,Mpc^{-1}}$, $\Omega_{\rm M} = 0.3$, $\Omega_\Lambda = 0.7$, and the redshifted flux densities are

$$S_\nu = \frac{S_\nu^0}{\nu} \frac{L_\odot}{D_{\rm L}^2} \frac{1}{4\pi} \tag{6.2}$$

where S_ν^0 is the rest frame flux densities and $D_{\rm L}$ is the luminosity distance. For simplicity, we use an online tool to compute the luminosity distances[6].

[5]Templates and instructions available at: `http://david.elbaz3.free.fr/astro_codes/chary_elbaz.html`

[6]`http://www.astro.ucla.edu/œwright/CosmoCalc.html`

Table 6.5: Best fit dust SED models.

Source name	EP Eridani	EP Eridani
Density distribution, γ	0	0
Grain size distribution, q	3.5	3.5
Average dust temperature (K)*	28.1 ± 18.9	28.0 ± 17.4
Radius range (AU)	5 - 110	10 - 110
Mass ($M_{\rm Moon}$)	$(2.1 \pm 0.1) \times 10^{-2}$	$(2.2 \pm 0.2) \times 10^{-2}$
Luminosity ratio, $f_{\rm d}$	$(3.2 \pm 0.2) \times 10^{-5}$	$(2.9 \pm 0.2) \times 10^{-5}$
Accuracy χ^2	1.8	1.5
Source name	Gliese2	Gliese 42
Density distribution, γ	-1	-1
Grain size distribution, q	2.5	2.0
Average dust temperature (K)*	22.1 ± 20.7	21.9 ± 21.0
Radius range (AU)	0.2 - 70.0	0.2 - 70.0
Mass ($M_{\rm Moon}$)	1.9 ± 0.2	9.3 ± 1.0
Luminosity ratio, $f_{\rm d}$	$(8.7 \pm 0.9) \times 10^{-6}$	$(8.7 \pm 1.0) \times 10^{-6}$
Accuracy χ^2	0.6	0.5

Notes. * The uncertainty is the $3\,\sigma$ error.

Thus, we did not adapt the flux densities to fit the data, we simply set different redshifts and then looped through the templates to find best fits. We did limit the redshifts to less than two, because galaxies at higher redshifts become too faint to be an issue for us.

6.5 Discussion

6.5.1 Field backgrounds

The probability of chance alignment is lower than 3% at these flux levels at 100 μm (see Section 2.3.1). We can compare this with Krivov et al. (2013) who use the same references, but for cold discs, i.e. 6–13 mJy at 160 μm. They found a probability of 4.8 %, which statistically means that we can expect that of the 133 DUNES sources, only 6.4 are aligned with background galaxies.

We also have observations at the wavelengths of 870 μm (LABOCA), and 250μm to 500 μm (SPIRE). To compare probabilities at longer wavelengths than PACS, we may look at figure 4 from Hatsukade et al. (2013) which shows the number count of galaxies at 1.3 mm. From this figure we can estimate that a flux density limit of 4 mJy beam^{-1} gives a number count of $(2 \pm 1) \times 10^{-3}$ beam^{-1} (RMS of LABOCA observations are between 3 and 6 mJy beam^{-1}). That implies a risk of alignment of roughly 0.2 % at 1.3 mm, and subsequently a risk of contamination with SPIRE and LABOCA observations between 0.2 % to 4.8 % .

If we also compare with 2MASS completeness limits, we see that not even the most extreme galaxies, those with the highest star forming rates at redshifts higher than 0.5, will be

detectable at optical or NIR wavelengths. It is thus quite unlikely that we will find many of the sources detected with PACS in shorter wavelength observations (as we saw in Sections 6.3.1 and 6.3.2).

6.5.2 EP Eridani

EP Eri is an extended source where we find two possibly associated sources, one to the east and one to the west. Their positions are indicated in Figure 6.2 and more easily visible in Figure 6.4. We found that the eastern source's coordinates coincide with the X-ray source J025234.1-124619, while the nature of the western source is unknown.

The western source is at the angular distance of 21.″69 from the main source, which corresponds to 224 AU at the star's distance (10.35 ± 0.04 pc). That would be an unusual distance if it were due to circumstellar dust. However, there exist examples of highly extended discs around other sun-like stars. HD 107146 is a G2 V star with a ring with radius of ≤ 200 AU (Williams et al. 2004; Ardila et al. 2004), similar is HD 207129 (a G0 V star) with a ring smaller than 180 AU (Krist et al. 2010; Löhne et al. 2012). HD 202628 (a G2 V star) has a more eccentric ring with a maximum visible radius of ~ 250 AU (Krist et al. 2012), however, it is mostly inside about 220 AU. So discs much larger than 220 AU around sun-like and late type stars do appear to be unusual, but not impossible. However, a disc, or a ring, would probably be visible at at least both sides of the main source. As the weaker eastern source has been identified, we can assume that the western source is not associated with EP Eri.

We see extended emission that is directly associated with the main source in Figure 6.4, where we have subtracted the main source with a PSF. We find that this emission is approximately circular in nature which implies that the star has a face-on disc. The extended emission corresponds to radii of roughly 60 and 80 AU respectively, for each PACS wavelength, at the star's distance. For the disc models, however, we used the upper limit radius from the $1\,\sigma$ limit at 160 μm, i.e. 20.″5, which corresponds to a radius of 110 AU. The disc model's inner radius was (initially) set to the sublimation radius of 0.03 AU.

Initially, we used the parameters $q = 3.5$ and $\gamma = 1$ but were forced to expand these ranges while exploring the parameter space. We also varied the radius of the inner hole of the disc.

We found that even small negative γ, slightly increasing density profiles, resulted in too cold dust. Finding fitting models was a matter of balancing the inner radius and the density profile. Difficulties with fitting both the 70 μm and 160 μm data at the same time tempted us to look at the possibility of a gap in the disc. However, with only three relevant data points we have too little information to be able to constrain such detailed models.

The best fit model indicates that the disc has quite a flat density distribution (close to zero) with a large inner hole of a radius of up to 10 AU, and a standard grain size distribution of $q = 3.5$. Representative SEDs fitted to the 100 μm flux density are plotted in Figure 6.6. The models with too warm dust are also fitted close to the 100 μm flux, and as they peak at much shorter wavelengths they have much lower flux density at 160 μm. The best-fit models are presented in Table 6.5.

The emission of the FIR galactic SED models from Chary & Elbaz (2001) proved difficult to fit to EP Eri's excess (best $\chi^2 \approx 100$ to 200). FIR galactic dust is simply too cold for this emission, which is another direct indication that EP Eri's excess is due to circumstellar dust.

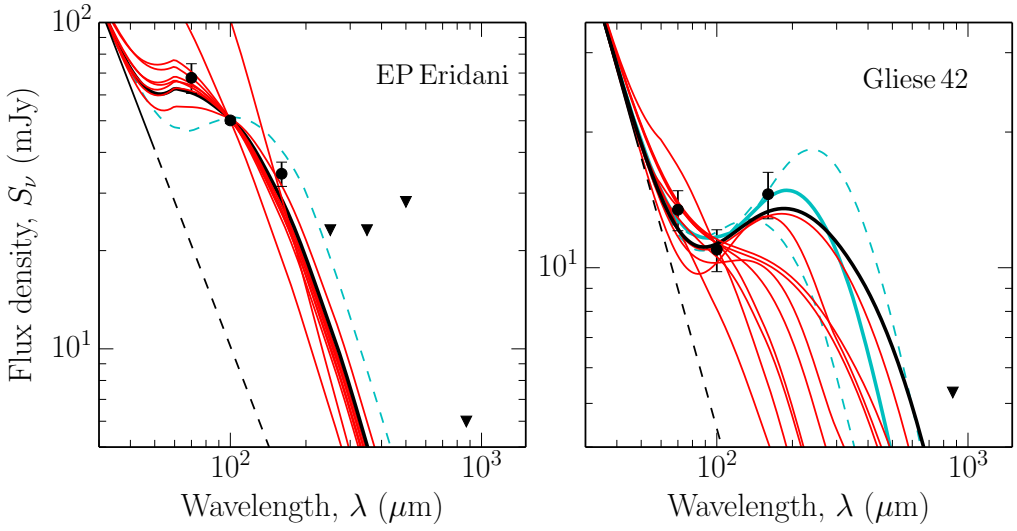

Figure 6.6: Excess models for EP Eri and Gli 42. Black thin lines are the stellar photospheric models, dashed black lines indicate where the photosphere is approximated as a Rayleigh-Jeans tail. Red lines are dust emission plus photosphere emission for discs with varying density distributions and grain size distribution. The best fit dust model is plotted as a thick black line. Cyan lines indicate best FIR galactic SED (Chary & Elbaz 2001), where dashed lines are limits. In the case of EP Eri no galactic model was found to sufficiently fit the data, and only the best model is shown as a cyan dashed line.

6.5.3 Gliese 42

This source was assumed to be a point source by Eiroa et al. (2013). In Figure 6.5 we see the source before and after subtraction of a PSF. Due to the contaminating background sources at 160 μm, we are also forced to assume a point source in order to not overestimate the flux density. The disc size is then based on the maximum beam radius, i.e. the HPBW at 160 μm which corresponds to a radius of approximately 70 AU at this distance.

The disc models are again based on a flaring disc model with a power law radial density distribution, as for EP Eri. The inner radius was set to the sublimation radius, i.e. between 0.01 AU and 0.03 AU, where we used 0.02 AU as an initial inner radius. Other initial parameters were $q = 3.5$ and $\gamma = 1$, and we also fitted each model to the 100 μm flux density.

It proved difficult to find a good fit to the data with a "standard" disc model. The radial constraint and $q = 3.5$ combined always resulted in too hot emission (peaking at too short wavelengths) regardless of density profile or inner radius. These models were possible to fit to the flux density at both 70 μm and 100 μm, however not to the 160 μm flux (see Figure 6.6).

Simpler estimates, however, as a black body, gave the dust temperature of 32 K (Eiroa et al. 2013). This corresponds to a black body radius of 41.2 AU. However, a black body is a poor estimate of a dust ring's real radius. Trends found by Pawellek & Krivov (2015) indicate that the true radius of a disc at Gli 42 can be between 7.3 to $19.5 \times R_{\rm BB}$, i.e. between 300 and 800 AU. This whole radial range is far larger than the radial constraint of 70 AU that was based on the 160 μm beam width.

It is possible, however, to significantly cool the dust by using extinctions with much flat-

ter grain size distributions. This way we find models with both $q = 2.0$ and $q = 2.5$, and with a growing density profile of $\gamma = -1$ that fit the observations (Figure 6.6 and Table 6.5). This corresponds to a ring of dust at up to 70 AU, and less amount of small grains than is usually found through simulations of collisional cascade (see Section 2.2). Such an increasing density profile can occur and is predicted for discs with ongoing planet formation (MacGregor et al. 2013).

When we compare with FIR galaxy SEDs we find a wide range of fitting models at a wide range of redshifts. These are with $z = 1.3 \pm 0.6$, and total IR luminosity of $(2.5^{+5.8}_{-2.1}) \times 10^{12}\,L_{\odot}$. This range of redshifts is quite high but the higher redshifts require quite luminous galaxies, making chance alignment less probable for higher redshifts, but not impossible. The problems involved with models arises from the high 160 μm flux density. It is also at this wavelength that the main source is most contaminated. We conclude that the nature of this source remains unclear and that further observations are required. The high proper motion of this star (620 mas yr^{-1}) will move it away from the contaminating background sources in less than 10 years, however, ALMA is be able to resolve all the sources in the angular proximity of the star today.

6.6 Conclusions

Our conclusions are summarised as follows:

- We found that EP Eri may have a face-on dust disc. Modelling indicates that this disc has a flat radial surface density distribution ($\gamma = 0$), it extends between 5-10 AU to 110 AU, and it has a grain size distribution of $q = 3.5$. This model corresponds to a disc with a dust-to-star luminosity ratio $\sim 3\times10^{-5}$ and total dust mass of $\sim 2\times10^{-2}\,M_{\rm Moon}$.
- Gli 42 exhibits quite cold dust emission, making it difficult to fit a "standard" model to the data with the assumption that this is a point source. We were able to fit dust models using an increasing surface density distribution ($\gamma = -1$), and a flatter grain size distribution of $q = 2.0$ to 2.5. These models have a luminosity ratio of 9×10^{-6} and a total dust mass of 2 or 9 $M_{\rm Moon}$ depending on choice of q. We were also able to fit FIR galaxy SEDs to the excess emission. These correspond to a wide range of redshifts (z from 0.7 to 1.9) and total IR luminosities (0.4 to $8.3 \times 10^{12}\,L_{\odot}$). The nature of this source is unclear. It is heavily contaminated at 160 μm, however, due to its high proper motion observations at an additional epoch, in about 10 years, would be useful. It should have moved 6″ to 7″ at that time, and be sufficiently far from the background sources for observations.

Chapter 7

Summary and future prospects

This thesis provides ample possibilities for further research. For example, in the case of 94 Cet (Chapter 4 and Paper II) we are able to map out the field and set models for the dust emission. However, the possibility of a circumtertiary ring at > 650 AU is compelling and was not (dis)proven. The system does not have a very high proper motion, so future observations might not provide an answer to the question of its existence. It may be possible to observe a similar map of CO$(2-1)$ as was done for α Cen with APEX to compare $v_{\rm LSR}$, the local-standard-of-rest velocity of the sources.

Another interesting case study is that of Gli 42 in Chapter 6. The source exhibits excesses at 70, 100, and 160 μm. However, the source is contaminated by at least three background sources, especially at 160 μm, which makes it difficult to fit dust SED models to the observed SED. We found that models containing dust with an unusually flat dust grain size distribution, and emission from a wide range of high-redshift galaxies, fit the observations of Gli 42.

It is possible that the Gli 42 emission is just a case of chance alignment with a background galaxy. It is also possible that the emission at 70 and 100 μm are due to dust emission, while it is only the 160 μm emission that is contaminated, and thus much higher than that of the star+dust. This can be explored with either high resolution FIR observations or future single-dish observations in ~ 10 years, when the star's proper motion has moved it sufficiently far on the sky so that it does not risk contamination from the background sources.

Furthermore, it would be prudent to use newly reduced data for both EP Eri and Gli 42, instead of the data that were reduced with HIPE 7.2 in the case of a future paper.

Concerning new reductions, in Chapter 5 and Paper III, I presented results on a total re-reduction of the whole expanded DUNES dataset, i.e. the original 133 sources presented by Eiroa et al. (2013) and the additional 55 sources presented by Montesinos et al. (2016). The additional 55 sources were reduced with HIPE 10, and was used as a control group. These results corresponded well with my results from HIPE 13.0.0, while the new reduction of the Eiroa et al. (2013) data set systematically exhibited a $1\sigma_{\rm F}$ higher flux density. There exist several possible new excess sources due to this, because these sources were previously just below the detection limit.

However, not to risk overestimating the number of excess sources, I decided to define two limits, where the dust excess is measured with a $\chi_{\rm dust}$ parameter. Sources with $\chi_{\rm dust} > 5$ are considered as strong detected excesses, while $3 < \chi_{\rm dust} < 5$ are considered as marginally

detected excesses. In my analysis, there is only one new source that had $\chi_{\rm dust} > 5$, i.e. δ Pavonis (HIP 99420, HD 190248). This source exhibits an excess at 100 μm, but none at 70μm nor 160 μm. This is a very steep excess, and a more in-depth study is required the find the real cause of it.

The outlooks are initially somewhat unclear for the future in dust disc research. There exist no suitable FIR space telescopes in operation after the shutdown of *Herschel*. However, other possibilities exist such as the Stratospheric Observatory for Infrared Astronomy (SOFIA). This is a 2.5 m telescope mounted on a Boeing 747, and is a joint project between NASA and the German aerospace center (Becklin 1997).

There also exist ground based telescopes that are available today. The Atacama Large Millimeter/submillimeter Array (ALMA)[1] is probably most famous among these. ALMA does not give the same possibilities as *Herschel* did, because it will not observe wavelengths shorter than $300\,\mu$m, but it has anyway proven useful for circumstellar disc observations. Another possibility is the Large Millimeter Telescope (LMT) in Mexico. Located at an altitude of 4640 m on Sierra Negra, it is the largest single-dish telescope at its wavelength range (850 μm and 4 mm), with its 50 m diameter dish.

A space based telescope is required to reach the same high frequencies as *Herschel* did. The Space Infrared Telescope for Cosmology and Astrophysics (SPICA) is a planned mission that is similar to *Herschel* with a 2.5-m mirror. This will primarily be a spectroscopic mission between the wavelengths of 12 μm to 210 μm, however, the launch date is not yet decided, and it might not be launched before 2030.

A really promising future lies in exoplanetary research. Dust discs and planets are intricately coupled, as we discussed in Chapter 1. One goal in both dust disc and exoplanetary research is to map out the contents of the nearest exoplanetary systems. The goal is partly to understand the dynamics and evolution of these systems, and also to put our Solar system into a wide context.

There are already several planet searching missions being planned, for example, the Transiting Exoplanet Survey Satellite[2] (TESS, planned for launch in 2017), the CHaracterising ExOPlanets Satellite[3] (CHEOPS, planned for launch by 2017-2018), and Planetary Transits and Oscillations of stars[4] (PLATO, planned for launch in 2024). Combining data from these with ground based telescopes (the Very Large Telescope and the coming European Extremely Large Telescope) will make it possible to map both the size and mass of exoplanets in the Solar neighbourhood.

[1] `http://www.almaobservatory.org/`
[2] `https://tess.gsfc.nasa.gov/`
[3] `http://cheops.unibe.ch/`
[4] `http://sci.esa.int/plato/`

Bibliography

Acke, B., Min, M., Dominik, C., et al. 2012, A&A, 540, A125

Anglada-Escudé, G., Amado, P. J., Barnes, J., et al. 2016, Nature, 536, 437

Ardila, D. R., Golimowski, D. A., Krist, J. E., et al. 2004, ApJL, 617, L147

Artymowicz, P. 1997, Annual Review of Earth and Planetary Sciences, 25, 175

Aumann, H. H. 1985, PASP, 97, 885

Aumann, H. H., Beichman, C. A., Gillett, F. C., et al. 1984, ApJL, 278, L23

Aumatell, G. & Wurm, G. 2011, MNRAS, 418, L1

Avrett, E. H. 2003, in Astronomical Society of the Pacific Conference Series, Vol. 286, Current Theoretical Models and Future High Resolution Solar Observations: Preparing for ATST, ed. A. A. Pevtsov & H. Uitenbroek, 419

Ayres, T. R., Linsky, J. L., Rodgers, A. W., & Kurucz, R. L. 1976, ApJ, 210, 199

Balog, Z., Müller, T., Nielbock, M., et al. 2014, Experimental Astronomy, 37, 129

Becklin, E. E. 1997, in ESA Special Publication, Vol. 401, The Far Infrared and Submillimetre Universe., ed. A. Wilson, 201–206

Bernstein, G. M., Trilling, D. E., Allen, R. L., et al. 2004, AJ, 128, 1364

Berta, S., Magnelli, B., Nordon, R., et al. 2011, A&A, 532, A49

Bessell, M. S. 1990, PASP, 102, 1181

Beust, H. 2003, A&A, 400, 1129

Boesgaard, A. M., Lum, M. G., & Deliyannis, C. P. 2015, ApJ, 799, 202

Brott, I. & Hauschildt, P. H. 2005, in ESA Special Publication, Vol. 576, The Three-Dimensional Universe with Gaia, ed. C. Turon, K. S. O'Flaherty, & M. A. C. Perryman, 565

Campbell, B., Walker, G. A. H., & Yang, S. 1988, ApJ, 331, 902

Chary, R. & Elbaz, D. 2001, ApJ, 556, 562

Colless, M., Peterson, B. A., Jackson, C., et al. 2003, ArXiv Astrophysics e-prints

Currie, T., Debes, J., Rodigas, T. J., et al. 2012, ApJL, 760, L32

Cutispoto, G., Messina, S., & Rodonò, M. 2001, A&A, 367, 910

Dame, T. M., Hartmann, D., & Thaddeus, P. 2001, ApJ, 547, 792

de Graauw, T., Helmich, F. P., Phillips, T. G., et al. 2010, A&A, 518, L6

Decin, L., Vandenbussche, B., Waelkens, K., et al. 2003, A&A, 400, 695

Demory, B.-O., Ehrenreich, D., Queloz, D., et al. 2015, MNRAS, 450, 2043

Dent, W. R. F., Wyatt, M. C., Roberge, A., et al. 2014, Science, 343, 1490

Dohnanyi, J. S. 1969, , 74, 2531

Draine, B. T. 1988, ApJ, 333, 848

Draine, B. T. 2003, ApJ, 598, 1017

Draine, B. T. 2006, ApJ, 636, 1114

Dullemond, C. P. 2012, RADMC-3D: A multi-purpose radiative transfer tool, astrophysics Source Code Library

Dumusque, X., Pepe, F., Lovis, C., et al. 2012, Nature, 491, 207

Eiroa, C., Marshall, J. P., Mora, A., et al. 2013, A&A, 555, A11

Elbaz, D., Dickinson, M., Hwang, H. S., et al. 2011, A&A, 533, A119

Elbaz, D., Dickinson, M., Hwang, H. S., et al. 2013, VizieR Online Data Catalog, 353, 39119

Endl, M., Kürster, M., Els, S., Hatzes, A. P., & Cochran, W. D. 2001, A&A, 374, 675

Engels, D., Sherwood, W. A., Wamsteker, W., & Schultz, G. V. 1981, , 45, 5

Ertel, S., Wolf, S., & Rodmann, J. 2012, A&A, 544, A61

Fixsen, D. J. & Dwek, E. 2002, ApJ, 578, 1009

Fracassini, M., Pasinetti-Fracassini, L. E., Pastori, L., & Pironi, R. 1988, Bulletin d'Information du Centre de Donnees Stellaires, 35, 121

Gáspár, A., Psaltis, D., Rieke, G. H., & Özel, F. 2012, ApJ, 754, 74

Gillett, F. C. 1986, in Astrophysics and Space Science Library, Vol. 124, Light on Dark Matter, ed. F. P. Israel, 61–69

Greaves, J. S., Holland, W. S., Matthews, B. C., et al. 2016, MNRAS, 461, 3910

Griffin, M. J., Abergel, A., Abreu, A., et al. 2010, A&A, 518, L3

Grigorieva, A., Thébault, P., Artymowicz, P., & Brandeker, A. 2007, A&A, 475, 755

Gu, Y., Jefferies, J. T., Lindsey, C., & Avrett, E. H. 1997, ApJ, 484, 960

Gustafson, B. A. S. 1994, Annual Review of Earth and Planetary Sciences, 22, 553

Hale, A. 1994, AJ, 107, 306

Hatsukade, B., Ohta, K., Seko, A., Yabe, K., & Akiyama, M. 2013, ApJL, 769, L27

Hatzes, A. P. 2013, ApJ, 770, 133

Hatzes, A. P., Cochran, W. D., Endl, M., et al. 2003, ApJ, 599, 1383

Hatzes, A. P., Cochran, W. D., McArthur, B., et al. 2000, ApJL, 544, L145

Hauck, B. & Mermilliod, M. 1997, VizieR Online Data Catalog, 2215, 0

Helou, G., Madore, B. F., Schmitz, M., et al. 1991, in Astrophysics and Space Science Library, Vol. 171, Databases and On-line Data in Astronomy, ed. M. A. Albrecht & D. Egret, 89–106

Hildebrand, R. H. 1983, , 24, 267

Holman, M. J. & Wiegert, P. A. 1999, AJ, 117, 621

Houck, J. R., Roellig, T. L., van Cleve, J., et al. 2004, ApJS, 154, 18

Inoue, A. K., Honda, M., Nakamoto, T., & Oka, A. 2008, , 60, 557

Jaime, L. G., Pichardo, B., & Aguilar, L. 2012, MNRAS, 427, 2723

Kalas, P., Graham, J. R., Chiang, E., et al. 2008, Science, 322, 1345

Kalas, P., Graham, J. R., Fitzgerald, M. P., & Clampin, M. 2013, ApJ, 775, 56

Kataoka, A., Okuzumi, S., Tanaka, H., & Nomura, H. 2014, A&A, 568, A42

Kennedy, G. M., Wyatt, M. C., Kalas, P., et al. 2014, MNRAS, 438, L96

Kennedy, G. M., Wyatt, M. C., Sibthorpe, B., et al. 2012, MNRAS, 421, 2264

Kervella, P., Thévenin, F., Ségransan, D., et al. 2003, A&A, 404, 1087

Kral, Q., Thébault, P., & Charnoz, S. 2013, A&A, 558, A121

Krist, J. E., Stapelfeldt, K. R., Bryden, G., & Plavchan, P. 2012, AJ, 144, 45

Krist, J. E., Stapelfeldt, K. R., Bryden, G., et al. 2010, AJ, 140, 1051

Krivov, A. V. 2010, Research in Astronomy and Astrophysics, 10, 383

Krivov, A. V., Eiroa, C., Löhne, T., et al. 2013, ApJ, 772, 32

Krivov, A. V., Löhne, T., & Sremčević, M. 2006, A&A, 455, 509

Krügel, E. & Siebenmorgen, R. 1994, A&A, 288, 929

Lagrange, A.-M., Gratadour, D., Chauvin, G., et al. 2009, A&A, 493, L21

Lamy, P. L. 1974, A&A, 35, 197

Liseau, R., De la Luz, V., O'Gorman, E., et al. 2016, ArXiv e-prints

Liseau, R., Montesinos, B., Olofsson, G., et al. 2013, A&A, 549, L7

Liseau, R., Risacher, C., Brandeker, A., et al. 2008, A&A, 480, L47

Liseau, R., Vlemmings, W., Bayo, A., et al. 2015, A&A, 573, L4

Löhne, T., Augereau, J.-C., Ertel, S., et al. 2012, A&A, 537, A110

Löhne, T., Krivov, A. V., & Rodmann, J. 2008, ApJ, 673, 1123

Loukitcheva, M., Solanki, S. K., Carlsson, M., & Stein, R. F. 2004, A&A, 419, 747

MacGregor, M. A., Wilner, D. J., Rosenfeld, K. A., et al. 2013, ApJL, 762, L21

Maldonado, J., Eiroa, C., Villaver, E., Montesinos, B., & Mora, A. 2012, A&A, 541, A40

Mamajek, E. E., Bartlett, J. L., Seifahrt, A., et al. 2013, AJ, 146, 154

Mamajek, E. E. & Hillenbrand, L. A. 2008, ApJ, 687, 1264

Marengo, M., Stapelfeldt, K., Werner, M. W., et al. 2009, ApJ, 700, 1647

Mathis, J. S., Rumpl, W., & Nordsieck, K. H. 1977, ApJ, 217, 425

Matthews, B. C., Sibthorpe, B., Kennedy, G., et al. 2010, A&A, 518, L135

Mayor, M. & Queloz, D. 1995, Nature, 378, 355

Mayor, M., Udry, S., Naef, D., et al. 2004, A&A, 415, 391

Metchev, S. A., Hillenbrand, L. A., & Meyer, M. R. 2004, ApJ, 600, 435

Miyake, K. & Nakagawa, Y. 1993, , 106, 20

Montesinos, B., Eiroa, C., Krivov, A. V., et al. 2016, ArXiv e-prints

Moro-Martín, A. 2013, Dusty Planetary Systems, ed. T. D. Oswalt, L. M. French, & P. Kalas, 431

Moro-Martín, A., Marshall, J. P., Kennedy, G., et al. 2015, ApJ, 801, 143

Moutou, C., Díaz, R. F., Udry, S., et al. 2011, A&A, 533, A113

Ossenkopf, V. & Henning, T. 1994, A&A, 291, 943

Ott, S. 2010, in Astronomical Society of the Pacific Conference Series, Vol. 434, Astronomical Data Analysis Software and Systems XIX, ed. Y. Mizumoto, K.-I. Morita, & M. Ohishi, 139

Paardekooper, S.-J. & Leinhardt, Z. M. 2010, MNRAS, 403, L64

Pawellek, N. & Krivov, A. V. 2015, MNRAS, 454, 3207

Pawellek, N., Krivov, A. V., Marshall, J. P., et al. 2014, ApJ, 792, 65

Pilbratt, G. L., Riedinger, J. R., Passvogel, T., et al. 2010, A&A, 518, L1

Plavchan, P., Werner, M. W., Chen, C. H., et al. 2009, ApJ, 698, 1068

Poglitsch, A., Waelkens, C., Geis, N., et al. 2010, A&A, 518, L2

Pollack, J. B., Hollenbach, D., Beckwith, S., et al. 1994, ApJ, 421, 615

Pourbaix, D. & Boffin, H. M. J. 2016, A&A, 586, A90

Pourbaix, D., Nidever, D., McCarthy, C., et al. 2002, A&A, 386, 280

Queloz, D., Mayor, M., Naef, D., et al. 2004, in IAU Symposium, Vol. 202, Planetary Systems in the Universe, ed. A. Penny, 106

Raghavan, D., Henry, T. J., Mason, B. D., et al. 2006, ApJ, 646, 523

Rajpaul, V., Aigrain, S., & Roberts, S. 2016, MNRAS, 456, L6

Regály, Z., Juhász, A., Sándor, Z., & Dullemond, C. P. 2012, MNRAS, 419, 1701

Rigby, E. E., Maddox, S. J., Dunne, L., et al. 2011, MNRAS, 415, 2336

Roberts, Jr., L. C., Turner, N. H., ten Brummelaar, T. A., Mason, B. D., & Hartkopf, W. I. 2011, AJ, 142, 175

Röll, T., Neuhäuser, R., Seifahrt, A., & Mugrauer, M. 2012, A&A, 542, A92

Röll, T., Seifahrt, A., Neuhäuser, R., Köhler, R., & Bean, J. 2011, in EAS Publications Series, Vol. 45, EAS Publications Series, 429–432

Sánchez-Portal, M., Marston, A., Altieri, B., et al. 2014, Experimental Astronomy, 37, 453

Shannon, A., Clarke, C., & Wyatt, M. 2014, MNRAS, 442, 142

Siringo, G., Kreysa, E., Kovács, A., et al. 2009, A&A, 497, 945

Skrutskie, M. F., Cutri, R. M., Stiening, R., et al. 2006, AJ, 131, 1163

Smith, B. A. & Terrile, R. J. 1984, Science, 226, 1421

Smyth, W. H. 1844, A cycle of celestial objects

Söderhjelm, S. 1999, A&A, 341, 121

Stark, C. C. & Kuchner, M. J. 2008, ApJ, 686, 637

Strubbe, L. E. & Chiang, E. I. 2006, ApJ, 648, 652

Su, K. Y. L. & Rieke, G. H. 2014, in IAU Symposium, Vol. 299, Exploring the Formation and Evolution of Planetary Systems, ed. M. Booth, B. C. Matthews, & J. R. Graham, 318–321

Thébault, P. 2012, A&A, 537, A65

Thébault, P. 2016, A&A, 587, A88

Thébault, P. & Augereau, J.-C. 2007, A&A, 472, 169

Thébault, P., Marzari, F., & Augereau, J.-C. 2010, A&A, 524, A13

Thébault, P., Marzari, F., & Scholl, H. 2009, MNRAS, 393, L21

Thévenin, F., Provost, J., Morel, P., et al. 2002, A&A, 392, L9

Torres, G., Andersen, J., & Giménez, A. 2010, , 18, 67

Trilling, D. E., Bryden, G., Beichman, C. A., et al. 2008, ApJ, 674, 1086

Vernazza, J. E., Avrett, E. H., & Loeser, R. 1981, ApJS, 45, 635

Vitense, C., Krivov, A. V., Kobayashi, H., & Löhne, T. 2012, A&A, 540, A30

Vitense, C., Krivov, A. V., & Löhne, T. 2010, A&A, 520, A32

Wahhaj, Z., Koerner, D. W., Ressler, M. E., et al. 2003, ApJL, 584, L27

Walker, G. A. H., Bohlender, D. A., Walker, A. R., et al. 1992, ApJL, 396, L91

Weingartner, J. C. & Draine, B. T. 2001, ApJ, 548, 296

Wiegert, P. A. & Holman, M. J. 1997, AJ, 113, 1445

Williams, J. P., Najita, J., Liu, M. C., et al. 2004, ApJ, 604, 414

Wolszczan, A. & Frail, D. A. 1992, Nature, 355, 145

Wood, B. E., Linsky, J. L., Müller, H.-R., & Zank, G. P. 2001, ApJL, 547, L49

Wood, B. E., Müller, H.-R., Zank, G. P., Linsky, J. L., & Redfield, S. 2005, ApJL, 628, L143

Wyatt, M. C. 2008, ARAA, 46, 339

Wyatt, M. C., Clarke, C. J., & Booth, M. 2011, Celestial Mechanics and Dynamical Astronomy, 111, 1

Xie, J.-W., Zhou, J.-L., & Ge, J. 2010, ApJ, 708, 1566

Zubko, V., Dwek, E., & Arendt, R. G. 2004, ApJS, 152, 211

Zuckerman, B. 2001, ARAA, 39, 549

Zuckerman, B., Song, I., Bessell, M. S., & Webb, R. A. 2001, ApJL, 562, L87